

1994

Inverse estimation of horizontal pressure gradients and vertical eddy viscosity profiles in shallow waters

Bohyun Bang

College of William and Mary - Virginia Institute of Marine Science

Follow this and additional works at: <https://scholarworks.wm.edu/etd>



Part of the [Oceanography Commons](#)

Recommended Citation

Bang, Bohyun, "Inverse estimation of horizontal pressure gradients and vertical eddy viscosity profiles in shallow waters" (1994). *Dissertations, Theses, and Masters Projects*. Paper 1539616559.

<https://dx.doi.org/doi:10.25773/v5-ayht-wm75>

This Dissertation is brought to you for free and open access by the Theses, Dissertations, & Master Projects at W&M ScholarWorks. It has been accepted for inclusion in Dissertations, Theses, and Masters Projects by an authorized administrator of W&M ScholarWorks. For more information, please contact scholarworks@wm.edu.

INFORMATION TO USERS

This manuscript has been reproduced from the microfilm master. UMI films the text directly from the original or copy submitted. Thus, some thesis and dissertation copies are in typewriter face, while others may be from any type of computer printer.

The quality of this reproduction is dependent upon the quality of the copy submitted. Broken or indistinct print, colored or poor quality illustrations and photographs, print bleedthrough, substandard margins, and improper alignment can adversely affect reproduction.

In the unlikely event that the author did not send UMI a complete manuscript and there are missing pages, these will be noted. Also, if unauthorized copyright material had to be removed, a note will indicate the deletion.

Oversize materials (e.g., maps, drawings, charts) are reproduced by sectioning the original, beginning at the upper left-hand corner and continuing from left to right in equal sections with small overlaps. Each original is also photographed in one exposure and is included in reduced form at the back of the book.

Photographs included in the original manuscript have been reproduced xerographically in this copy. Higher quality 6" x 9" black and white photographic prints are available for any photographs or illustrations appearing in this copy for an additional charge. Contact UMI directly to order.

U·M·I

University Microfilms International
A Bell & Howell Information Company
300 North Zeeb Road, Ann Arbor, MI 48106-1346 USA
313/761-4700 800/521-0600



Order Number 9501969

**Inverse estimation of horizontal pressure gradients and vertical
eddy viscosity profiles in shallow waters**

Bang, Bohyun, Ph.D.

The College of William and Mary, 1994

U·M·I
300 N. Zeeb Rd.
Ann Arbor, MI 48106



**Inverse Estimation of Horizontal Pressure Gradients and Vertical Eddy
Viscosity Profiles in Shallow Waters**

A Dissertation presented to
The Faculty of the School of Marine Science
The College of William and Mary in Virginia

In Partial Fulfilment of the Requirements for the Degree of
Doctor of Philosophy

by
Bohyun Bang

1994

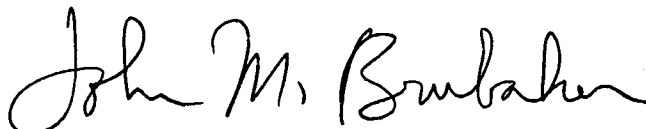
APPROVAL SHEET

This dissertation is submitted in partial fulfillment of
the requirements for the degree of

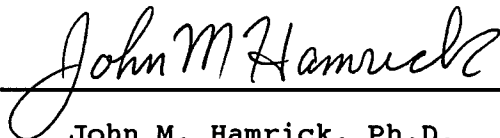
Doctor of Philosophy

Bohyun Bang

Approved, June 1994




John M. Brubaker, Ph.D.
Committee Chairman/Advisor



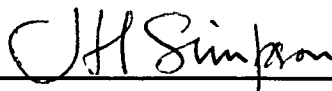
John M. Hamrick, Ph.D.



Mark R. Patterson, Ph.D.



Evon P. Ruzecki, Ph.D.



John H. Simpson, Professor
School of Ocean Sciences
University of Wales, UK.

TABLE OF CONTENTS

	Page
ACKNOWLEDGEMENTS	v
LIST OF TABLES	vi
LIST OF FIGURES	ix
LIST OF SYMBOLS	xiii
ABSTRACT	xiv
I. INTRODUCTION	1
II. SHEAR STRESS AND TURBULENCE	6
A. Direct Measurement	6
B. Indirect Estimation	7
C. Turbulence Model	9
III. REVIEW OF INVERSE METHODS	12
IV. METHODS	15
A. Dynamic Equation	15
B. Inverse Scheme	28
C. Data Processing	30
D. Numerical Model	32
E. Computer Codes	34
V. DATA AND ANALYSES	35
A. Model-Simulated Data	35
B. Literature Data	38
C. Field Data	39
VI. RESULTS	49
A. Tests on Model-Simulated Data	50
B. Results with Literature Data	60
C. Results with Current Mooring Data	62

D. Results with ADCP Data	116
VII. DISCUSSION	130
A. Pressure Gradient Acceleration	130
B. Eddy Viscosity	133
C. Shear Stress and Depth-Average <i>TKE</i> Production	140
D. Role of $u_0(z)$ in Inverse Systems	142
VIII. CONCLUSIONS	144
LITERATURE CITED	150
VITA	155

ACKNOWLEDGEMENTS

I would like to thank Dr. John M. Brubaker for his advice, patience and support throughout the study. Thanks are also extended to Dr. John H. Simpson who provided me significant suggestions and advice. Dr. John M. Hamrick relieved me with many tips in numerical computation. I wish to thank other committee members, Dr. Evon P. Ruzicki and Dr. Mark R. Patterson, for their constructive reviews on the manuscript. Thanks are extended to Dr. Albert Kuo for comments, and to Mr. M. Sisson for his unending help in organizing mooring data. It was Dr. W. Bouicourt, at the Horn Point Environmental Laboratory, U. Maryland, who generously provided the bottom-mounted ADCP data.

I owe a great deal of debt to my wife, Hwaseon, and two sons, Hyeongwoo and Joohn, for their encouragement, cheer and endurance.

LIST OF TABLES

Table		Page
IV-1	Necessary conditions for inverse systems to be overdetermined	28
V-1	Numerical-model input: pressure gradient accelerations	37
V-2	Numerical-model output specification	37
V-3	Location of mooring stations	43
V-4	Deployment information in the upper York	43
V-5	Deployment information at the York mouth	44
V-6	Deployment information in the bay mainstem	45
V-7	Split deployment information with moorings	46
V-8	ADCP system configuration	48
V-9	ADCP deployment information	48
VI-1	Inversion experiments on data from the model-run A: pressure gradient acceleration PGA_T	52
VI-2	Inversion experiments on data from the model-run A: eddy viscosity N_{z0}	52
VI-3	Inversion experiments on data from the model-run A (I01): eddy viscosity $N_{z_{M4}}$	53
VI-4	Inversion experiments on data from the model-run B: pressure gradient acceleration PGA_T	55
VI-5	Inversion experiments on data from the model-run B: eddy viscosity N_{z0}	55
VI-6	Inversion experiments on data from the model-run B (I01): eddy viscosity $N_{z_{M4}}$	56
VI-7	General measures of numerical confidence in analyses of model-generated datasets	57

VI-8	Inversion of data from Bowden and Fairbairn(1952): pressure gradient acceleration PGA_T	61
VI-9	Inversion of data from Wolf(1980): pressure gradient acceleration PGA_T	61
VI-10	General measures of numerical confidence in analyses of literature datasets	61
VI-11	Inversions at the station 'Clay': pressure gradient acceleration PGA_T	64
VI-12	Inversions at the station 'Clay': eddy viscosity N_{z0}	64
VI-13	Inversions at the station 'Allm': pressure gradient acceleration PGA_T	65
VI-14	Inversions at the station 'Allm': pressure gradient acceleration N_{z0}	65
VI-15	General measures of numerical confidence at the upper York stations	68
VI-16	Scaling factors and drag coefficients at the upper York stations	68
VI-17	Time-residual pressure gradient acceleration, PGA_0 , at the upper York stations	68
VI-18	Scaling factors and drag coefficients at the lower York stations	77
VI-19	Scaled maximum of eddy viscosity and its vertical location at the lower York stations	77
VI-20	Estimated time-residual pressure gradient acceleration, PGA_0 , at the lower York stations	77
VI-21	General measures of numerical confidence at the lower York stations	77
VI-22	Scaling factors and drag coefficients at the bay stations	96
VI-23	Relative deviation ($ \Delta %$) in scaling factors and drag coefficients from seasonal means at the upper bay station, 'NOS121'	96

VI-24	Scaled maximum of eddy viscosity and its vertical location at the bay stations	96
VI-25	Estimates of time-residual pressure gradient acceleration, PGA_0 , at the bay stations	97
VI-26	General measures of numerical confidence at the bay stations	97
VI-27	Inversions on ADCP data without $N_{z_{M4}}$ resolution: PGA_T estimates	119
VI-28	Comparison of PGA_T estimates from ADCP data without and with $N_{z_{M4}}$ resolution	119

LIST OF FIGURES

Fig.		Page
V-1	Overview of current stations in Chesapeake Bay and one of its tributaries	42
VI-A-1a	Model-run A: Current structure (M_2) and PGA_T estimates	58
VI-A-2a	Model-run B: Current structure (5 constituents) and PGA_T estimates	59
VI-C-1a	Currents and estimates of PGA_T at the station 'Clay'	69
VI-C-1b	Eddy viscosity and shear stress at the station 'Clay'	70
VI-C-1c	Hysteresis and depth-average TKE production at the station 'Clay'	71
VI-C-2a	Currents and estimates of PGA_T at the station 'Allm'	72
VI-C-2b	Eddy viscosity and shear stress at the station 'Allm'	73
VI-C-2c	Hysteresis and depth-average TKE production at the station 'Allm'	74
VI-C-3a	Currents and estimates of PGA_T at the station 'Y0.0'	78
VI-C-3b	Eddy viscosity and shear stress at the station 'Y0.0'	79
VI-C-3c	Hysteresis and depth-average TKE production at the station 'Y0.0'	80
VI-C-4a	Currents and estimates of PGA_T at the station 'RB'	81
VI-C-4b	Eddy viscosity and shear stress at the station 'RB'	82
VI-C-4c	Hysteresis and depth-average TKE production at the station 'RB'	83

VI-C-5a	Currents and estimates of PGA_T at the station 'Tu91': segment 'a'	84
VI-C-5b	Eddy viscosity and shear stress at the station 'Tu91': segment 'a'	85
VI-C-5c	Hysteresis and depth-average TKE production at the station 'Tu91': segment 'a'	86
VI-C-6a	Currents and estimates of PGA_T at the station 'Tu91': segment 'b'	87
VI-C-6b	Eddy viscosity and shear stress at the station 'Tu91': segment 'b'	88
VI-C-6c	Hysteresis and depth-average TKE production at the station 'Tu91': segment 'b'	89
VI-C-7a	Currents and estimates of PGA_T at the station 'Tu91': segment 'c'	90
VI-C-7b	Eddy viscosity and shear stress at the station 'Tu91': segment 'c'	91
VI-C-7c	Hysteresis and depth-average TKE production at the station 'Tu91': segment 'c'	92
VI-C-8a	Currents and estimates of PGA_T at the station 'NOS066': segment 'a'	98
VI-C-8b	Eddy viscosity and shear stress at the station 'NOS066': segment 'a'	99
VI-C-8c	Hysteresis and depth-average TKE production at the station 'NOS066': segment 'a'	100
VI-C-9a	Currents and estimates of PGA_T at the station 'NOS066': segment 'b'	101
VI-C-9b	Eddy viscosity and shear stress at the station 'NOS066': segment 'b'	102
VI-C-9c	Hysteresis and depth-average TKE production at the station 'NOS066': segment 'b'	103
VI-C-10a	Currents and estimates of PGA_T at the station 'NOS121': segment 'a'	104
VI-C-10b	Eddy viscosity and shear stress at the station 'NOS121': segment 'a'	105

VI-C-10c	Hysteresis and depth-average TKE production at the station 'NOS121': segment 'a'	106
VI-C-11a	Currents and estimates of PGA_T at the station 'NOS121': segment 'b'	107
VI-C-11b	Eddy viscosity and shear stress at the station 'NOS121': segment 'b'	108
VI-C-11c	Hysteresis and depth-average TKE production at the station 'NOS121': segment 'b'	109
VI-C-12a	Currents and estimates of PGA_T at the station 'NOS121': segment 'c'	110
VI-C-12b	Eddy viscosity and shear stress at the station 'NOS121': segment 'c'	111
VI-C-12c	Hysteresis and depth-average TKE production at the station 'NOS121': segment 'c'	112
VI-C-13a	Currents and estimates of PGA_T at the station 'NOS121': segment 'd'	113
VI-C-13b	Eddy viscosity and shear stress at the station 'NOS121': segment 'd'	114
VI-C-13c	Hysteresis and depth-average TKE production at the station 'NOS121': segment 'd'	115
VI-D-1a	Currents and estimates of PGA_T at the ADCP station: without smoothing	120
VI-D-2a	Currents and estimates of PGA_T at the ADCP station: 4-point moving average	121
VI-D-3a	Currents and estimates of PGA_T at the ADCP station: 8-point moving average	122
VI-D-4a	Currents and estimates of PGA_T at the ADCP station: 12-point moving average	123
VI-D-1b	Eddy viscosity and shear stress at the ADCP station: without smoothing	124
VI-D-2b	Eddy viscosity and shear stress at the ADCP station: 4-point moving average	125
VI-D-3b	Eddy viscosity and shear stress at the ADCP station: 8-point moving average	126

VI-D-4b	Eddy viscosity and shear stress at the ADCP station: 12-point moving average	127
VI-D-4c	Hysteresis and depth-average <i>TKE</i> production at the ADCP station: 12-point moving average	128
VI-D-5b	Eddy viscosity and shear stress at the ADCP station: 12-point moving average with N_{2M4} resolution added	129
VII-1	Pressure gradient M_2 in the York River	131
VII-2	Pressure gradient S_2 in the York River	132
VII-3	Pressure gradient N_2 in the York River	132
VII-4	Eddy-viscosity profile reconstructed from Gordon and Dohne(1973)	139
VII-5	Vertical-structure function of eddy viscosity	139

LIST OF MAJOR SYMBOLS

$u;v$	flow velocity in the x, y directions respectively [cm · s ⁻¹]
f	Coriolis parameter [s ⁻¹]
p	pressure [cm ² · s ⁻²]
PGA	pressure gradient acceleration [cm · s ⁻²]
τ	shear stress [cm ² · s ⁻²]
δ	horizontal aspect ratio of wave in a channel
K_E	Kelvin number
g	gravity constant [cm · s ⁻²]
ζ	surface elevation [cm]
ρ	density of fluid [kg · m ⁻³]
λ	$\lambda = (\rho)^{-1} \cdot d\rho/dx$ [cm ⁻¹]
H	total depth of water column [cm]
σ	radian frequency [s ⁻¹]
Φ	phase angle
N_z	eddy viscosity [cm ² · s ⁻¹]
C_d	drag coefficient
P_s	TKE shear production [cm ² · s ⁻³]
θ_{PA}	principal-axis angle from the east
ν	singularity parameter of inversion
γ	misfit parameter of inversion
κ	von Kármán constant (=0.41)
α	sound absorption coefficient
Δ	deviation from a reference
η	scaled depth (upward positive)

ABSTRACT

A least-squares inverse method was devised to estimate horizontal pressure gradients and vertical eddy-viscosity profiles simultaneously, from current profiles. The method was designed mostly for observations of deterministic or near-deterministic wave currents. Tidal-current observations were chosen for the present study.

The inverse system was constructed from a linearized momentum equation. The viscosity was modeled with a time-constant and harmonic function in time, but without its vertical structure predefined. The least-squares problem was solved with the singular value decomposition, by taking current harmonic profiles as input. At first, the method was tested with current profiles simulated by a numerical model employing the mixing-length theory for vertical eddy viscosity. Analyses were done on fourteen sets of real measurements at 6 stations in Chesapeake Bay and one of its tributaries. Thirteen were from current-meter moorings, and one was from a bottom-mounted acoustic Doppler current profiler.

It turned out that the proposed method performed well enough to diagnose a linearized dynamic balance which involved a friction term with time-constant, but depth-dependent eddy viscosity. Eddy-viscosity profiles appeared to have linear-exponential structure. The apparent maximum varied significantly in season, implying some stratification effect. Using the primary results, values of drag coefficient (C_d) and depth-average *TKE* production were deduced. Results of C_d indicated some seasonal variation of bottom roughness. Depth-average *TKE* production in the lower bay appeared to be ~8 times higher than in the mid- or upper bay. The production in the upper part of the York River appeared to be 3-4 times higher than the lower part. Among them, the upper part of the York River appeared to have the highest production.

The approach will be a good tool for the analysis of ADCP measurements in field, due to the simplicity, yet the diagnostic power. The application, however, is limited mostly to deterministic current measurements. The approach is not appropriate to strongly advective flows. Even for weakly advective flows, it is incapable of determining the oscillatory part of the viscosity successfully, due to truncated nonlinear-advective terms.

**Inverse Estimation of Horizontal Pressure Gradients and
Vertical Eddy Viscosity Profiles in Shallow Waters**

I. INTRODUCTION

In shallow waters, vertical exchange is primarily caused by turbulent mixing. Turbulence acts as an intermediary in the transfer of momentum and scalar substances such as buoyancy (heat, salinity), dissolved oxygen, nutrients, small organisms and non-living suspended particles. First of all, to understand the vertical exchange processes, it is necessary to parameterize turbulence. Due to the lack of a universal theory, however, the parameterization requires many collective pieces of information, especially on the buoyancy-feedback mechanism.

The source of turbulent mixing is turbulent kinetic energy (*TKE*) driven by shear stress (Reynolds stress) on the mean flow. This *TKE* shear production may occur from either wind stress at the surface, frictional stress at the bottom, or internal stress in the water column. Mixing is suppressed by water column stratification. The source of stratification is buoyancy driven by solar heating and fresh water input. On a shorter time scale than that of buoyancy flux variation, the degree of stratification depends on the strength of the mean flow shear. In the absence of large episodic events, therefore, water-column stability tends to

remain in quasi-equilibrium state: either well mixed, stably stratified, or partially mixed. In partially mixed waters, both the bottom-generated and the internal shear are considered important (Dyer, 1988).

As the principal source of *TKE* production, shear stress is often determined directly from turbulence measurements or models, or deduced indirectly from the mean flow measurement. Only a few studies utilizing direct measurement can be found in shallow waters, perhaps because turbulent fluctuation is too random and small scaled to be easily detected (cf. Chapter II of this volume). Several closure models have been developed and tested well for the turbulence with vertical buoyancy flux (e.g. Mellor & Yamada, 1982). For the turbulence with lateral buoyancy flux in shallow waters, however, few applications of such models are reported as being generally successful.

The concept of eddy viscosity has been widely accepted and used for the parameterization of shear stress. With the eddy viscosity concept, a simple inverse approach is designed for the simultaneous estimation of dynamic terms (i.e., pressure-gradient force, vertical eddy viscosity and internal shear stress) from vertical array of current measurements. With the estimated pressure-gradient force being substituted, bottom shear stress can be determined from a depth-average momentum balance. Again the depth-

average balance and the pressure-gradient force can be used to determine a drag coefficient and total water-column *TKE* shear-production generated by oscillating currents.

Tidal flow is deterministic so that it may best suit the proposed approach. In Chesapeake Bay, tidal current contributes a considerable amount of mixing energy to oppose a buoyancy flux in a deterministic manner (Pritchard, 1989), though local winds may play an important role in vertical mixing in the middle part of the bay from early fall to spring (Goodrich et al., 1987).

It is well known that incoming principal tides propagate mostly as Kelvin waves from the mouth of the bay (Fisher, 1986; Parker, 1988). Along they propagate, tidal waves may gradually dissipate. Therefore, in the lower bay, tidal waves are probably more energetic, hence producing stronger turbulence, than in the middle and upper part. Few of the previous studies have clarified the matter by comparing values of *TKE* production.

At first, the inverse approach is tested on simulated datasets from a numerical model. Then, the approach is applied to current harmonics from literature and two types of current observations in Chesapeake Bay and one of its tributaries. The first type consists of moored measurements, while the second includes measurements from a bottom-mounted acoustic Doppler current profiler (*ADCP*).

ADCPs are quite new for current observations (e.g., Schott & Johns, 1987; Simpson et al., 1990; Marmorino & Trump, 1992), due to the instrument's high resolution in the vertical. Yet, few attempts have been made to utilize the increased resolution for friction-related studies in shallow waters. Thus, the present approach may provide an analytic tool to deduce frictional information from *ADCP* observations.

Objectives of this study are threefold. The first objective is to develop a simple inverse method to estimate pressure gradient force, vertical structure of eddy viscosity, and shear stress solely from field measurements of deterministic wave currents. The second is to find reasonable values for water-column effective drag coefficient and total *TKE* shear production, based on the first results. The third is to provide an enhanced analytic tool to study *ADCP* vertical observations in field.

To investigate confidence, similarity and variety in time and locality, results from analyses of independent measurements will be compared.

Chapter II reviews previous related studies on shear stress and *TKE*. Chapter III reviews inverse methods practiced in oceanography, and notes some unique points of the current approach compared to others. Chapter IV describes assumptions and justifications for linearization

of the equations of motion, the matrix system of the inverse equation, data processing methods, and a numerical model employed to test performance of the inverse method.

Chapter V describes model inputs and generated outputs, and datasets from current-meter stations and an *ADCP* station.

Chapter VI presents results of analyses, which include the estimates of pressure gradient, eddy viscosity, shear stress (both internal and bottom), depth averaged *TKE* shear production, and drag coefficient. In Chapter VII, results will be discussed on pieces of corroborative evidence and degree of success of the inversion. Conclusions are drawn in Chapter VIII, including remarks on the significance and physical implication of the inverse method and results, and possible further extension of the research.

II. SHEAR STRESS AND TURBULENCE

Knowledge of turbulent mixing processes is still meager, though it has been gradually increased owing to development of suitable instruments and techniques to observe turbulent fluctuations. In shallow waters, shear-driven turbulence has been directly measured, indirectly determined, or theoretically modeled with some closure schemes. One key subject has been the determination of vertical shear stress. The stress can be either directly observed as Reynolds' stress, or indirectly estimated from dynamic balance of the mean flow. Also, it could be determined with eddy viscosity parameterization.

A. Direct Measurement

In shallow waters, direct observations of shear stress or *TKE* have been achieved either with mechanical current meters (e.g. Francis et al., 1953; Gordon & Dohne, 1973), with electromagnetic current meters (e.g. Bowden & Fairbairn, 1956; Anwar, 1983), with acoustic Doppler systems (e.g. Seitz, 1973), or with acoustic travel-time current meters (e.g. Schröder & Siedler, 1989).

Gordon and Dohne(1973) measured the Reynolds stress R_{xz} of a vertically well mixed flow in the Choptank River on the eastern shore of Chesapeake Bay. Near maximum flow, it ranged from near zero at the surface to about 5 dynes/cm² close to the bottom (7 m deep). They also found the relation $R_{xz} \approx 0.13$ *TKE*.

Anwar(1983) measured the Reynolds stress R_{xz} , the mean velocity and salinity near the bottom of estuarine channels in U.K. and Australia. He found $0.06 \leq Ri \approx R_f \leq 0.2$ regardless of flow states (stratified or well mixed), indicating the existence of a local equilibrium layer. Here Ri and R_f denote the gradient and flux Richardson number, respectively.

A study of the mixing zone in the Elbe estuary by Schröder and Siedler(1989) revealed that temporal variation of *TKE* was strongly coherent to tidal current fluctuation at 2.5 m above the bottom. It also showed that the Reynolds stress R_{xz} changed in phase with tidal current fluctuation.

B. Indirect Estimation

Two methods have been found in the indirect estimation of shear stress. The first method involves determining friction from an equation of motion, using known horizontal pressure gradients and current profiles. The second method incorporates the law of wall. Bottom stress is estimated from a near-bottom current profile, in turn, used for the

estimation of internal stress from a water-column current profile.

With the first method, Bowden and Fairbairn(1952) estimated shearing stress profiles effective to semidiurnal tidal current from observations of surface elevation at two stations and current profiles at the middle. They showed that the amplitude of the stress increased linearly from the surface to the bottom. Also, Bowden(1960) estimated shear stress and eddy viscosity effective to residual flow in the Mersey Narrows. Maximum values of eddy viscosity occurred at mid-depth, but were about 1/10th of what were found in a well-mixed flow.

With the second method, Bowden et al.(1959) determined instantaneous shear-stress profiles and vertical eddy viscosity. At the times of acceleration, the instantaneous stress profiles showed considerable deviation from the linear variation. Estimates of the vertical eddy viscosity showed maximum near mid-depth and near times of maximum current. The maximum was approximately represented by

$$(N_z)_{\max} \approx 2.5 \times 10^{-3} \cdot UH \quad \text{II-(1)}$$

where U and H denote the depth-average amplitude of tidal current and total depth.

C. Turbulence Model

Turbulence models are based on assumptions introduced with empirical information. The Eddy-viscosity (or diffusivity) concept has been favorably used in most hydrodynamic models, mainly by virtue of its economy. In contrast to the molecular counterpart, the eddy viscosity is not a fluid property, but strongly depends on the state of turbulence, and hence may vary considerably at different spatial and temporal scales. The eddy parameterization of turbulence becomes nonsense if energy or material flux is against the gradient.

A brief review of turbulence model types helps clarifying how far the eddy concept can be applicable. Turbulence models may be classified in three categories: Prandtl mixing length model (type I), energy-equation models (type II) and stress/flux-equation models (type III) (Rodi, 1987).

The type-I model relates the eddy viscosity, N_z , in shear layers to the mean velocity gradient (e.g. Rossby & Montgomery, 1935):

$$N_z = S_M(Ri) \cdot l_m^2 \cdot |\partial_z u|$$

$$\partial_z = \frac{\partial}{\partial z}, \quad Ri = -\frac{g}{\rho} \cdot \partial_z \rho$$

II-(2)

where $S_M(Ri)$ and l_m represent a certain stability function of Ri and mixing length, respectively. The stability function usually takes the effect of stratification on purely empirical

bases. This model type is based on the assumption that turbulence is in a local-equilibrium state.

The type-II models have been used to account for advection and diffusion of turbulence. The most widely practiced model is the k - ϵ equation model, where k and ϵ represent *TKE* and its dissipation. The eddy viscosity is related to k and ϵ as

$$N_z = c \frac{k^2}{\epsilon} \quad \text{II-(3)}$$

where c is an empirical constant. The distribution of k and ϵ is determined from corresponding balance equations. In stratified flows, c can not be assumed constant, and hence needs empirical adjustment.

The type-III models have been developed to overcome limitations inherent to the type-I and -II models, especially with counter-gradient transport and anisotropy of turbulence due to gravitational effects. These Models do not employ the eddy concept any longer, instead, they solve balance equations for individual stress and flux components (e.g. Launder et al., 1975), and hence named as stress/flux models. Substantial amount of effort and cost in practicing the type-III models, however, led to developments of simplified versions (algebraic stress/flux models) (e.g. Gibson & Launder, 1978; Mellor & Yamada, 1982). In quasi-equilibrium

shear layers, some algebraic stress/flux simplifications can result in a similar form to the one in II-(2), but with the stability function treated semi-empirically, such as the level-2 closures in Mellor and Yamada (1982) or Galperin et al. (1988).

Obviously, it is not desirable to combine the turbulence-mean flow dynamics with the stress/flux (type-III) models in a practical view point. Because of the economy achievable with simpler closure models, most hydrodynamic models still employ the eddy concept (Rodi, 1987). In allowing the concept, however, turbulence models require certain number of empirical constants to be decided from measurements.

III. REVIEW OF INVERSE METHODS

A variety of inverse methods has been practiced in oceanography. An appropriate method has been often decided by the scale of problem and data characteristic (noisiness and sparsity of data).

In large-scale studies, for instance, Hogg(1987) used a least-square fit of the steady-state advective-diffusive equations to Levitus Atlas data to obtain the geostrophic flow fields and horizontal eddy diffusivities. A similar approach may be found in Fiadeiro and Veronis(1984). One common feature in the preceding works is that they used the method of singular value decomposition to solve the steady-inverse problem in a least-squares sense.

In unsteady dynamic fields, the variational optimal control technique has recently received broad attention. Since first applied in meteorology by Sasaki(1970), it has been a useful tool for variety of data-inverse or assimilation problems in oceanography (e.g. Wunsch,1988; Moore,1991; Yu & O'Brien, 1991). Briefly, this approach requires a forward model and adjoint equations driven by the misfit between model and observations. The misfit, then, is minimized in a least-squares sense. The variational method works in somewhat

automated optimization, and requires numerical computation in both the forward and backward directions. Thus, it is best suited to problems of highly transient or non-linear flow fields. Despite its theoretical beauty, it contains some drawbacks. First, it is computationally very expensive due to the doubled modeling. Second, the construction of the adjoint model is not a trivial matter at all (Moore, 1991). Third, it may be prone not only to singularity (non-uniqueness), but also to numerical instability. Also it may be subject to 'pseudo-uniqueness' caused by different initial guesses or by insufficient constraints (Panchang & Richardson, 1993).

Parameters may be obtained by fitting theoretical solutions to data. For instance, Maas and Van Haren(1987) estimated values of the depth-constant effective eddy viscosity and drag coefficient by fitting the results of harmonic analysis to theoretical solutions for the vertical frictional mode in a tidally dominated area (the Central North Sea).

Definitely, it is the most desirable inversion to solve well-posed problems directly for unknown parameters, as Bowden and Fairbairn(1952) did. Designs and/or data quality of field observations, however, may not be always satisfactory for this type of approach. We may often cope with undesirable situations in either time or space. Such conditions may render inverse problems ill-posed.

For dynamic flows characterized by a deterministic or quasi-deterministic nature, the present study introduces a simple inversion method to deal with these ill-posed problems, hence to estimate pressure gradient force and viscous term simultaneously by fitting a linearized equation of motion to data, using the eddy viscosity concept.

The approach uses results of harmonic analysis in the time domain as Maas and Van Haren(1987) did. Three good features of this approach can be listed. First, the time-vertical problem can be reduced to a vertical problem only, owing to the data reduction with harmonic analysis. Second, smoothness in the time domain is provided with the harmonic analysis. The third is that ill-posed problems may become over-determined in a least-squares sense, due to the frequency split.

There are two unique points noted in the current approach. The first is that the approach requires only current measurements in the vertical. The second is that the approach attempts the resolution of vertical structure of vertical eddy viscosity without any structural presumption.

IV. METHODS

A. Dynamic Equation

A momentum equation of three dimensional flow for shallow-water waves may be given as

$$\partial_t \vec{u} + (\vec{u} \cdot \nabla_h) \vec{u} + w \partial_z \vec{u} + \vec{f} \times \vec{u} \approx PGA + \partial_z \vec{F} \quad \text{IV-(1)}$$

with

$$\begin{aligned} \partial_t &= \frac{\partial}{\partial t}, & \nabla_h &= \left(\frac{\partial}{\partial x}, \frac{\partial}{\partial y} \right), & \partial_z &= \frac{\partial}{\partial z} \\ \vec{u} &= (u, v), & \vec{f} &= (0, 0, f) \\ PGA &= -\frac{1}{\rho} \nabla_h P, & \vec{F} &= \frac{\vec{\tau}}{\rho} = (F_{zx}, F_{zy}) \end{aligned}$$

where the symbols f , PGA and F denote Coriolis parameter, pressure gradient acceleration and kinematic (density-normalized) shear stress, respectively. Subscripts x and y designate the x - and y -directions.

The horizontal friction terms are regarded as negligible. The notion can be generally tolerable, only if flows are effectively located away from lateral boundaries. Ianniello(1979) suggests that the effective layer of such boundary influence may be on the order of 10 to 100 m in a

typical tidal channel.

In case of channel flow, the y-momentum equation and v-related terms in the x-momentum equation may be neglected, if the horizontal aspect ratio, $\delta = (\sigma^*W/C_p)^2$, and the Kelvin number, $K_E = f^*W/C_p$, are both $\ll 1$, where σ , W and C_p represent characteristic frequency, width of channel and phase velocity. Then, a simplified version of IV-(1) may be given by

$$\partial_t u + v\partial_x u + w\partial_z u \approx PGA + \partial_z F \quad \text{IV-(2)}$$

Henceforth, only the x-directional balance is considered, and subscript x in F is dropped by virtue of simplicity.

1. Linearization

The nonlinear advective terms, often called the local field acceleration, is mainly related to the along-propagation change of total-depth or cross-sectional area of the main flow conduit. Divergence of continuity also creates nonlinearity due to the flow-effective geometry change in the longitudinal direction. The advective nonlinearity may be outweighed by the divergence nonlinearity (Pingree and Maddock, 1978; Uncles, 1988). In the momentum-balance point of view, the divergence nonlinearity is smeared into the PGA term.

The advective nonlinearity may become significant only

where the total depth or cross-sectional area varies rapidly over short distance. In relatively uniform portions of estuaries and embayments, in fact, the advective terms are known to be of minor importance compared to the frictional term (Uncles, 1981; Godin, 1991). Then, the linearized version of IV-(2) becomes

$$\partial_t u \approx PGA + \partial_z F \quad \text{IV-(3)}$$

for first-order dynamics, while the advective nonlinearity is transferred to second-order dynamics.

It is also noted that the nonlinearity induces the Eulerian residual, which may not be negligible in the residual momentum balance (Ianniello, 1977). The residual term, however, becomes a matter of time-residual dynamics.

2. Decomposition

Terms u , PGA and F in IV-(3) may be split as

$$\begin{aligned} u &\approx u_0 + u_T ; & u_T &\approx \sum_{k=1}^m u_k, \\ PGA &\approx PGA_0 + PGA_T ; & PGA_T &\approx \sum_{k=1}^m PGA_k, \\ F &\approx F_0 + F_T ; & F_T &\approx \sum_{k=1}^m F_k \end{aligned} \quad \text{IV-(4)}$$

Subscript symbols 0 and T indicate time-residual and oscillating component (mostly tidal in shallow waters), respectively. The symbol m denotes the number of frequency

species (or bands). K-th species can be written in complex harmonic form as

$$\begin{aligned} u_k &= \frac{1}{2} \cdot (U_k \cdot e^{i\sigma_k t} + [U_k]^* \cdot e^{-i\sigma_k t}) \\ PGA_k &= \frac{1}{2} \cdot (G_k \cdot e^{i\sigma_k t} + [G_k]^* \cdot e^{-i\sigma_k t}) \\ F_k &= \frac{1}{2} \cdot (T_k \cdot e^{i\sigma_k t} + [T_k]^* \cdot e^{-i\sigma_k t}) \end{aligned} \quad \text{IV-(5)}$$

The symbols, U_k , G_k and T_k represent complex amplitudes, and thus include phase information. The symbol $[\]^*$ denotes complex conjugate. With IV-(4) and IV-(5) substituted in IV-(3), a vertical equation for k-th principal species is written as

$$i\sigma_k U_k = G_k + \partial_z T_k \quad \text{IV-(6)}$$

with only positive frequencies taken into account.

3. Pressure gradient acceleration

The PGA can be separated in two parts in the vertical. One is depth-independent (barotropic), and the other is depth-dependent (baroclinic):

$$\begin{aligned} PGA &= -\frac{g}{\rho} \cdot \partial_x \int_z^{\zeta} \rho \, dz \approx -g (\partial_x \zeta + \frac{1}{\rho_0} \int_z^{\zeta} \partial_x \rho \, dz) \\ &\approx -g (\partial_x \zeta + \lambda (\zeta - z)); \quad \lambda = \frac{\partial_x \rho}{\rho_0} \end{aligned} \quad \text{IV-(7)}$$

where g , ζ and ρ denote the gravity constant, surface

elevation and density, respectively. Here and henceforth, the overbar symbol indicates a depth-average. In time, equation IV-(7) can be split in time-residual and oscillating components as

$$\begin{aligned}
 \overline{PGA_0} &\approx -g \left[\partial_x \zeta_0 + \lambda_0 \frac{H}{2} - \lambda_0 \frac{H}{2} \cdot \left(1 + 2 \frac{z}{H}\right) \right] \\
 \overline{PGA_T} &\approx -g \left[\partial_x \zeta_T + \lambda_0 \zeta_T + \lambda_T \frac{H}{2} - \lambda_T \frac{H}{2} \cdot \left(1 + \frac{2z}{H}\right) \right] \\
 \lambda_0 &\approx \frac{\partial_x \overline{\rho_0}}{\rho_0}, \quad \lambda_T \approx \frac{\partial_x \overline{\rho_T}}{\rho_0}
 \end{aligned}
 \tag{IV-8}$$

Again, in complex form, k-th density species can be represented by

$$\overline{\rho_k} = \frac{1}{2} (R_k \cdot e^{i\sigma_k t} + [R_k]^* \cdot e^{-i\sigma_k t})
 \tag{IV-9}$$

where R denote complex amplitude. With negligible disturbance from internal waves, depth-average density balance for k-th species is approximately given by

$$\begin{aligned}
 \partial_t \overline{\rho_k} &\approx -\overline{u_k} \cdot \partial_x \overline{\rho_0}, \quad i \cdot \sigma_k \cdot R_k \approx -\overline{U_k} \cdot \partial_x \overline{\rho_0} \\
 \therefore \lambda_k &\approx i \frac{\partial_x \overline{U_k}}{\sigma_k} \cdot \lambda_0
 \end{aligned}
 \tag{IV-10}$$

Water depth H may be given on the order of 10^3 cm. For typical M_2 -dominant tidal flows, the frequency is $\sim 10^{-4} \text{ s}^{-1}$. Surface elevation may be given on the order of $10 - 10^2$ cm. Wavelength may be on the order of 100 km (10^7 cm). Longitudinal density variation may be on the order of 10^{-9} g/cm^4 . Then it may be given that

$$\begin{aligned}
 o(\partial_x \zeta_k) &\sim (10^{-5} - 10^{-6}) \\
 o\left(\frac{\partial_x \bar{U}_k}{\sigma_k}\right) &\sim (10^{-1} - 10^{-2}), \quad o(\lambda_0) \sim 10^{-9} \\
 o(\lambda_k) &\sim o\left(\frac{\partial_x \bar{U}_k}{\sigma_k} \cdot \lambda_0\right) \sim (10^{-10} - 10^{-11})
 \end{aligned}
 \tag{IV-11}$$

Subsequently, the barotropic part is on the order of

$$o(\partial_x \zeta_k + \lambda_0 \cdot \zeta_k + \lambda_k \cdot \frac{H}{2}) \sim (10^{-5} - 10^{-6})
 \tag{IV-12}$$

while the baroclinic part is on the order of

$$o(\lambda_k \cdot \frac{H}{2}) \sim (10^{-7} - 10^{-8})
 \tag{IV-13}$$

It is obvious that the baroclinic *PGA* is about two orders of magnitude smaller than the barotropic for shallow water waves. In other words, *PGA* in shallow water waves tends to be depth-independent, even under the influence of a longitudinal density gradient.

On the contrary, the baroclinicity becomes important in the time-residual component, thus taking a general form as

$$PGA_0 \approx a + bz \quad (a = -g\partial_x \zeta_0 ; \quad b = g\lambda_0)
 \tag{IV-14}$$

It is also noted that IV-(14) implicitly contains the leading portion of the Eulerian residual.

4. Characteristics of local dynamics

Tidal current profiles are the most appropriate for the

proposed inverse approach. Flow in Chesapeake Bay is mainly characterized by tidal currents. Dominant species (principal constituents) are reported as M_2 , S_2 , N_2 , K_1 and O_1 (Parker, 1988). Among them, M_2 is recognized as predominant. The most recognizable second-order constituents are M_4 and M_6 (Fisher, 1986).

5. Eddy viscosity parameterization

The kinematic vertical shear stress can be parameterized with eddy viscosity (N_z):

$$F = N_z \cdot (\partial_z u + \partial_x w) \approx N_z \cdot \partial_z u \quad \text{IV-(15)}$$

For dimensional reasons, N_z may be related to TKE as follows

$$N_z = S_M \cdot l \cdot k^{1/2} \quad \text{IV-(16)}$$

S_M , l and k denote a stability function, a characteristic length scale of the energy-containing motion and TKE , respectively (Rodi, 1987). When flow motion is characterized by a predominant frequency (or frequency band), the time variation of TKE may be described in two frequencies: time-mean and the frequency doubled. Regarding IV-(16), the time variation of eddy viscosity may be described in the same way.

The study involves two eddy-viscosity models in time. In the first model, the eddy viscosity is time-independent,

but depth-dependent: N_{z0} . In the second model, time-variation is included: N_{zM4} . With M_2 motion taken as predominant, the second model may be given by

$$N_z \approx N_{z0} + N_{zM4}$$

$$N_{zM4} = \frac{1}{2} \cdot (E_{M4} \cdot e^{i\sigma_{M4}t} + [E_{M4}]^* \cdot e^{-i\sigma_{M4}t}) \quad \text{IV- (17)}$$

where E_{M4} denotes complex amplitude.

6. System equations

With the eddy-viscosity model in IV-(17), the time-residual balance is given by

$$\partial_z F_0 + P G A_0 \approx \partial_z F_0 + a + b z \approx 0$$

$$F_0 \approx N_{z0} \cdot \partial_z u_0 \quad \text{IV- (18)}$$

and the first-order dynamic balance by

$$\partial_z T_k + G_k \approx i \cdot \sigma_k \cdot U_k, \quad k: M_2, S_2, N_2, K_1, O_1 \quad \text{IV- (19)}$$

The stress amplitude in complex, T_k , can be explicitly formulated for M_2 , as follows

$$T_{M2} \approx N_{z0} \cdot \partial_z U_{M2} + \frac{1}{2} E_{M4} \cdot \partial_z [U_{M2}]^* \quad \text{IV- (20)}$$

and for other principal constituents,

$$T_k \approx N_{z0} \cdot \partial_z U_k, \quad k: S_2, N_2, K_1, O_1 \quad \text{IV- (21)}$$

Due to the double-frequency variation of the eddy viscosity,

its interaction with the time-residual and M_2 flow in the stress term brings up M_4 and M_6 balance, given by

$$\partial_z T_{M4} - \frac{1}{2} \{ U_{M2} \cdot \partial_x U_{M2} + W_{M2} \cdot \partial_z U_{M2} \} \approx i \cdot \sigma_{M4} \cdot U_{M4} \quad \text{IV-(22)}$$

$$\partial_z T_{M6} \approx i \cdot \sigma_{M6} \cdot U_{M6}$$

with

$$\begin{aligned} T_{M4} &\approx N_{z0} \cdot \partial_z U_{M4} + E_{M4} \cdot \partial_z u_0 \\ T_{M6} &\approx N_{z0} \cdot \partial_z U_{M6} + \frac{1}{2} E_{M4} \cdot \partial_z U_{M2} \end{aligned}$$

Although both terms T_{M4} and T_{M6} are associated with the same parameters N_{z0} and E_{M4} , the M_4 balance, in fact, introduces the additional unknowns to be determined, $\partial_x U_{M2}$ and W_{M2} . Henceforth, only the subset, the M_6 -balance equation, is used for the analysis of the oscillating component of eddy viscosity, E_{M4} .

With definite integrations from z to 0, the equations IV-(18), IV-(19) and IV-(22) yield a linear algebraic system of equations given by

$$\begin{aligned} \partial_z u_0 \cdot N_{z0} + z a + \frac{1}{2} z^2 \cdot b &\approx 0 \\ \partial_z U_{M2} \cdot N_{z0} + \frac{1}{2} \partial_z [U_{M2}]^* \cdot E_{M4} + z G_{M2} &\approx -i \cdot \sigma_{M2} \int_z^0 U_{M2} d\hat{z} \\ \partial_z U_k \cdot N_{z0} + z G_k &\approx -i \cdot \sigma_k \int_z^0 U_k d\hat{z} \\ &(k: S_2, N_2, K_1, O_1) \\ \partial_z U_{M6} \cdot N_{z0} + \frac{1}{2} \partial_z U_{M2} \cdot E_{M4} &\approx -i \cdot \sigma_{M6} \int_z^0 U_{M6} d\hat{z} \end{aligned} \quad \text{IV-(23)}$$

The stress at the surface was assumed negligible. This assumption may be valid with tidal-momentum balance, but may not with the time-residual. To minimize the time-residual surface stress, we may need an effective time period longer than a typical time scale of local wind influence (\sim days). Otherwise, the inclusion of the time-residual component may deteriorate the inverse system. This condition may be satisfied with the time-series length of M_2-N_2 or M_2-S_2 modulation.

With the time-independent viscosity model N_{z_0} only, IV-(23) is further simplified to

$$\begin{aligned} \partial_z u_0 \cdot N_{z_0} + z a + \frac{1}{2} z^2 \cdot b &\approx 0 \\ \partial_z U_k \cdot N_{z_0} + z G_k &\approx -i \sigma_k \int_z^0 U_k dz \\ (k: M_2, S_2, N_2, K_1, O_1) \end{aligned} \quad \text{IV-(24)}$$

Each depth of estimation (or of unknowns) is located at the mid-point between two depths of knowns, where velocity complex amplitude is differentiated and integrated to the surface. Intra-layer velocity structure is assumed to be piecewise-linear at mid-depths.

With water column observations, it is often the case to miss vertical resolution near the surface and the bottom. Thus, two extra layers are defined either above the nearest point of measurement to the surface (top layer) or below the

nearest to the bottom (bottom layer). Quadratic extrapolation is used for vertical integration of currents in both layers. The constraints used for the quadratic extrapolation are:

$$\begin{aligned} \partial_z u_0 = \partial_z u_T = 0 & \quad \text{at } z=0 \\ u_0 = u_T = 0 & \quad \text{at } z=-H \end{aligned} \quad \text{IV- (25)}$$

The nearest two points to the surface or the bottom are to be used in the extrapolation.

For depth-dependent unknowns of eddy viscosity, it is necessary to determine current shears at depths of unknowns. The mid-point in the bottom layer is considered as the depth of unknown, while the point in the top layer is not, because the no-slip boundary condition can be regarded as a real measurement. Currents are differentiated linearly at all depths of unknowns by virtue of simplicity (even including the depth in the bottom layer). In this way, it is anticipated that the shear in the bottom layer may be larger than it would be.

At each depth of estimation, internal shear stress is reconstructed from the estimated viscosity and given velocity shear. Meanwhile, oscillating components of barotropic *PGA* are used to retrieve component-effective bottom stress and a drag coefficient with the depth-average momentum balance being determined, given by

$$\begin{aligned}
 (T_k)_B &= H(G_k - i\sigma_k \bar{U}_k), & \bar{U}_k &= \frac{1}{H} \int_{-H}^0 U_k dz \\
 C_d &\approx \frac{(F_T)_B}{\bar{u}_T |\bar{u}_T|}, & \bar{u}_T &= \frac{1}{H} \int_{-H}^0 u_T dz
 \end{aligned}
 \tag{IV-26}$$

A least-squares fitting is used again to estimate the drag coefficient. TKE shear production (P_s) can be calculated by multiplying internal shear stress with velocity shear. With integration of IV-(3) from z to 0, the shear production can take a form as

$$P_s \approx F \partial_z u = \partial_z u \int_z^0 (PGA - \partial_z u) dz
 \tag{IV-27}$$

When integrated from $-H$ to 0, this leads to the total water-column production, hence to the depth-average production. The depth-average can be given by

$$\bar{P}_s = \bar{u} PGA_T + \overline{u PGA_0} - \overline{u \partial_z u_T}
 \tag{IV-28}$$

where the subscript T denotes tidal component. This quantity, in fact, is equivalent to the rate of wave-energy dissipation.

B. Inverse Scheme

The linear algebraic system of equations in IV-(23) or IV-(24) has a form of $A \cdot x = d$, where A , x and d represent a design matrix ($N \times M$), a vector of unknowns ($M \times 1$) and a vector of knowns ($N \times 1$), respectively. Here, N and M denote the number of equations and the number of unknowns.

The matrix system needs to be overdetermined to get the most effective results to velocity profiles. A necessary condition is that N must be greater than or equal to M . Diagnostic measures are given in Table IV-1 for the case with or without the time-residual equation being added to the system.

Table IV-1. Necessary conditions for inverse systems to be overdetermined.

CASE	NZ MODEL	N	M	CONDITION
1	NZ_0, NZ_{M4}	$(2m+3)n$	$3n+2(m+1)$	$n \geq [1+1/m]$
	NZ_0	$(2m+1)n$	$n+2(m+1)$	$n \geq [1+1/m]$
2	NZ_0, NZ_{M4}	$(2m+2)n$	$3n+2m$	$n \geq [1+1/(2m-1)]$
	NZ_0	$2mn$	$n+2m$	$n \geq [1+1/(2m-1)]$

m: 1st-order constituents n: depths of knowns
CASE 1: with time-residual current
CASE 2: without time-residual current

It is noted that unknowns for PGA_0 are not considered in the second case. In any case, the necessary condition is satisfied with data from 2 depths. In practice, the present inverse scheme needs at least one extra depth for the quadratic extrapolations both at the top and bottom layers. Thus, the required minimum is at least 3 depths.

Since it is a least-squares problem to solve the system, the normal equation $x = (\mathbf{A}^T \cdot \mathbf{A})^{-1} \cdot (\mathbf{A}^T \cdot d)$ may be used. This approach, however, is somewhat sensitive to round-off error and the near-singularity problem, due to the construction of the covariance matrix and its inversion. The near-singularity problem will occur if two basis functions (column vectors of \mathbf{A}) or two different combinations of functions have a near-linear dependence. The *singular value decomposition* (SVD) technique is known to fix both the round-off problem and the singularity difficulty; hence it results in the best approximation in the least-squares sense (Press et al., 1990). The SVD has been one of effective tools for analysis of oceanographic data: e.g., for mode separation of current measurements (Candela et al., 1992) and for inverse analysis (Fiadeiro & Veronis, 1983; Hogg, 1987).

The SVD factorization of the matrix \mathbf{A} is given by $\mathbf{A} = \mathbf{P} \cdot \mathbf{R} \cdot \mathbf{Q}^T$. Dimensions of \mathbf{P} , \mathbf{R} and \mathbf{Q} are $N \times M$, $M \times M$ and $M \times M$, respectively. Matrices \mathbf{P} and \mathbf{Q} are column-orthogonal and

column-row-orthogonal, respectively. Hence they satisfy the eigen-property, $P^T \cdot P = Q^T \cdot Q = Q \cdot Q^T = I$ (identity matrix). R is a diagonal matrix which contains singular values (or square roots of eigenvalues of $A^T \cdot A$) in diagonal elements. The solution vector is given by $x = Q \cdot R^{-1} \cdot P^T \cdot d$.

It is a similar concept to the inversion with the *SVD* that the vertical profiles of flow acceleration may be decomposed in orthogonal modes, and that each mode is subject to being solved for unknown parameters. It is worth noting that the acceleration term in the left of IV-(3), in fact, can be decomposed in two orthogonal functions according to the Gram-Schmidt orthonormalization process:

$$\phi_1 = PGA_T - \frac{(F_T)_B}{H} \quad \phi_2 = \frac{(F_T)_B}{H} + \partial_z F_T$$

$$\int_{-H}^0 (\phi_1 \cdot \phi_2) dz = 0 \quad \text{IV-(29)}$$

F_{TB} : bottom shear stress

C. Data Processing

At each current station, a principal axis (PA) is determined, using measurements at all depths, on which the longitudinal component, u , is projected. The PA angle, θ_{PA} is computed as follows

$$\theta_{PA} = \tan^{-1} \left(\frac{\sqrt{(SS)^2 + 4 \cdot (SP)^2} - SS}{2 \cdot (SP)} \right)$$

$$SS = \sum_{i=1}^n \sum_{j=1}^{l(i)} u_{ij}^2 - v_{ij}^2 \quad SP = \sum_{i=1}^n \sum_{j=1}^{l(i)} u_{ij} \cdot v_{ij}$$

IV- (30)

where $l(i)$ and n represent the number of observations in i -th depth time-series and the total number of measurement depths at one station.

Current records are processed with the method of *least-squares harmonic analysis (LSHA)* to determine amplitudes and phases of principal constituents. Phases are adjusted to the beginning of deployment year. It is noted that the method of *LSHA* also employs the *SVD* algorithm. Vertically ordered amplitudes and phases of the specified frequencies are provided to the next inverse system.

Overall numerical confidence is checked with measure of singularity (ν) and misfit (γ), defined as

$$\nu = \log_{10} \frac{\max(r)}{\min(r)}, \quad 0 \leq \nu \leq 16$$

$$\gamma = \frac{\chi^2}{d^T \cdot d}, \quad 0 \leq \gamma \leq 1$$

IV- (31)

where r represents a vector containing diagonal elements of the matrix R , and $\chi^2 = (d - A \cdot x)^T (d - A \cdot x)$. The number of significant digits in double precision is 16. Since computation is to be done in double precision, the number 16 is taken to be a critical upper limit of ν . In a practical

sense, however, the upper limit is set at 10 (v_c) for safer interpretations. It is noted that input for inversion is assumed noise-free.

D. Numerical Model

To test the performance of the inverse method, a simple numerical model is used. The model is designed to resolve vertical structure of rectilinearly oscillating currents in vertically well mixed state. The prototype can be found in Fang and Ichiye (1983). With the Coriolis terms included, the authors investigated the vertical structure of tidal currents caused by bottom friction. The prototype successfully simulated the observation by Bowden and Fairbairn (1952).

To meet the current objective, the equation of motion is given by

$$\partial_z u = -g \partial_x \zeta + \partial_z F \quad \text{IV- (32)}$$

With the z -coordinate positive upward ($0 \leq z' \leq H$), the kinematic shear stress is formulated by the mixing-length theory as:

$$F = N_z \cdot \partial_z u$$

$$N_z = l^2 \cdot |\partial_z u|, \quad l = \kappa (z' + z_0) \cdot \left(1 - \frac{z'}{\beta \cdot H}\right) \quad \text{IV- (33)}$$

The symbols κ , z_0 and β denote the von Kármán constant,

bottom roughness and a shape factor of the mixing length ($\beta \geq 1.0$), respectively. If one uses $\beta = 1 + z_0/H$, the mixing length becomes exactly parabolic. Model boundary conditions are set by $u = 0$ at the bottom and by $F = 0$ at the surface.

Since the current structure is very sensitive to the bottom roughness z_0 , log-transformed coordinate with M vertical grids is used as follows,

$$\begin{aligned}\Delta z^{(u)} &= \Delta s \exp(s^{(u)} + s_0) \\ \Delta z^{(F)} &= \Delta s \exp(s^{(F)} + s_0) \\ \Delta s &= \frac{\ln(1+H/z_0)}{M-0.5} \quad s_0 = \ln(z_0) \\ s^{(u)} &= 0, \Delta s, 2\Delta s, \dots \quad s^{(F)} = \frac{\Delta s}{2}, \frac{3\Delta s}{2}, \dots\end{aligned}$$

Vertical grids are staggered for the velocity and stress. Computation is done in a fully implicit scheme, to avoid possible numerical instability occurring when tridiagonal matrices are solved along time, that is, the vertical derivative is evaluated at unknown-time levels.

Model run is designed to stop when two consecutive time windows for output have cross-correlation values over 0.95 at all sampling depths. The length of a time window is 8 tidal cycles for M_2 single forcing, or determined by a maximum modulation period for multi-constituent forcing.

Simulated current observations, sampled at designated depths, are processed with the method of *LSHA*, then given to the inverse system. To see the degree of fitness, inverse

estimates of eddy viscosity are compared with *LSHA* results of model-generated eddy viscosity.

E. Computer Codes

Routines for *PA*, *LSHA* with *SVD* and numerical model were coded in the C++ language (Borland C++ for DOS). Computations of inversion were done with 'MATLAB for Windows' running on a 486-PC.

V. DATA AND ANALYSES

Three kinds of data are involved in analyses. They include data simulated by a numerical model, data from literature, and field measurements, respectively.

Analyses were done in 2 categories. The first category defines if the system equation includes time-residual component (flag 1: 0 or 1), while the second does if solution includes the time-varying component of eddy viscosity, N_{2M4} (flag 2: 0 or 1). Accordingly, a code 'Ixx' will be used for the identification of analysis-type in subsequent chapters, where 'xx' represents a combination of flag 1 and flag 2: I00, I01, I10 and I11.

A. Model-Simulated Data

The von Kármán constant (κ), physical roughness (z_0) and the shape factor (β) were taken as 0.4, 0.1 cm and 1.15, respectively. Pressure gradient acceleration was given by a sum of oscillatory forcings,

$$PGA = \sum_{i=1}^m \sigma_i \sqrt{\frac{g}{H}} \cdot (\zeta_0)_i \cos(\sigma_i \cdot t - (\frac{3\pi}{2} + \Phi_i)) \quad V-(1)$$

where ζ_0 and Φ represent amplitude and phase of surface elevation. Total water depth, H , was set to 15 m. Model runs were done with 200 vertical grids and a 120-second time interval.

Two test runs, named as 'run A' and 'run B', were considered, with $m = 1$ (M_2) and $m = 5$ (M_2, S_2, N_2, K_1, O_1).

Table V-1 describes the amplitude-phase values of surface-elevation and the corresponding PGA input.

Time series of current and vertical eddy viscosity were constructed at 12 designated depths, according to output specification given in Table V-2.

Due to negligible time-residual signals, analyses were performed with approaches I00 and I01.

Table V-1. Numerical-model input: pressure gradient accelerations.

	Period (hrs)	ζ_0 (cm)		Φ ($^\circ$)		$\ PGA\ $ (10^{-3}cm/s^2)
		run A	run B	run A	run B	
M_2	12.4206	50	50	0	0	5.6790
S_2	12.0000		10		40	1.1756
N_2	12.6584		8		80	0.8916
K_1	23.9345		5		100	0.2947
O_1	25.8193		3		120	0.1639

Table V-2. Numerical-model output specification.

Series length	4.1 days (run A); 29.0 days (run B)
Time interval	30 minutes
Depth range	0.6 ~ 13.8 m (u); 1.2 ~ 14.4 m (N_2)
Depth interval	1.2 m

B. Literature Data

A total of 4 sets of harmonic data were taken from 2 literature studies to verify the performance of the present method using real data.

Three sets were from the work of Bowden and Fairbairn(1952), which included 1 semidiurnal constituent of surface elevations and currents derived from three 24h records (records 2, 7 and 11) at 2 stations (the West and East, 9.45km apart). The goal of their study was to deduce frictional stresses in the middle station. Pressure gradients were determined from the elevation harmonics at the West and the East stations, while the current harmonics were determined from either one of the two stations. It is further noted that those records were claimed to have given significant results.

The fourth set was from a similar study to the above by Wolf(1980). The set included 3 semidiurnal constituents (M_2 , S_2 and N_2) of surface elevations and bottom currents at 2 stations (stations 10 and 12), and of 2 water-column currents at the mid-station (station 11). Pressure gradients were determined in the same manner as above. Bottom current harmonics at the stations 10 and 12 were linearly interpolated to give the mid-station values.

The inverse method uses only current harmonic data of one fixed station, hence results are station-specific rather

than longitudinal averages. The analysis-type I00 was applied.

C. Field Data

Two kinds of field data were analysed. The first included deployments of moored current-meter arrays, and the second included an *ADCP* deployment. A total of 8 current stations, 7 with moored instruments and 1 with an *ADCP*, were involved in analyses. All stations are in Chesapeake Bay and one of its tributaries (the York River). The location map of current stations is illustrated in Fig. V-1. In the map, 6 identification labels were used to designate localities: 'AL' for a station near Allmondsville, 'CL' for a station near Clay Bank, 'YM' for 3 stations at the mouth of the York River, 'LB' for a station in the lower bay, 'HP' an *ADCP* station near Horn Point, and 'UB' a station in the upper bay. Overall sampling years span from 1982 to 1991 (~10 years). It is noted that the present study uses datasets not specifically designed for the inverse approach.

1. Moored current measurements

Each of 7 datasets consists of time-series at various depths at one mooring station. Geographic location is also summarized in Table V-3. All of them are located at the middle of major flow conduit (effective flow channel), away

from lateral-friction effects (> 100 m).

Five stations were occupied by Virginia Institute of Marine Science. They are located in the estuarine part of the York River, named as 'Clay', 'Allm', 'Y0.0', 'RB' and 'Tu91', which were were organized in 2 groups. The first group includes 2 stations, which are 5km apart in the upper York ('Clay' and 'Allm'). The second group includes 3 stations, which are closely located each other within a circle of radius < 100 m at the mouth of the York River ('Y0.0', 'RB' and 'Tu91').

Two stations were occupied by the National Ocean Survey (NOS). They are located in the bay mainstem, one in the lower bay ('NOS066') and the other in the upper bay ('NOS121').

Tables V-4 to V-7 describe deployment information, including total depth of water column, measured depth, deployment time and instrument type.

Two instrument types were involved: Inter-Ocean Model S4 (IO-S4) and Grundy (Gr) current meter. The first one is electromagnetic, while the other is mechanical.

Tables V-4 and V-5 are given for two groups in the York River. More details on the first set can be found in data reports by Sisson et al.(1991) and by Kuo et al.(1993). Table V-6 describes deployment information on two stations in the bay mainstem. More details can be found in a report

by Parker (1988).

In all, measurements were at 3~4 depths in the vertical. Due to the low vertical resolution, either the approach I00 or I10 was employed.

To investigate if it is necessary to include time-residual component, the types I00 and I10 were both applied to datasets of 'Clay' and 'Allm', because of similar experimental conditions at two stations (proximity and synchronism). Other sets were analysed with the approach I10.

At the station 'Tu91', total deployment length is ~118 days. The whole deployment is divided in 3 segments ('Tu91a', 'Tu91b', 'Tu91c'). At the station 'NOS066', 2 deployments are explicitly separated by ~2 month gap, named as 'NOS066a' and 'NOS066b'. The station 'NOS121' has a year-long time series. The entire series is split in 4 segments ('NOS121a', 'NOS121b', 'NOS121c', 'NOS121d') (Table V-7).

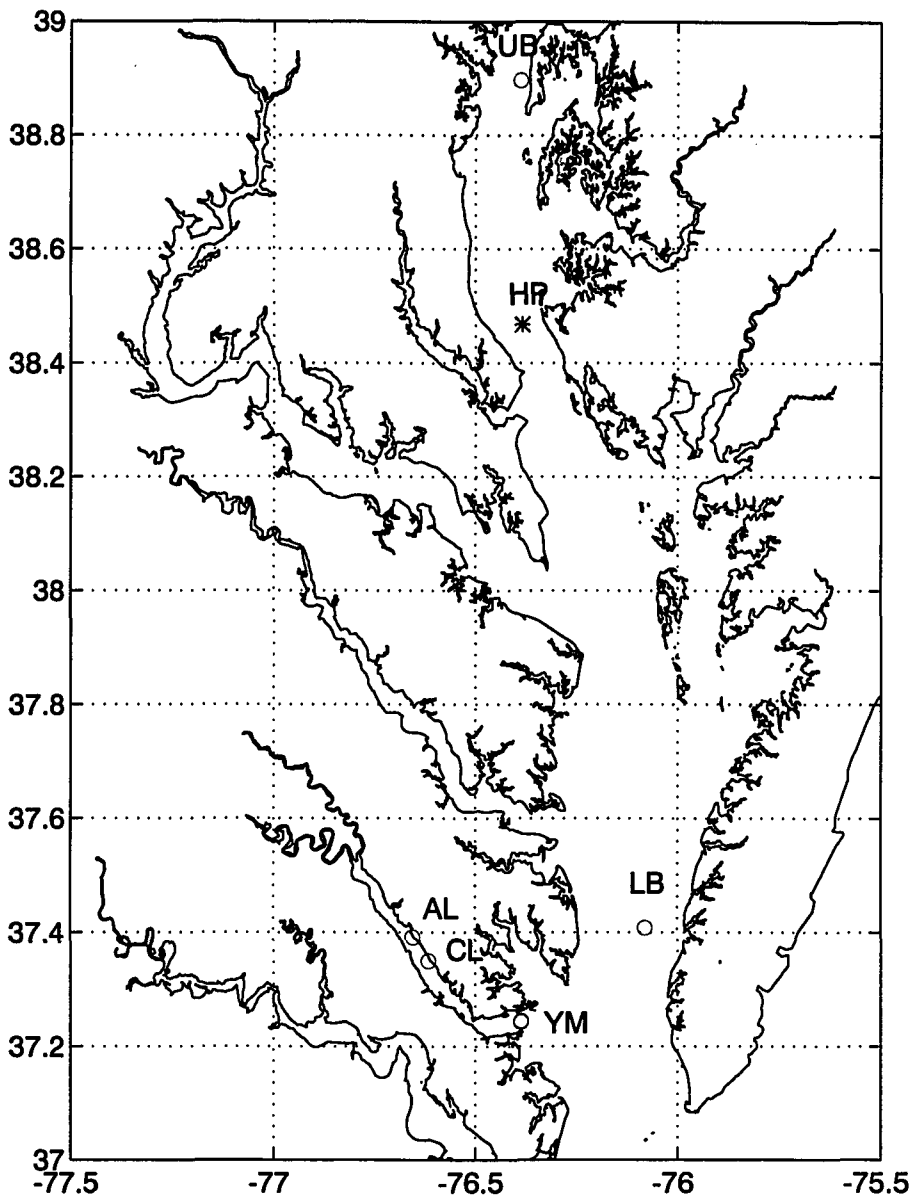


Fig. V-1. Overview of current stations in Chesapeake Bay and one of its tributaries.

Table V-3. Location of mooring stations.

	STATION	LAT. (N)	LONG. (W)	DIST.* (km)
York River	Clay ¹	37° 21.0'	76° 37.0'	26
	Allm ²	37° 23.5'	76° 39.3'	31
	Y0.0 ³	37° 14.7'	76° 23.2'	0
	RB ⁴	37° 14.7'	76° 23.2'	0
	Tu91 ⁵	37° 14.6'	76° 23.2'	0
Bay	NOS066	37° 24.5'	76° 04.8'	51
	NOS121	38° 53.8'	76° 23.3'	216.4

*: upstream distance from the relative mouth

[Upper York]

1. station off Clay Bank 2. station off Allmondsville

[York mouth]

3. 0.0 km from the mouth 4. buoy-station 'RB' 5. station 'Tue Marshes'

Table V-4. Deployment information in the upper York.

YORK	DEPTH (m)		DEPLOYMENT		Δt (min)	TYPE
	H	z	Begin	End		
Clay	8.7	-1.7	11/10/89	01/11/90	10	IO-S4
		-3.7	11/10/89	01/10/90		
		-5.7	11/23/89	01/10/90		
		-7.7	11/10/89	01/10/90		
Allm	8.7	-1.7	11/10/89	12/08/89	10	IO-S4
		-3.7	11/10/89	01/10/90		
		-5.7	11/10/89	01/10/90		
		-7.7	11/10/89	01/10/90		

[Most complete record: 11/23/89 - 12/08/89 (~19 days)]

Table V-5. Deployment information at the York mouth.

YORK	DEPTH (m)		DEPLOYMENT		Δt (min)	TYPE
	H	z	Begin	End		
Y0.0	16.7	-1.5	7/19/88	9/14/88	5	IO-S4
		-6.5	7/19/88	9/14/88		
		-11.5	7/19/88	9/14/88		
		-15.7	7/19/88	9/14/88		
RB	17.3	-1.3	7/06/89	9/01/89	30	IO-S4
		-6.5	7/13/89	9/07/89		
		-11.5	7/06/89	9/07/89		
		-16.3	7/06/89	9/07/89		
Tu91	19.5	-1.5	5/29/91	9/23/91	30*	IO-S4
		-6.0	5/29/91	9/23/91		
		-10.0	5/29/91	9/23/91		
		-18.5	5/29/91	9/23/91		

[All stations in different years]

*: Sampling-time interval was not constant through deployments due to the internal-clock battery failure. Time information was recovered by reading external-clock, instead.

Table V-6. Deployment information in the bay mainstem.

BAY	DEPTH (m)		DEPLOYMENT		Δt (min)	TYPE
	H	z	Begin	End		
NOS 066	21.7	-4.6	04/08/82	05/10/82	10	Gr
			07/22/82	08/09/82		
	-12.2	04/08/82	05/10/82			
		07/22/82	08/09/82			
-20.1	04/16/82	05/10/82				
	-19.2	07/22/82	08/09/82			
NOS 121	24.1*	-6.7	12/06/82	01/10/82	10	Gr
	23.8	-5.9	04/05/83	05/26/83		
			06/09/83	07/05/83		
	-12.2	08/22/83	12/05/83			
		12/06/82	01/10/82			
	-11.4	04/05/83	05/26/83			
		06/09/83	08/04/83			
	08/22/83	09/07/83				
		09/22/83	10/24/83			
	11/01/83	12/05/83				
	-21.7	12/06/82	01/10/83			
		-21.4	04/05/83	05/26/83		
	06/09/83		07/19/83			
08/22/83	09/07/83					
09/22/83	12/05/83					

*: Total depth of the station 'NOS121' was 24.1 m during the first deployment period ('82), and 23.8 m during the rest (lateral shift \approx 20 m).

Table V-7. Split deployment information with moorings.
 (E: early, M: middle, L: late)

STATION	BEGINS	LENGTH (days)	SEASON
Tu91a	5/29/91	35	E-Summer
Tu91b	7/3/91	41	M-Summer
Tu91c	8/14/91	42	L-Summer
NOS066a	4/8/82	32	M-Spring
NOS066b	7/7/82	18	M-Summer
NOS121a	12/6/82	35	E-Winter
NOS121b	4/5/83	50	M, L-Spring
NOS121c	6/9/83	90	Summer
NOS121d	9/22/83	74	M, L-Fall

2. ADCP measurement

An ADCP dataset consists of a vertical array of a month-long time-series, sampled with a bottom-mounted ADCP by Horn Point Environmental Laboratories, University of Maryland, Cambridge, Maryland, USA. Configuration and deployment information of the ADCP are described in Tables V-8 and V-9 respectively.

One bin represents a triangular-shaped averaging window in the ADCP system. The size of the window is 2 times the depth-cell size (DCS). The depth of the first bin becomes 1 DCS above the blank-after-transmit (BT) zone. Thus, with the BT given 0.5 m, the first bin is placed at 25.5 m below the surface, i.e. $DT - (DCS + BT)$. In the same manner, the last bin is placed at 0.5 m above the surface, and hence becomes an imaginary bin not to be counted at all.

Only 25 bins were actually logged. It turned out that the 25th bin was often turned off and on again. Thus, only 24 bins (1 ~ 24), were retained for the next steps. Without the 25th bin, the bin-depth ranges from 2.5 m (24th bin) to 25.5 m (1st bin) below the surface, with the total depth $H = 27.3$ m (height of the instrument = 0.3 m).

Since the set had relatively high resolution in the vertical, both approaches I10 (PGA, N_{z0}) and I11 (PGA, N_{z0}, N_{zM}) were used.

Table V-8. ADCP system configuration.

System frequency	1.229 MHz
Transducer shape; facing	convex; up
Beam angle (BA)	20°
Number of depth-cells (N_{dc})	27
Depth of transducer (DT)	27 m below MLW*
Depth-cell size (DCS)	1 m
Blank after transmit (BT)	0.5 m
Pings per ensemble	240
Ensemble length	4 minutes
Percent good threshold (PGT)	25 %

*: Mean Low Water

Table V-9. ADCP deployment information.

Location	38° 28.1'N 76° 23.1'W
Length of deployment	4/26/90~6/02/90 (37 days)
Mean salinity	17.5 psu
Mean temperature	15 °C (range: 10~20 °C)
Sound absorption coef., α	$\alpha = f(15 \text{ °C}, 17.5 \text{ psu})$
Speed of sound, C_s	$C_s = f(\text{ens. temp.}, 17.5 \text{ psu})$
Post-averaging interval	20 minutes

VI. RESULTS

For tabular presentation of PGA_T and shear stresses, the symbols A and Φ are used to represent amplitude and phase, with a convention $Y = A \cos(\sigma t - \Phi)$ being implied. The phase is always given in degrees.

Three figure plates are used to illustrate current harmonic profiles and inversion results from each dataset. The plates are designated by adding letters 'a', 'b' and 'c' to caption numbers. The plates consist of 4, 4 and 2 subplots, respectively. In illustrating the vertical structure of profiles, 6 symbol/line combinations are used to represent multiple constituents: 'o' with dashed line (M_2), dashed line (S_2), 'o' (N_2), '+' (K_1), 'x' (O_1) and '*' (time-residual).

The first plate illustrates current-amplitude profiles, current-phase profiles, amplitudes/phases of depth-average currents, and PGA_T amplitudes/phases, in left-right/top-bottom subplot-sequence. It must be noted that the last subplot represents output to inverse analysis, while the first 3 do input. Current-amplitude profiles are represented by deviations from the depth-average amplitude

of each constituent, scaled by a scaling factor U_s (amplitude of the M_2 depth-average). Current-phase profiles are represented by deviations from the depth-average phase of each constituent. Amplitudes/phases of depth-average currents and of PGA_T are illustrated by polar-compass plots. Amplitudes are scaled by U_s and G_s (amplitude of M_2 PGA_T).

The second plate illustrates amplitudes/phases of bottom stresses, eddy viscosity profile, amplitude profiles of internal stress, phase profiles of internal stress, in the same subplot-sequence as in the first plate. Stress amplitudes are normalized by a scaling factor F_s (amplitude of M_2 bottom stress). Eddy viscosities are scaled by a scaling factor defined by $Nzs = \kappa/e * H * \sqrt{F_s}$, where e denotes the base of natural logarithms (cf. VII-(2)).

The third plate contains two subplots. The first subplot illustrates hysteresis between generated time series of bottom stress and depth-average current. The slope, determined by least-squares, provides an estimate of C_d (cf. IV-(26)). Second subplot illustrates generated time series of depth-average TKE shear production.

Each set of results is associated with one of 4 inversion types (cf. p35): I00, I01, I10 or I11.

A. Tests on Model-Simulated Data

Current amplitudes and phases were obtained from model time series sampled at 12 depths, using the method of *LSHA*. Vertical profiles are illustrated in Fig. VI-A-1a (run A) and Fig. VI-A-2a (run B).

Here and henceforth, the symbol Δ in tables represents the deviation of result from a reference. The deviations are given in % for amplitude, and in $^{\circ}$ for phase.

1. Run A (M_2 forcing)

PGA_T estimates are presented in Table VI-1. Estimates for the experiment I00 are also illustrated in Fig. VI-A-1a. Deviations from the model are less than 0.4% for amplitude and 3.2° for phase. When the experiment type is switched from I00 to I01, estimation is improved by 0.1% for amplitude and 2.3° for phase.

Estimates of N_{z_0} are presented in Table VI-2. Both experiments recover structural similarity to the model (same depths of apparent maximum; decrease toward surface and bottom). Deviations from the model are less than 13% at all depths but 60 cm above the bottom. The large deviation at 60 cm above the bottom (factor ~ 6 underestimation in both experiments) is due to the linear differentiation in the bottom layer ($-15.0\text{m} \leq z \leq -13.8\text{m}$). In fact, the factor 6 is close to the derivative ratio with linear and log-profile at the depth: $\sim \ln(1200/z_0)/2 \approx 5$.

Table VI-1. Inversion experiments on data from the model-run A: pressure gradient acceleration PGA_T . (A: 10^{-3} cm/s²)

PGA_T	M	I00	Δ	I01	Δ
M_2 A	5.679	5.658	-0.4%	5.664	-0.3%
Φ	270.0	266.8	-3.2°	269.1	-0.9°

M: model-generated

Table VI-2. Inversion experiments on data from the model-run A: eddy viscosity N_{20} . (unit: cm²/s)

z/H	M	I00	Δ (%)	I01	Δ (%)
-0.08	25.5	25.2	-1.2	28.8	12.9
-0.16	44.6	42.6	-4.5	48.0	7.6
-0.24	62.3	58.7	-5.8	65.8	5.3
-0.32	78.1	72.8	-6.8	80.4	2.9
-0.40	90.3	83.3	-7.8	91.5	1.3
-0.48	98.7	90.4	-8.4	98.5	-0.2
-0.56	101.9	93.0	-8.7	100.6	-1.3
-0.64	99.8	90.3	-9.5	97.0	-2.8
-0.72	91.0	81.9	-10.0	87.4	-4.0
-0.80	75.3	67.1	-10.9	71.1	-5.6
-0.88	51.6	45.0	-12.8	47.4	-8.1
-0.96	19.6	3.3	-83.2	3.4	-82.7

M: model-generated

Estimates of $N_{z_{M4}}$ bear deviations less than 27% for amplitude and less than $\sim 22^\circ$ for phase at all depths except 60cm above the bottom (Table VI-3). Deviations are substantially higher than those of N_{z_0} estimates. It is certain, however, that the overall structure of the model profiles is recovered (depth of maximum, decrease toward the surface and bottom).

Table VI-3. Inversion experiment on data from the model-run A (I01): eddy viscosity $N_{z_{M4}}$. (A: cm^2/s)

z/H	A(M)	A(I01)	$\Delta(\%)$	$\Phi(\text{M})$	$\Phi(\text{I01})$	$\Delta(^{\circ})$
-0.08	16.0	11.8	-26.2	36.3	14.8	-21.5
-0.16	28.0	20.7	-26.0	33.3	15.5	-17.8
-0.24	39.3	29.4	-25.1	30.1	14.0	-16.1
-0.32	49.0	38.4	-21.6	26.3	13.9	-12.4
-0.40	56.9	45.2	-20.5	22.6	11.2	-11.4
-0.48	62.1	50.7	-18.4	18.5	9.1	-9.4
-0.56	64.7	53.1	-17.9	14.6	6.8	-7.8
-0.64	63.0	52.8	-16.2	9.9	3.6	-6.3
-0.72	57.9	48.5	-16.2	5.1	-0.1	-5.2
-0.80	47.9	40.0	-16.5	-0.5	-4.3	-3.8
-0.88	33.0	26.7	-19.1	-6.8	-9.1	-2.3
-0.96	12.6	20.2	60.3	-15.2	-11.9	3.3

M: model-generated

2. Run B (5-constituent forcing)

Primarily, results of inversion include estimates of PGA_T (M_2 , S_2 , N_2 , K_1 , O_1) and eddy viscosity (N_{z0} , N_{zM4}). PGA_T estimates are presented in Table VI-4. Estimates for the experiment I00 are also illustrated in Fig. VI-A-2a. Amplitudes and phases are deviated from the model within ~7% and 12° in both experiments I00 and I01. Little improvement is observed in deviations with the switch of experiment from I00 to I01: maximum improvement is 0.4% for amplitude and 2.1° for phase in M_2 constituent.

Estimates of N_{z0} are presented in Table VI-5. It is shown that structural similarity is recovered in both experiments (same depths of apparent maximum; decrease toward surface and bottom). Deviation from the model is less than 13% (I00) or less than 11% (I01) at all depths but 60cm above the bottom. The factor ~6 underestimation is again due to the linear differentiation in the bottom layer ($-15.0m \leq z \leq -13.8m$).

Table VI-4. Inversion experiments on data from the model-run B: pressure gradient acceleration PGA_T . (A: 10^{-3} cm/s²)

PGA_T		M	I00	Δ	I01	Δ
M_2	A	5.679	5.643	-0.6%	5.659	-0.2%
	Φ	270.0	266.4	-3.6°	268.5	-1.5°
S_2	A	1.176	1.142	-2.9%	1.142	-2.9%
	Φ	310.0	302.9	-7.1°	303.3	-6.7°
N_2	A	0.892	0.911	2.1%	0.91	2.0%
	Φ	350.0	342.2	-7.8°	342.6	-7.4°
K_1	A	0.295	0.274	-7.1%	0.274	-7.1%
	Φ	10.0	358.5	-11.5°	359.3	-10.7°
O_1	A	0.164	0.156	-4.9%	0.156	-4.9%
	Φ	30.0	18.3	-11.7°	19.1	-10.9°

M: model-generated

Table VI-5. Inversion experiments on data from the model-run B: eddy viscosity N_{z0} . (unit: cm²/s)

z/H	M	I00	Δ (%)	I01	Δ (%)
-0.08	26.4	26.2	-0.8	29.4	11.4
-0.16	46.1	44.2	-4.1	49.4	7.2
-0.24	64.5	61.0	-5.4	67.6	4.8
-0.32	80.7	75.3	-6.7	82.9	2.7
-0.40	93.3	86.8	-7.0	94.8	1.6
-0.48	101.9	93.7	-8.0	101.8	-0.1
-0.56	105.4	96.3	-8.6	103.8	-1.5
-0.64	103.0	93.6	-9.1	100.3	-2.6
-0.72	94.0	84.8	-9.8	90.4	-3.8
-0.80	77.7	69.4	-10.7	73.5	-5.4
-0.88	53.3	46.5	-12.8	49.0	-8.1
-0.96	20.2	3.5	-82.7	3.6	-82.2

M: model-generated

Estimates of N_{2M4} bear deviations less than 34% for amplitude and less than $\sim 26^\circ$ for phase at all depths but 60cm above the bottom (Table VI-6). Again, it is shown that overall structure is recovered (depth of maximum, decrease toward the surface and bottom).

Table VI-6. Inversion experiment on data from the model-run B (I01): eddy viscosity N_{2M4} . (A: cm^2/s)

z/H	A(M)	A(I01)	$\Delta(\%)$	Φ (M)	Φ (I01)	$\Delta(^{\circ})$
-0.08	15.1	10.0	-33.8	32.5	6.8	-25.7
-0.16	26.6	17.6	-33.8	29.9	7.2	-22.7
-0.24	37.1	25.4	-31.5	26.6	7.0	-19.6
-0.32	46.6	32.7	-29.8	23.0	5.6	-17.4
-0.40	54.1	38.6	-28.7	19.4	5.2	-14.2
-0.48	59.3	43.2	-27.2	15.6	2.2	-13.4
-0.56	61.4	45.6	-25.7	11.6	0.1	-11.5
-0.64	60.2	45.4	-24.6	7.2	-2.7	-9.9
-0.72	55.1	41.8	-24.1	2.5	-5.9	-8.4
-0.80	45.8	34.7	-24.2	-2.7	-10.2	-7.5
-0.88	31.5	23.4	-25.7	-8.9	-14.5	-5.6
-0.96	12.0	1.8	-85.0	-17.0	-16.0	1.0

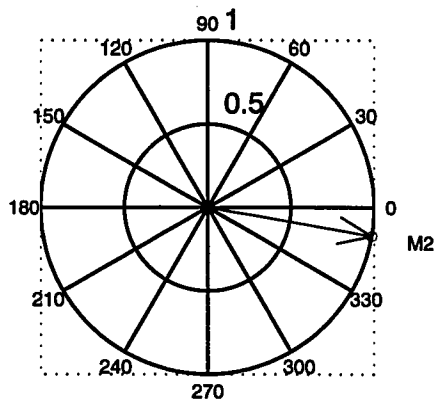
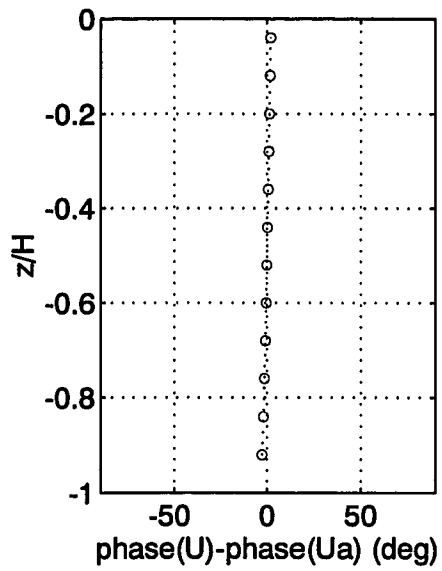
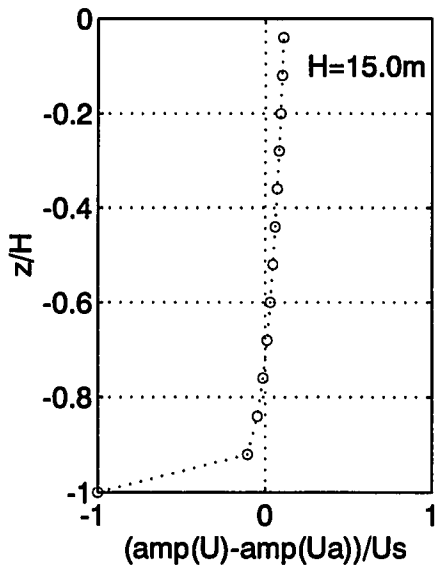
M: model-generated

3. Diagnostics

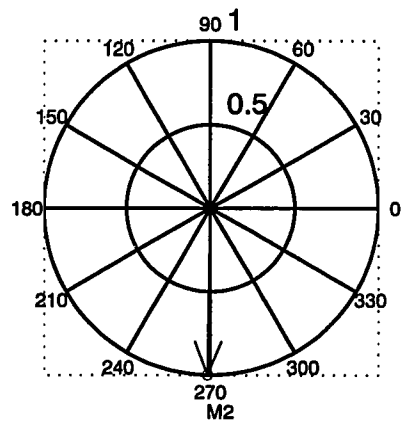
Measures of singularity (ν) and misfit (γ) are given in Table VI-7. Values of ν are less than the predefined limit $\nu_c (= 10)$. Values of γ are in order of $10^{-5} - 10^{-6}$.

Table VI-7. General measures of numerical confidence in analyses of model-generated datasets.

	Run A		Run B	
	I00	I01	I00	I01
ν	6.3	6.4	6.3	6.4
γ	5.9e-06	7.7e-07	1.2e-05	7.4e-06



Ua/Us: Us=38.7



G/Gs: Gs=5.66E-3

Fig. VI-A-1a. Model-run A: Current structure (M2) and PGA_T estimates.

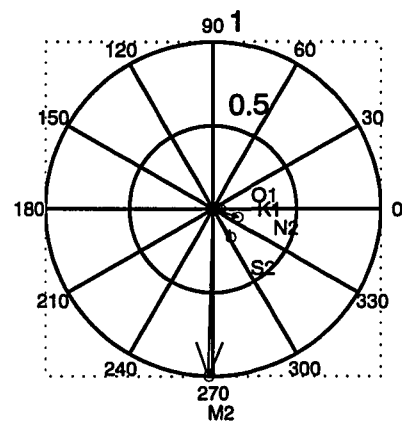
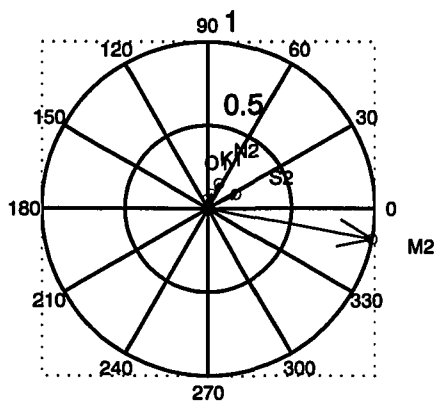
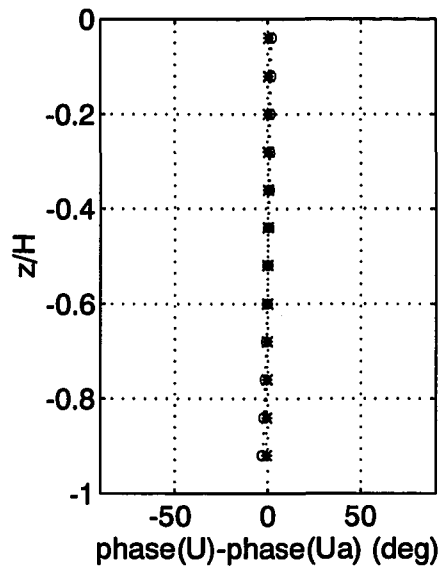
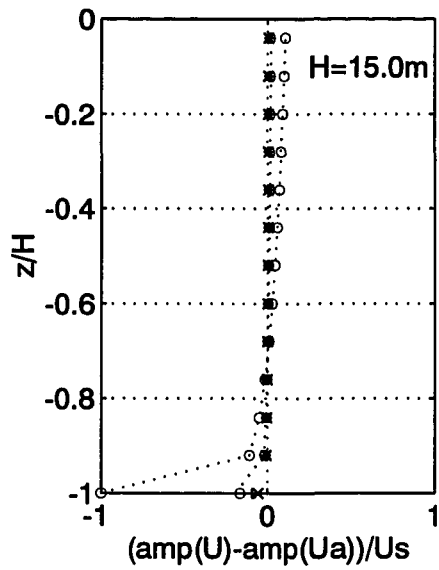


Fig. VI-A-2a. Model-run B: Current structure (5 constituents) and PGA_r estimates.

B. Results with Literature Data

Literature datasets allowed only type I00 analysis, due to the absence of residual currents and low resolution in depth (3~4 depths). Results of inversions are given in Tables VI-8 and VI-9. Since only PGA_T and current profiles are regarded as direct measurements in literature, comparisons are made only for PGA_T estimates.

With inversions of 3 sets of M_2 current profiles in Bowden and Fairbairn(1952), PGA_T estimates show maximum deviations of ~12% for amplitude and ~16° for phase from the measured values (Table VI-8).

With inversion of a set of current profiles for 3 semidiurnal constituents in Wolf(1980), PGA_T estimates show maximum deviations of ~10% for amplitude and ~8° for phase from the measured values (Table VI-9).

Overall measures of numerical significance are given in Table VI-10. An order increase is observed in misfit (γ), regarding the model experiments. Measures of singularity (ν) remain on ~6.

Table VI-8. Inversion of data from Bowden and Fairbairn(1952): pressure gradient acceleration PGA_T . (A: 10^{-3} cm/s²)

PGA		BF52	I00	Δ
Record 2	A	8.58	8.54	-0.5%
	Φ	203.1	187.6	-15.5°
Record 7	A	10.18	11.41	12.1%
	Φ	210.7	200.1	-10.6°
Record 11	A	8.25	8.93	8.2%
	Φ	199.2	190.5	-8.7°

Table VI-9. Inversion of data from Wolf(1980): pressure gradient acceleration PGA_T . (A: 10^{-3} cm/s²)

PGA		Wolf80	I00	Δ
M ₂	A	9.472	8.506	-10.2%
	Φ	148.6	156.3	7.7°
S ₂	A	3.205	2.968	-7.3%
	Φ	199.5	198.9	-0.6°
N ₂	A	1.664	1.577	-5.2%
	Φ	138.5	133.5	-5.0°

Table VI-10. General measures of numerical confidence in analyses of literature datasets.

	BF52			Wolf80
	Record 2	Record 7	Record 11	
ν	5.5	6.4	5.8	5.9
γ	1.6e-04	3.5e-04	5.2e-04	9.8e-04

C. Results with Current Mooring Data

Since the mooring stations had only 3 or 4 depths of measurement, estimation of N_{2M} is not considered. Analyses were performed basically with time-residual information (approach I10) on a total of 13 datasets (2 at 2 stations in the upper York, 5 at 3 stations in the lower York, 6 at 2 stations in the bay mainstem).

1. Results in the upper York

In addition to the I10 approach, inversions without time-residual information (approach I00) were tested. Results are presented in Table VI-11 to VI-16. As a reference, a mean is taken from estimates due to both approaches. Without knowing any true reference, the symbol $|\Delta|$ is used to represent absolute deviation from the mean.

At the station 'Clay', both analysis types show little variation in PGA_T estimates (Table VI-11). Deviations from the mean values are $\leq 0.1\%$ for amplitude and $< 2^\circ$. Deviations in N_{20} estimates are $< 4\%$ (Table VI-12). The maximum 3.6% deviation occurs at $0.31H$ ($H = 8.7$ m) below the surface.

At the station 'Allm', deviations in PGA_T estimates are $\leq 0.4\%$ for amplitude and $< 7^\circ$ for phase (Table VI-13). N_{20} estimates show little variation with the switch of analysis

type at all depths but $0.31H$ below the surface (Table VI-14).

Table VI-11. Inversions at the station 'Clay': pressure gradient acceleration PGA_T . (A: 10^{-3} cm/s²)

PGA_T		I10	I00	$ \Delta $
M ₂	A	7.38	7.39	0.1%
	Φ	173.3	173.4	0.05°
S ₂	A	1.08	1.08	0.0%
	Φ	164.8	165.9	0.55°
N ₂	A	1.41	1.41	0.0%
	Φ	335.2	335.3	0.05
K ₁	A	0.5	0.5	0.0%
	Φ	174	174.2	0.1°
O ₁	A	0.29	0.29	0.0%
	Φ	289.4	292.7	1.65°

Table VI-12. Inversions at the station 'Clay': eddy viscosity N_{z0} . (unit: cm²/s)

z/H	I10	I00	$ \Delta $ (%)
-0.310	5.8	5.4	3.6
-0.540	10.2	10.5	1.4
-0.770	12.3	12.6	1.2
-0.943	2.9	2.9	0

Table VI-13. Inversions at the station 'Allm': pressure gradient acceleration PGA_T . (A: 10^{-3} cm/s²)

PGA_T		I10	I00	$ \Delta $
M ₂	A	8.16	8.14	0.1%
	Φ	180.3	180.3	0.00°
S ₂	A	1.16	1.17	0.4%
	Φ	141.9	154.2	6.15°
N ₂	A	1.73	1.72	0.3%
	Φ	342	342	0.00°
K ₁	A	0.48	0.48	0.0%
	Φ	168	167.6	0.20°
O ₁	A	0.3	0.3	0.0%
	Φ	234.7	232	1.35°

Table VI-14. Inversions at the station 'Allm': eddy viscosity N_{z0} . (unit: cm²/s)

z/H	I10	I00	$ \Delta $ (%)
-0.310	2.6	5.0	31.6
-0.540	6.4	6.4	0.0
-0.770	10.3	10.3	0.0
-0.943	2.9	2.9	0.0

The overall measures of numerical significance are given in Table VI-15. Compared to the model experiments, a factor of 100 increase is observed in misfit (γ). On the contrary, measures of singularity (ν) increased to ~ 7 in the I10 analyses, while they decreased to ~ 5 in the I00 analyses. Values of ν are obviously less than ν_c .

By excluding the $u_0(z)$ -associates (i.e. equation and unknowns of PGA_0), it is observed that the approach I00 gives a smaller value of singularity than does the approach I10. Meanwhile, γ is reduced a little at the station 'Clay' and by one order at the station 'Allm'. Thus, it seems that the inclusion of the $u_0(z)$ -associates bears a trade-off.

Results due to I10 analyses are illustrated in Fig. VI-C-1a, VI-C-1b, VI-C-1c for the station 'Clay', and in Fig. VI-C-2a, VI-C-2b and VI-C-2c for the station 'Allm'. Scaling factors and drag coefficients are summarized in Table VI-16. Overall values of Nzs and C_d are $144.3 \text{ cm}^2/\text{s}$ and 0.45×10^{-3} .

An apparent maximum of scaled eddy viscosity of 0.87×10^{-1} at the station 'Clay', and 0.70×10^{-1} at the station 'Allm', both occurred at $0.77H$ below the surface. From the apparent maxima, the viscosity tends to decrease both upward and downward from this point. Amplitude profiles of internal stress show concave-upward structure (Fig. VI-C-1b, Fig. VI-C-2b).

Maximum bottom stress in time seems to reach ~ 1.8 cm^2/s^2 at both stations. Time-series of depth-average *TKE* production show frequency modulation (Fig. VI-C-1c, Fig. VI-C-2c). It appears that monthly (apogean-perigean) modulation is significant as well as spring-neap modulation. Perigean-spring maxima seem to reach ~ 0.1 cm^2/s^3 (~ 0.01 Watts/ m^3) with overall running average of $0.04 - 0.05$ cm^2/s^3 ($0.004 - 0.005$ Watts/ m^3). Then, the water-column *TKE* produced in a day is roughly estimated as $3 - 4$ K Joules/ m^2 .

Estimates of 2 PGA_0 -coefficients (a and b in VI-(14)), due to the analysis type I10, are given in Table VI-17 for both stations 'Clay' and 'Allm'. Overall values of a and b are $\sim 1.15 \times 10^{-3}$ and $\sim 3.19 \times 10^{-6}$. The corresponding effective surface slope and λ_0 are -1.17×10^{-6} and 3.25×10^{-9} cm^{-1} (cf. IV-(8)).

Table VI-15. General measures of numerical confidence at the upper York stations.

	Clay		Allm	
	I10	I00	I10	I00
v	7.2	4.7	7.1	4.6
γ	8.8e-04	8.4e-04	1.1e-03	1.0e-04

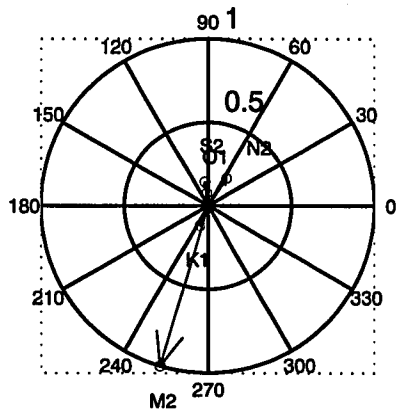
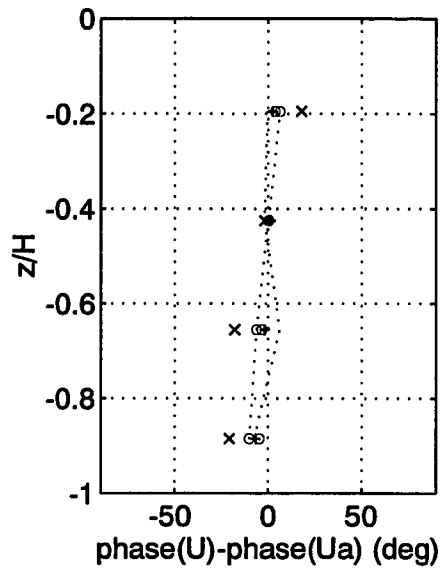
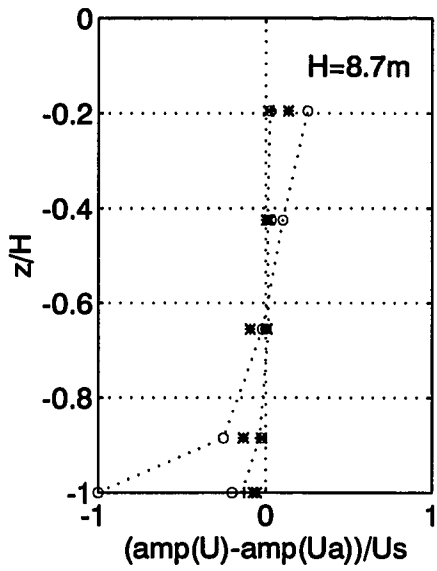
Table VI-16. Scaling factors and drag coefficients at the upper York stations. (G_s : 10^{-3} cm/s², C_d : 10^{-3})

	Clay	Allm	Mean
Us	47.3	52.0	49.7
Gs	7.38	8.16	7.77
Fs	1.23	1.32	1.28
Nzs	141.8	146.9	144.3
C_d	0.42	0.49	0.45

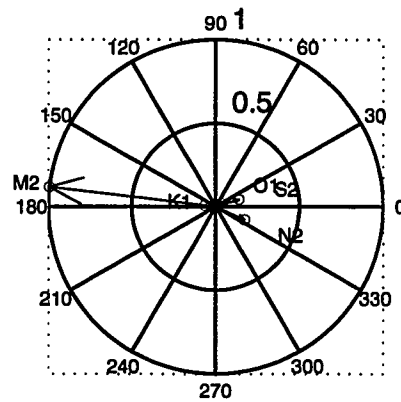
Table VI-17. Time-residual pressure gradient acceleration, PGA_0 , at the upper York stations. (a : 10^{-3} cm/s², b : 10^{-6} 1/s²)

PGA_0	Clay	Allm	Mean
a	1.25	3.33	1.15
b	1.05	3.05	3.19

(a > 0: seaward, b > 0: landward)

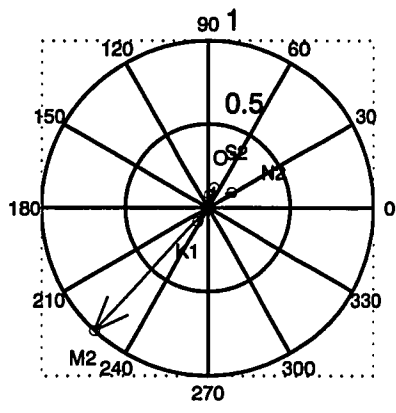


$U_a/U_s: U_s=47.3$

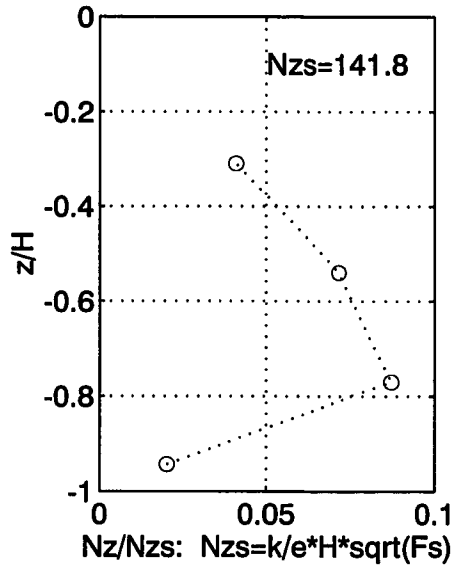


$G/G_s: G_s=7.38E-3$

Fig. VI-C-1a. Currents and estimates of PGA_r at the station 'Clay'.



[bottom stress]/Fs: Fs=1.23



Nz/Nzs: Nzs=k/e*H*sqrt(Fs)

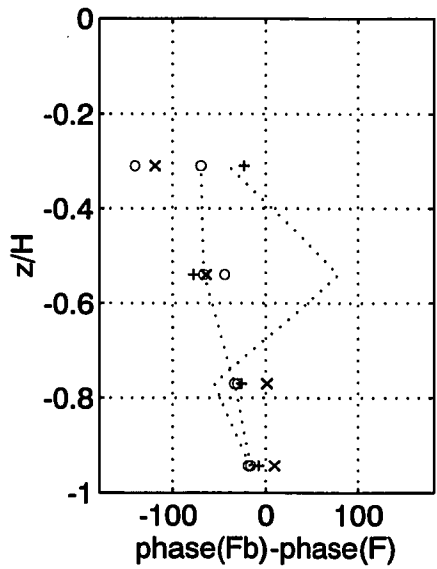
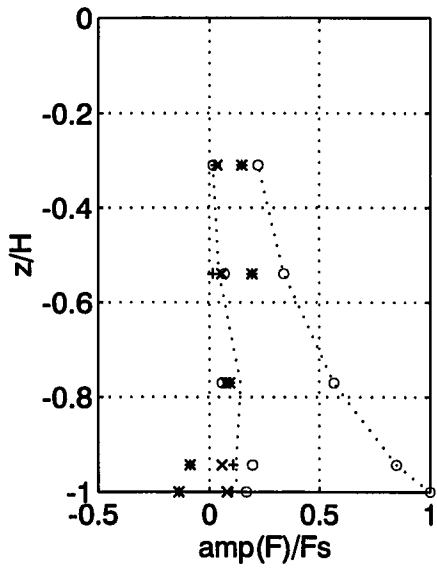


Fig. VI-C-1b. Eddy viscosity and shear stress at the station 'Clay'.

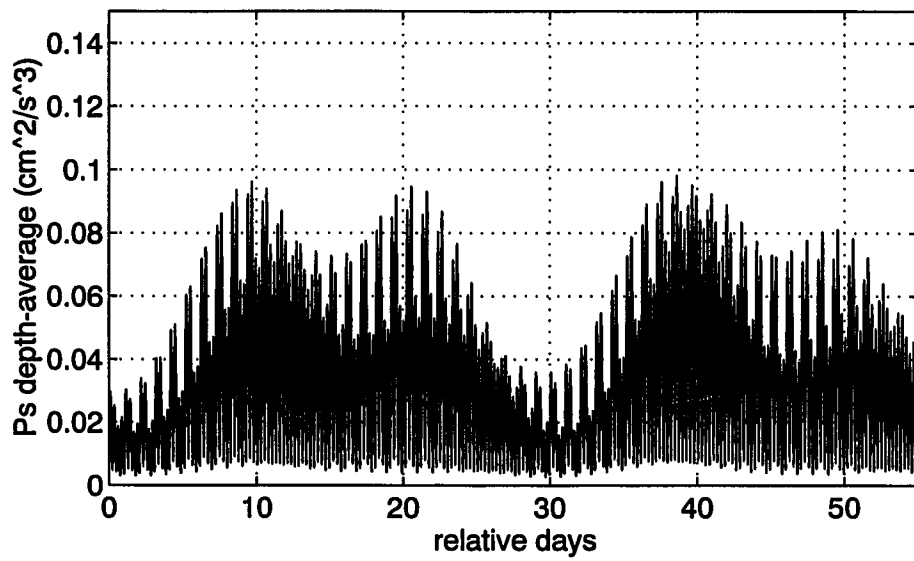
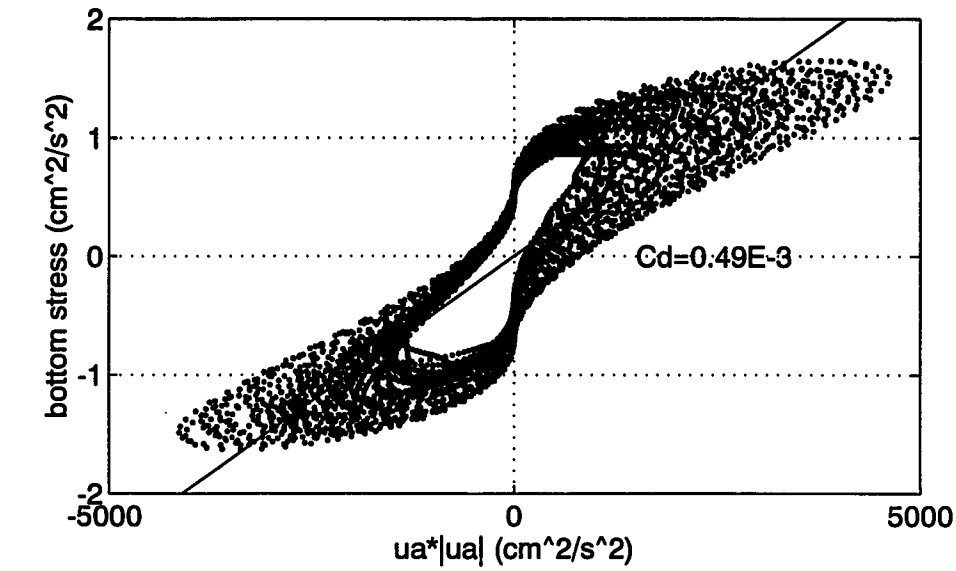


Fig. VI-C-1c. Hysteresis and depth-average *TKE* production at the station 'Clay'.

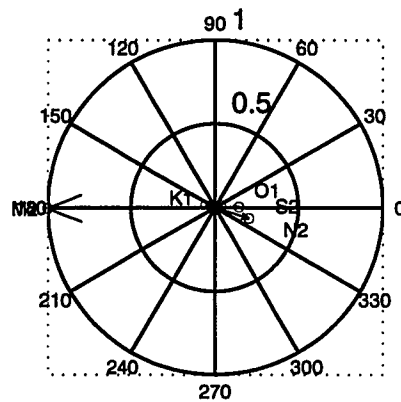
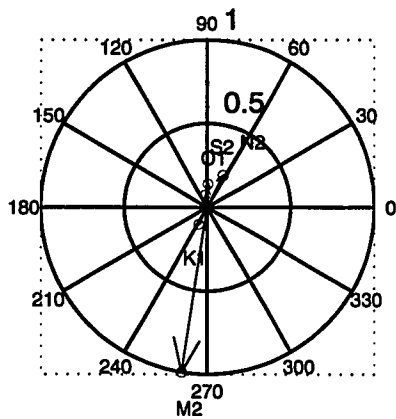
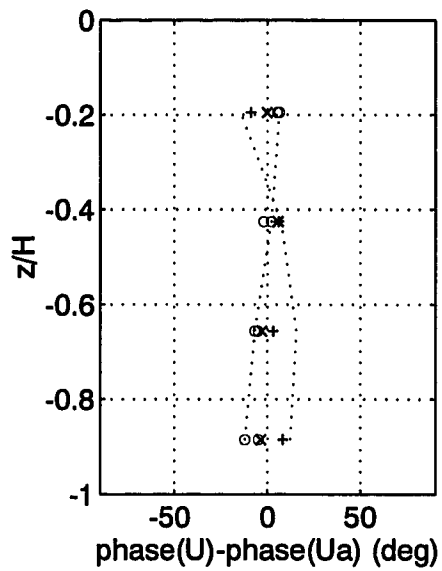
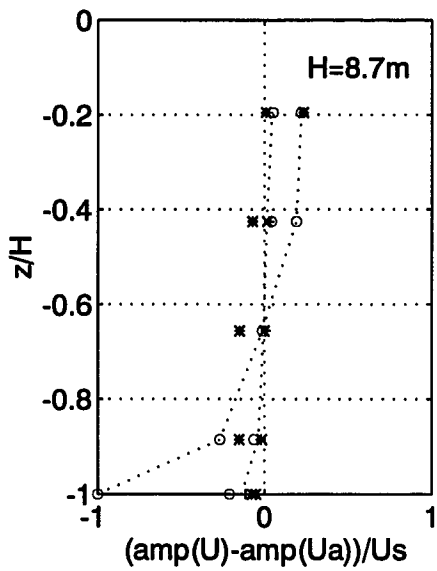
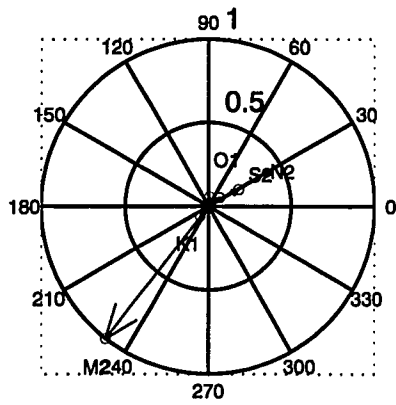


Fig. VI-C-2a. Currents and estimates of PGA_r at the station 'Allm'.



[bottom stress]/Fs: Fs=1.32

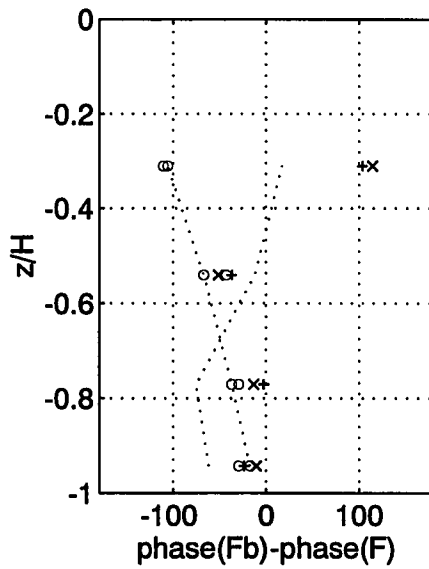
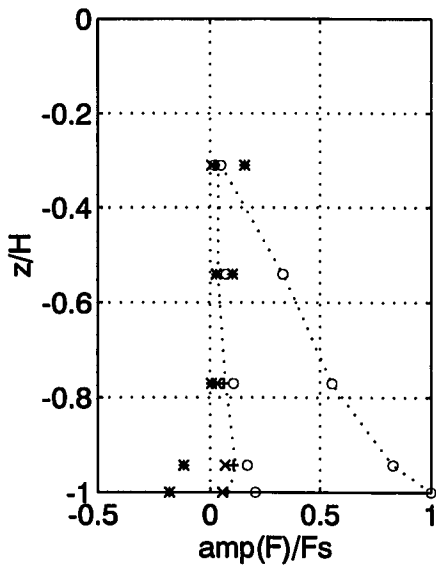
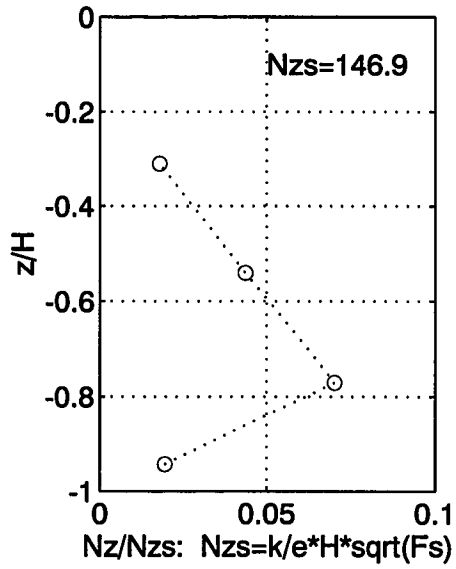


Fig. VI-C-2b. Eddy viscosity and shear stress at the station 'Allm'.

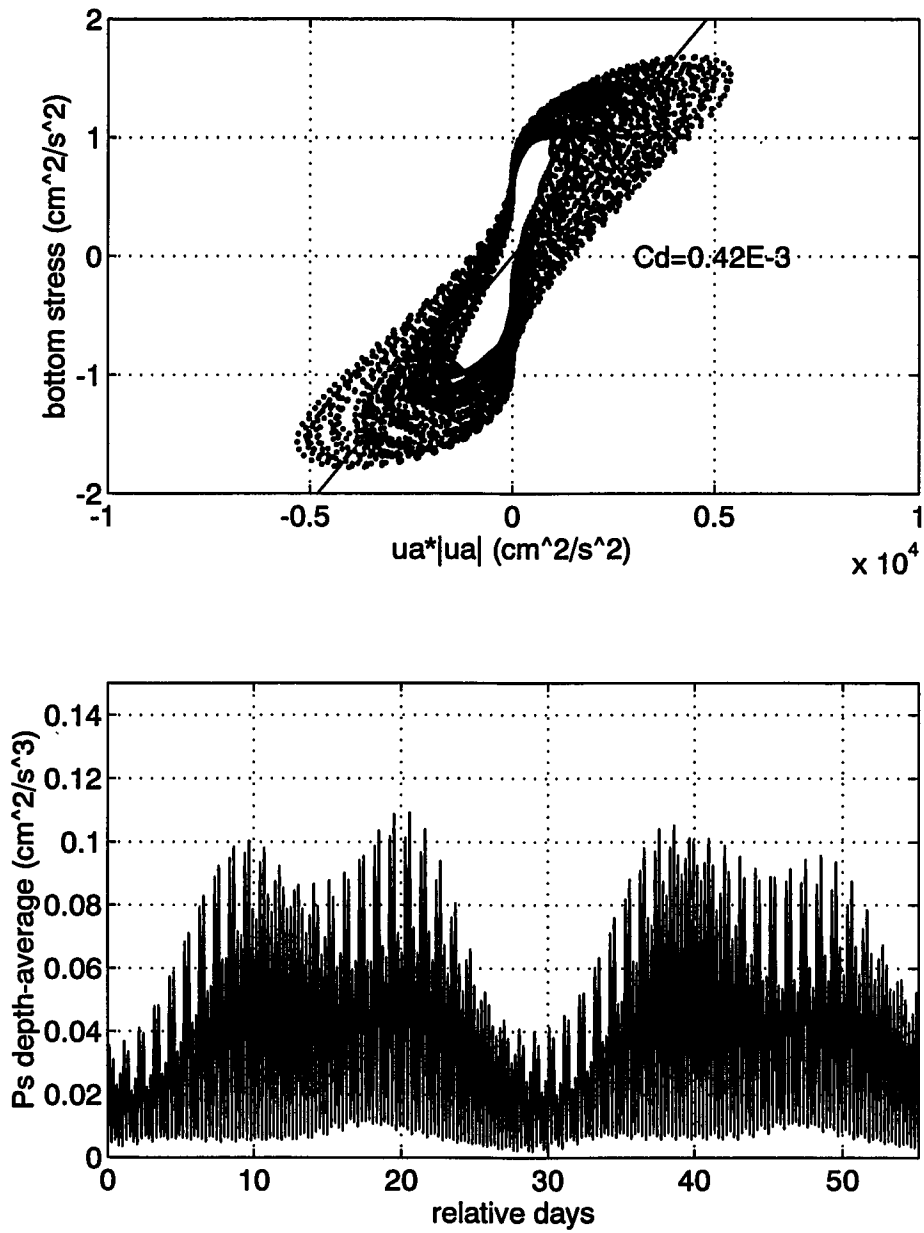


Fig. VI-C-2c. Hysteresis and depth-average *TKE* production at the station 'Allm'.

2. Results in the lower York

Total 5 datasets were involved with the analysis-type I10: 'Y0.0', 'RB', 'Tu91a', 'Tu91b' and 'Tu91c'. Results are illustrated in 5 sets of figure plates: [Fig. VI-C-3a,b,c] for 'Y0.0', [Fig. VI-C-4a,b,c] for 'RB', [Fig. VI-C-5a,b,c] for 'Tu91a', [Fig. VI-C-6a,b,c] for 'Tu91b' and [Fig. VI-C-7a,b,c] for 'Tu91c'.

Dynamic features may be characterized by scaling factors (**Us**, **Gs**, **Fs**, **Nzs**) and C_d estimates at the stations. They are summarized in Table VI-18. Eddy-viscosity scale factor, **Nzs**, ranges 265 - 331 cm²/s. Among the split segments at the station 'Tu91', it appears that **Nzs** of 'Tu91b' is 20 - 30 cm²/s higher than others. Drag coefficient, C_d , ranges $[0.9 - 1.2] \times 10^{-3}$. Apparently, C_d seems the lowest in early/mid-summer ('Y0.0', 'Tu91a'), and becomes higher after mid-summer.

Apparent maximum of scaled eddy viscosity ranges $[0.25 - 1.23] \times 10^{-1}$, occurring at $0.7H - 0.8H$ below the surface. Among the split segments ('Tu91a'~'Tu91c'), the maximum increases as time advances (Table VI-19). At all stations, estimated amplitude profiles of internal stress show upward-concave structure (Fig. VI-C-3b, 4b, 5b, 6b, 7b). Degree of the concavity seems much higher than that of the upper York stations.

Maximum values of bottom stress in time appear to be

1.8, 1.9, 1.8, 2.0, and 1.5 cm^2/s^2 ('Y0.0', 'RB', 'Tu91a', 'Tu91b', 'Tu91c'). As in the upper York, time-variation of depth-average *TKE* production is modulated (Fig. VI-C-3c, 4c, 5c, 6c, 7c). It seems the monthly modulation is more prominent than in the upper York. Perigeon-spring-diurnal maxima appear to reach $\sim 0.04 \text{ cm}^2/\text{s}^3$ at 'Y0.0' (Fig. VI-C-3c), $\sim 0.04 \text{ cm}^2/\text{s}^3$ at 'RB' (Fig. VI-C-4c), $\sim 0.02 \text{ cm}^2/\text{s}^3$ at 'Tu91a' (Fig. VI-C-5c), $\sim 0.04 \text{ cm}^2/\text{s}^3$ at 'Tu91b' (Fig. VI-C-6c) and $\sim 0.02 \text{ cm}^2/\text{s}^3$ at 'Tu91c' (Fig. VI-C-7c).

Estimates of 2 PGA_0 -coefficients (*a* and *b*) are given in Table VI-20. Overall values of *a* and *b* are 0.25×10^{-3} and 0.38×10^{-6} . Corresponding effective surface slope and λ_0 are -0.26×10^{-6} and $0.39 \times 10^{-9} \text{ cm}^{-1}$, factor ~ 5 and ~ 8 reduced values compared to the upper-York estimates. At the station 'Tu91', estimates from 'Tu91a' (early summer) are significantly lower (\sim factor 2) than the other two.

Overall measures of numerical significance are given in Table VI-21. Compared to the model experiments, a two-order of magnitude increase is observed in misfit (γ). Measures of singularity (ν) are ~ 8 ($< \nu_c$), increased by ~ 1 from those of the upper York stations.

Table VI-18. Scaling factors and drag coefficients at the lower York stations. (G_s : 10^{-3} cm/s²; C_d : 10^{-3})

	Y0.0	RB	Tu91a	Tu91b	Tu91c	Mean
Us	31.8	30.3	30.8	30.9	28.5	30.5
Gs	4.86	4.74	4.72	4.71	4.43	4.69
Fs	1.16	1.36	1.18	1.33	1.06	1.22
Nzs	264.5	296.6	312.1	331.0	295.9	300.0
C_d	0.91	1.20	0.94	1.15	1.15	1.07

Table VI-19. Scaled maximum of eddy viscosity and its vertical location at the lower York stations. (N_{z0}/Nzs : 10^{-1})

	Y0.0	RB	Tu91a	Tu91b	Tu91c
N_{z0}/Nzs	0.60	0.36	0.25	0.63	1.23
z/H	-0.81	-0.80		-0.73	

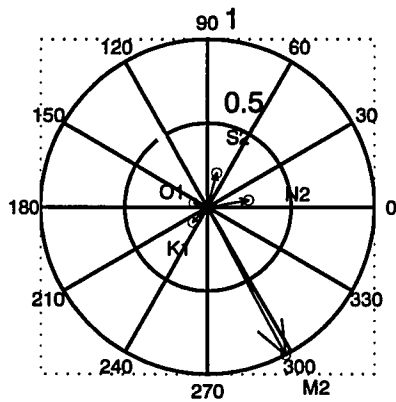
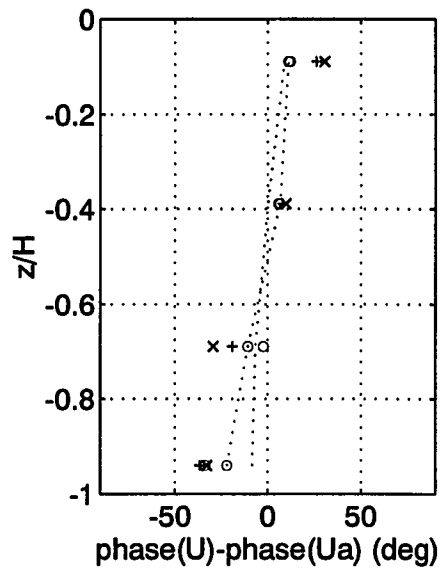
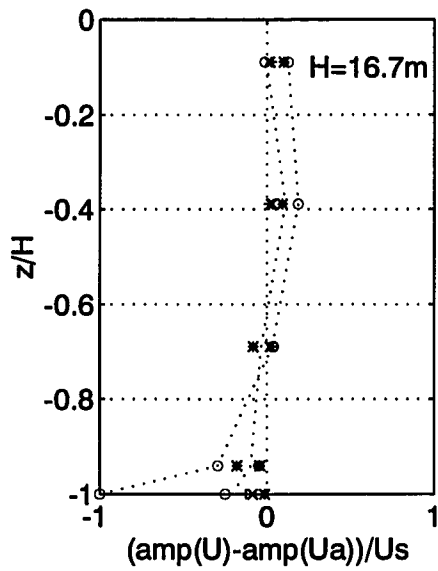
Table VI-20. Estimates of time-residual pressure gradient acceleration, PGA_0 , at the lower York stations. (a : 10^{-3} cm/s², b : 10^{-6} 1/s²)

PGA_0	Y0.0	RB	Tu91a	Tu91b	Tu91c	Mean
a	0.33	0.29	0.13	0.26	0.26	0.25
b	0.51	0.50	0.19	0.37	0.34	0.38

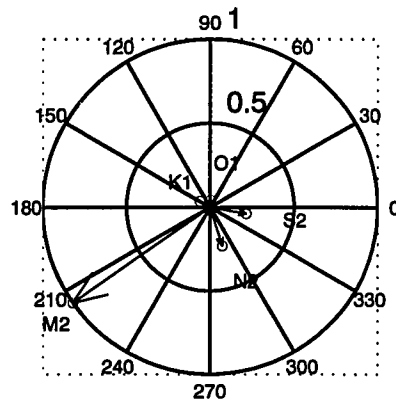
($a > 0$: seaward, $b > 0$: landward)

Table VI-21. General measures of numerical confidence at the lower York stations.

	Y0.0	RB	Tu91a	Tu91b	Tu91c
v	8.2	8.3	8.1	8.4	8.4
γ	9.9e-04	2.6e-03	5.6e-04	7.2e-04	9.0e-04

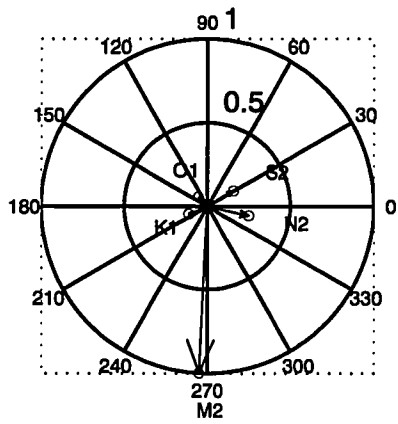


Ua/Us: Us=31.8



G/Gs: Gs=4.86E-3

Fig. VI-C-3a. Currents and estimates of PGA_r at the station 'Y0.0'.



[bottom stress]/Fs: Fs=1.16

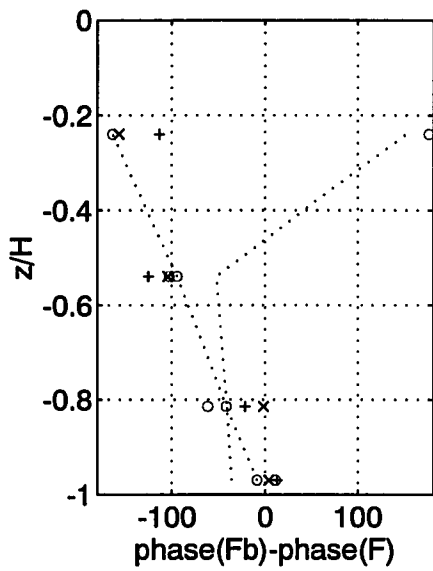
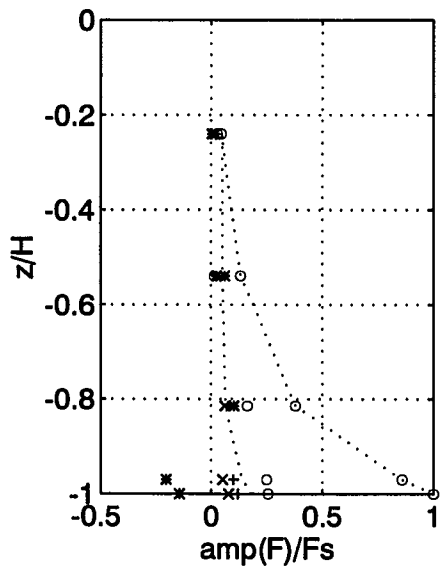
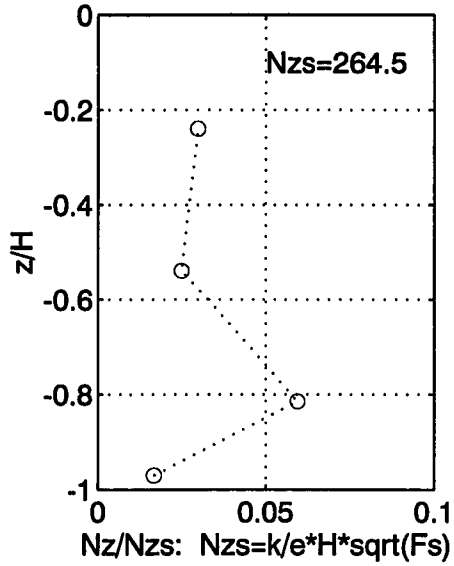


Fig. VI-C-3b. Eddy viscosity and shear stress at the station 'Y0.0'.

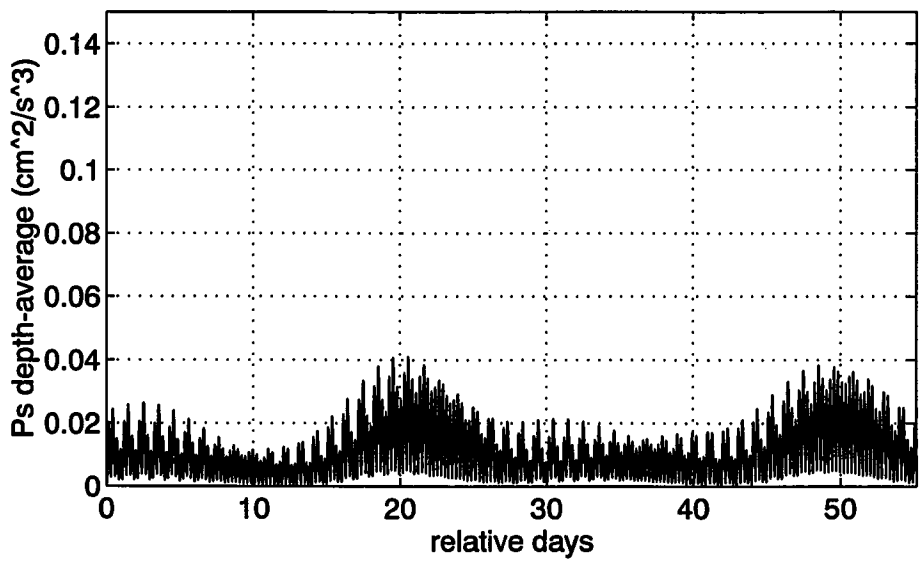
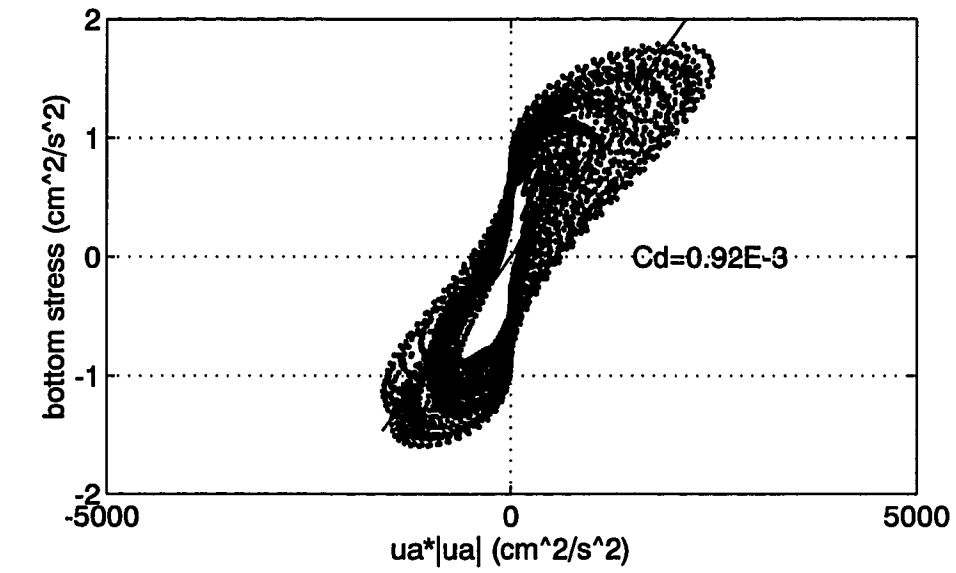
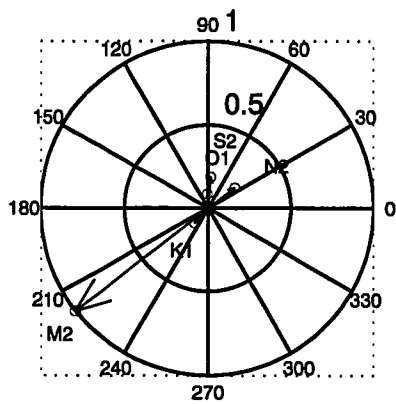
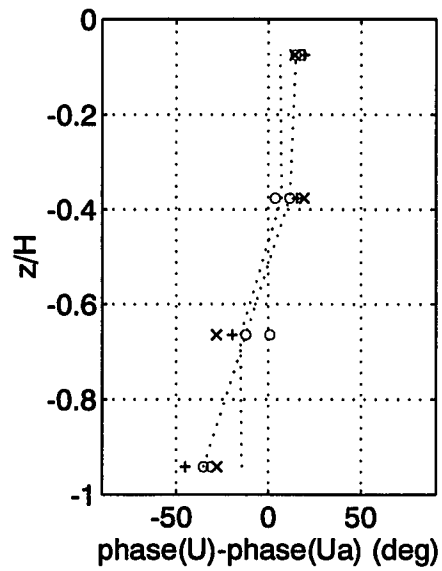
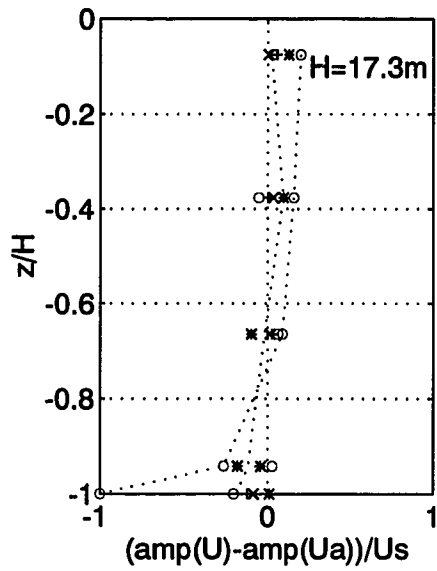
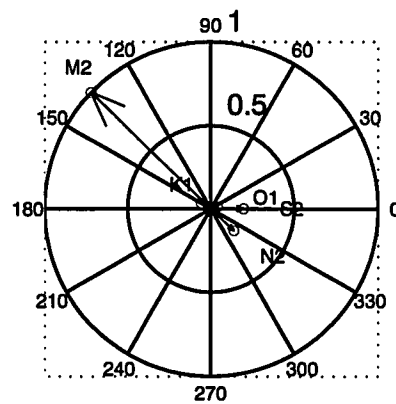


Fig. VI-C-3c. Hysteresis and depth-average *TKE* production at the station 'Y0.0'.



Ua/Us: Us=30.3



G/Gs: Gs=4.74E-3

Fig. VI-C-4a. Currents and estimates of PGA_r at the station 'RB'.

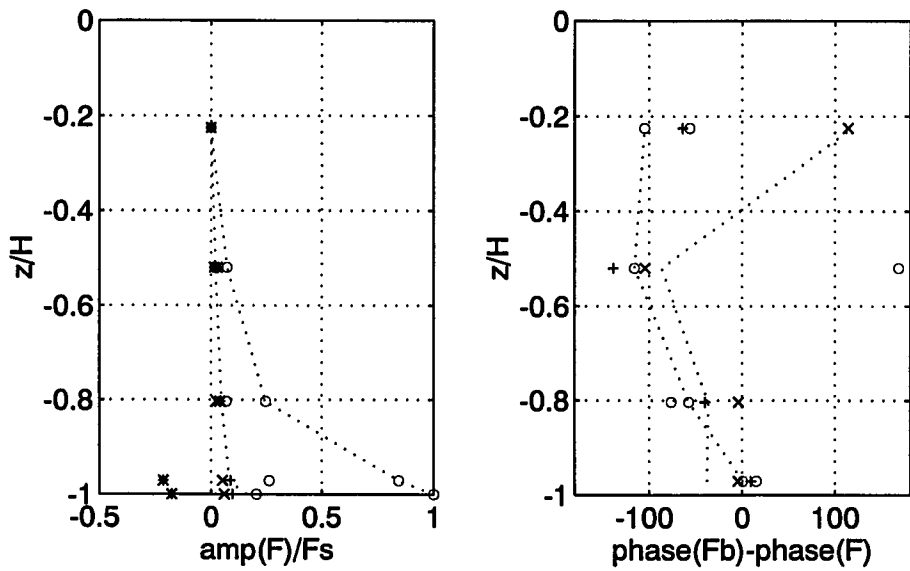
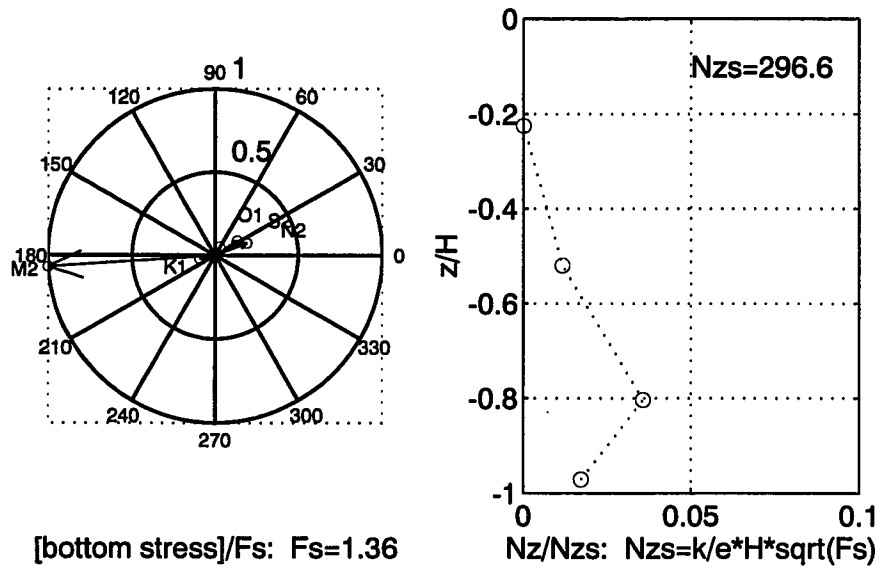


Fig. VI-C-4b. Eddy viscosity and shear stress at the station 'RB'.

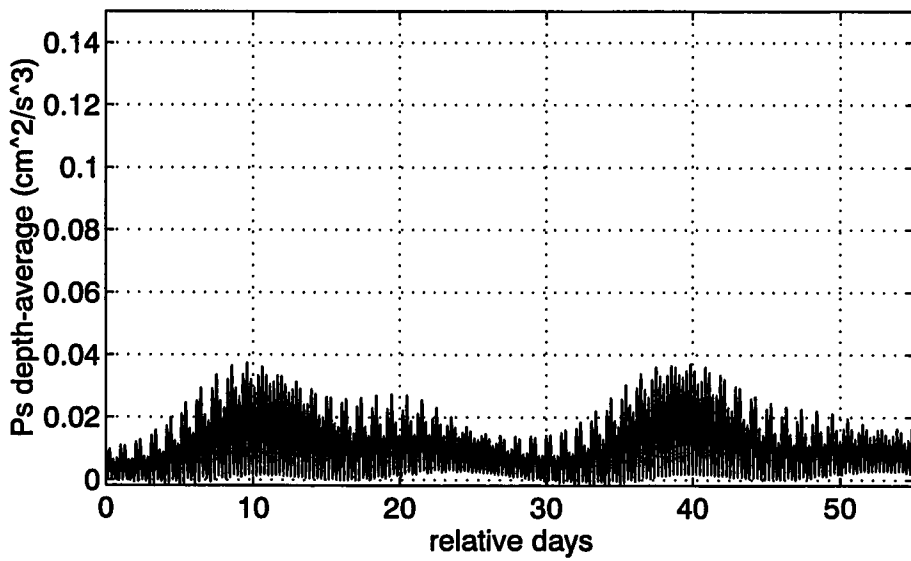
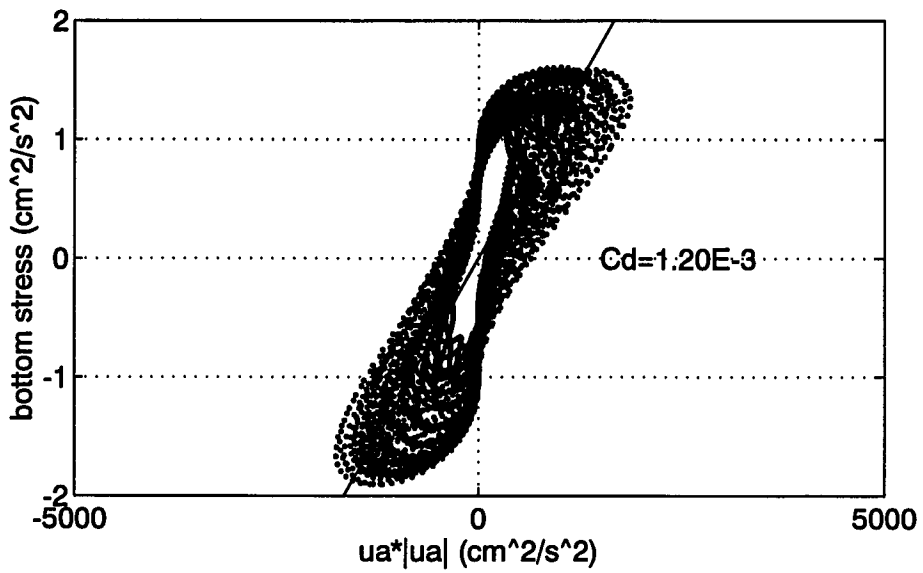
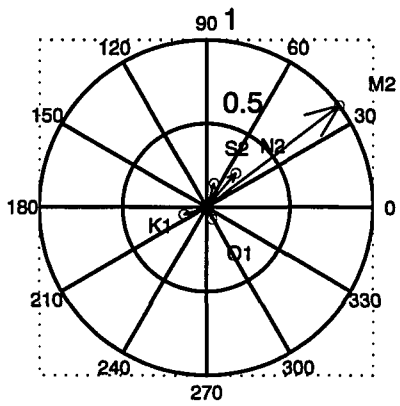
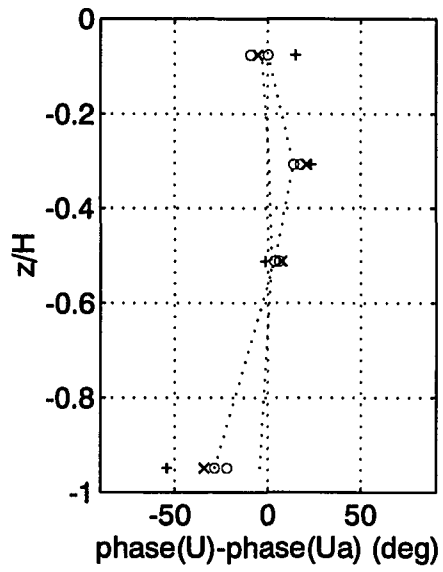
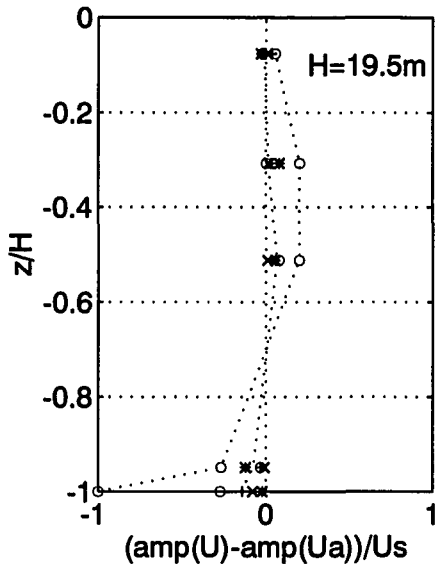
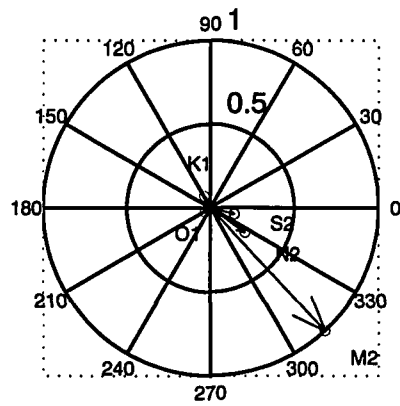


Fig. VI-C-4c. Hysteresis and depth-average *TKE* production at the station 'RB'.



Ua/Us: Us=30.8



G/Gs: Gs=4.72E-3

Fig. VI-C-5a. Currents and estimates of PGA_T at the station 'Tu91': segment 'a'.

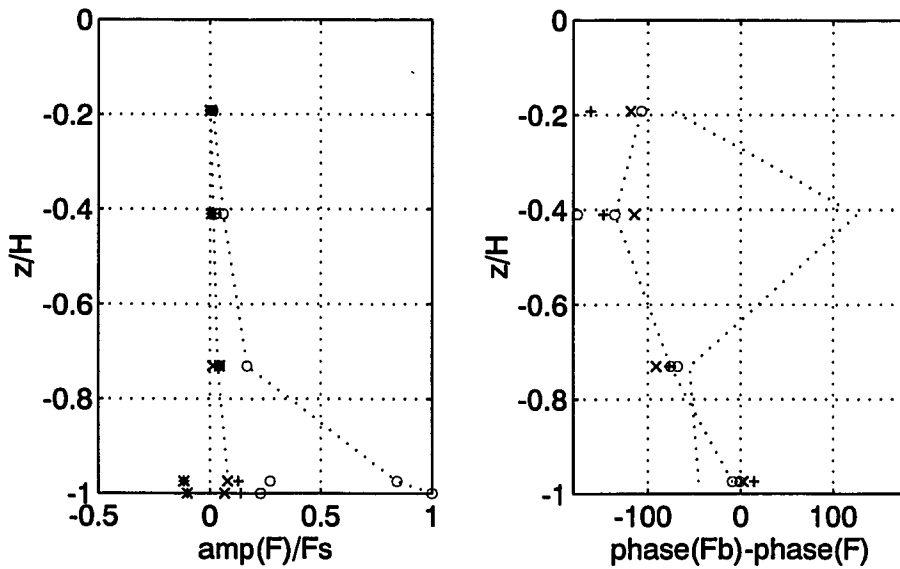
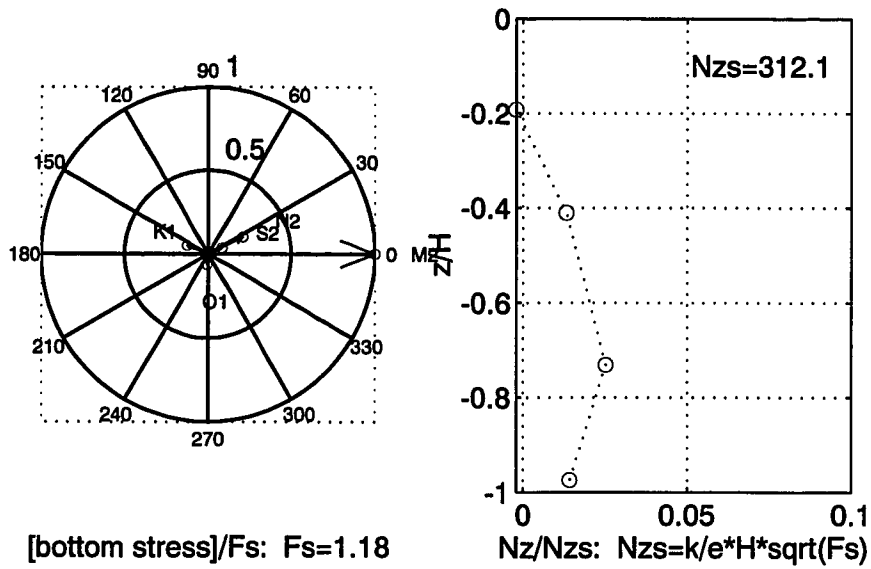


Fig. VI-C-5b. Eddy viscosity and shear stress at the station 'Tu91': segment 'a'.

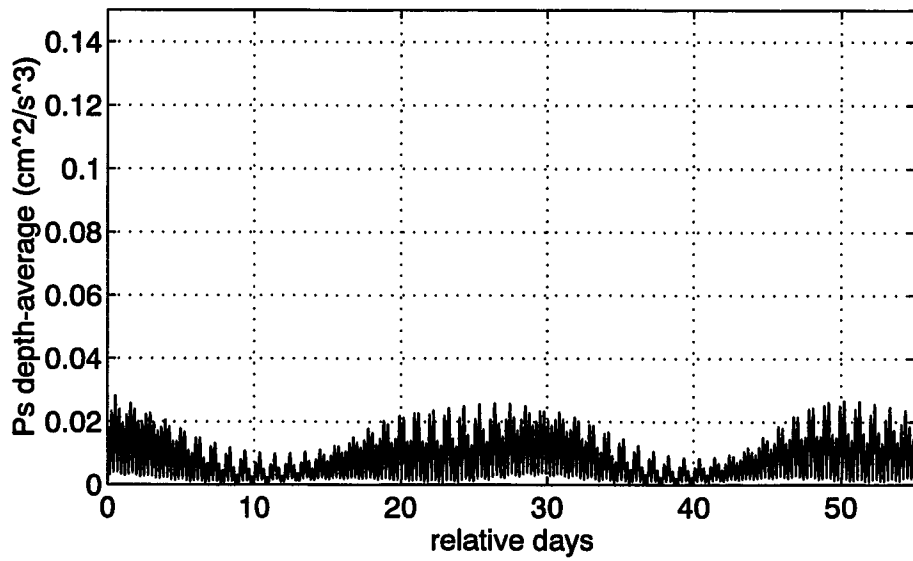
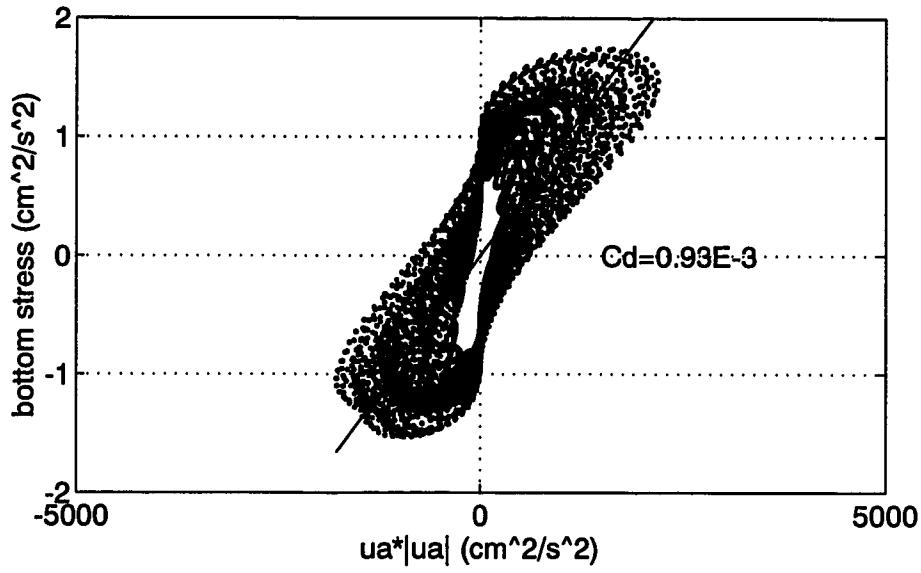


Fig. VI-C-5c. Hysteresis and depth-average *TKE* production at the station 'Tu91': segment 'a'.

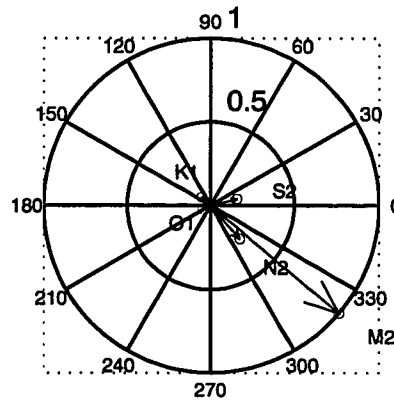
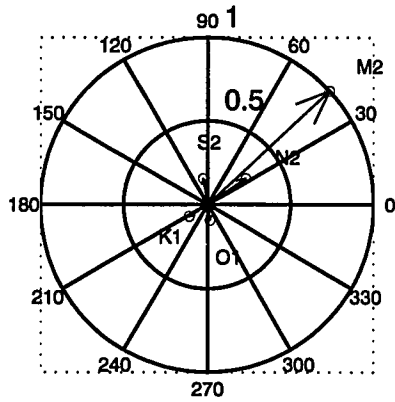
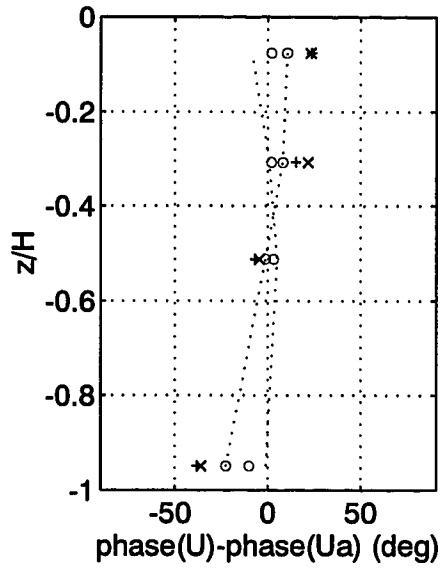
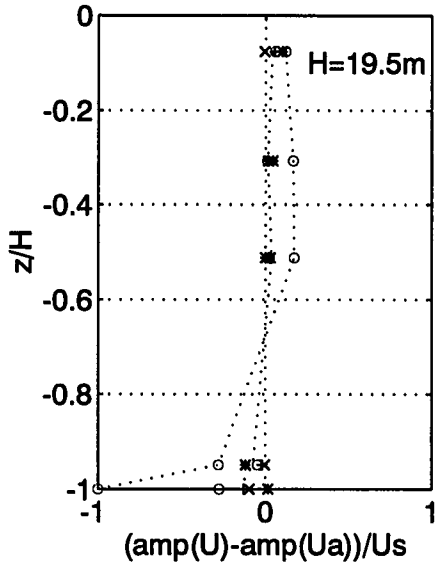
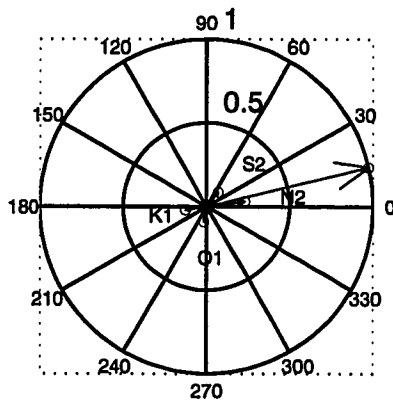


Fig. VI-C-6a. Currents and estimates of PGA_T at the station 'Tu91': segment 'b'.



[bottom stress]/Fs: Fs=1.33

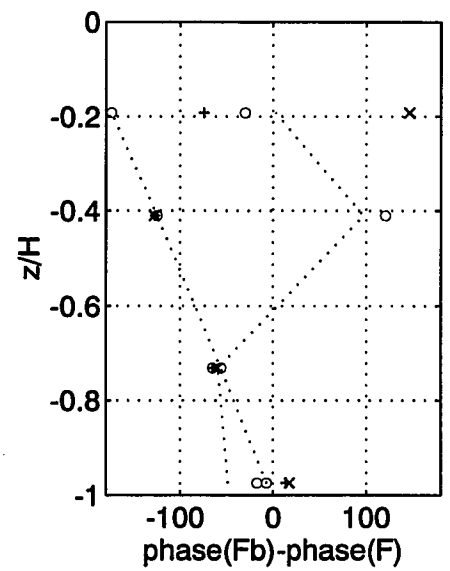
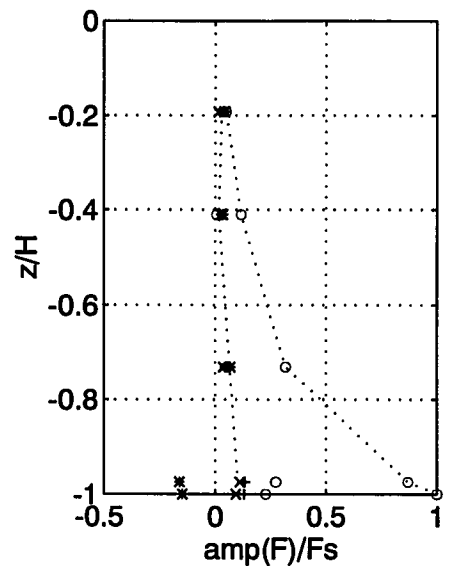
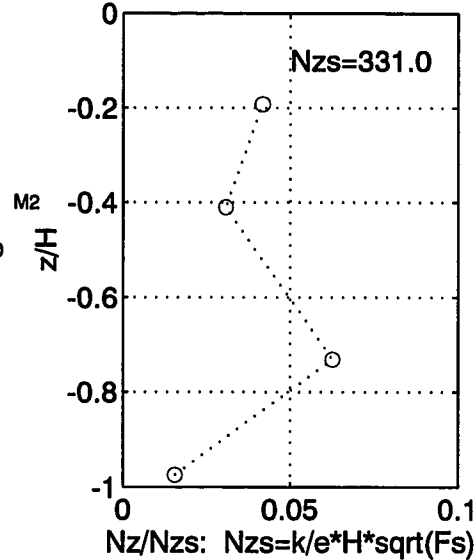


Fig. VI-C-6b. Eddy viscosity and shear stress at the station 'Tu91': segment 'b'.

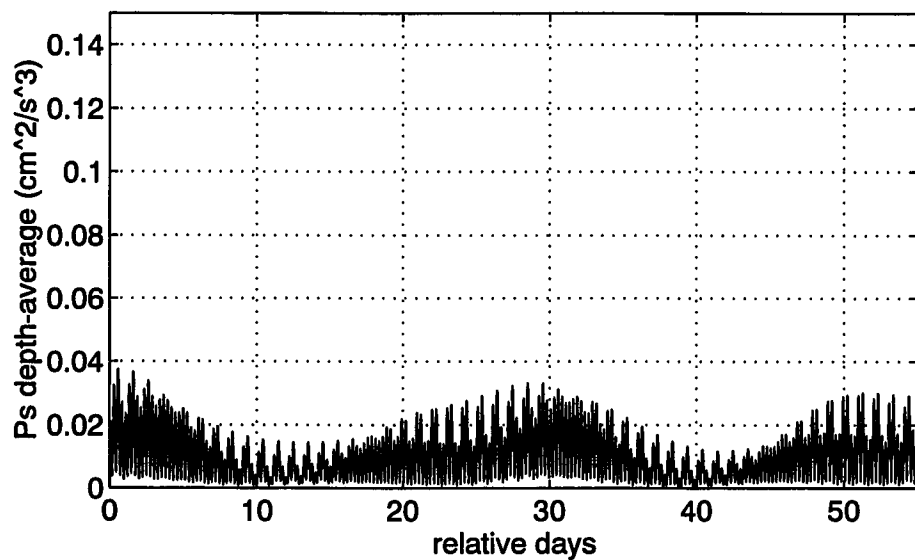
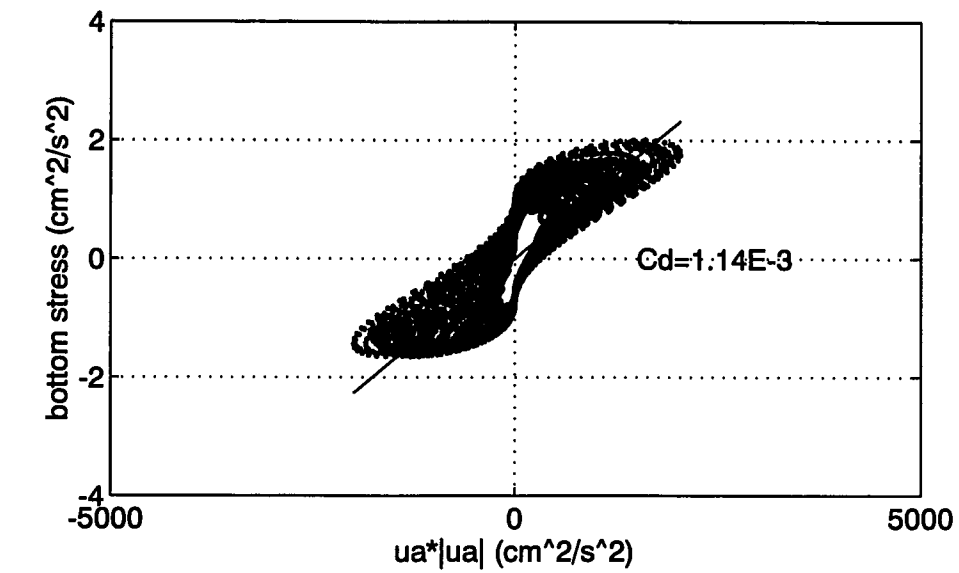


Fig. VI-C-6c. Hysteresis and depth-average *TKE* production at the station 'Tu91': segment 'b'.

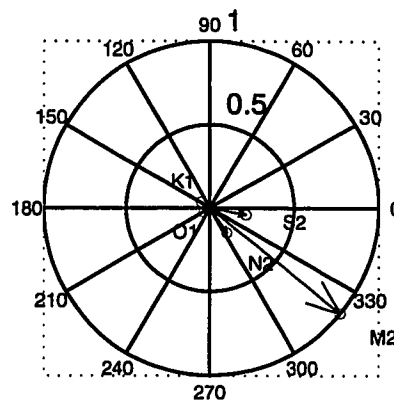
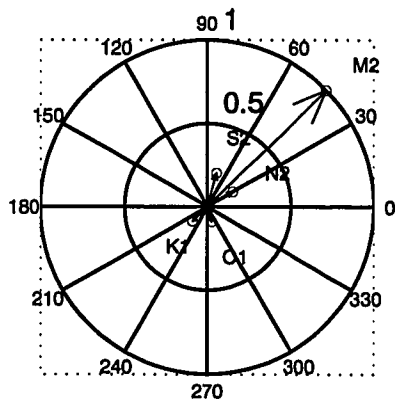
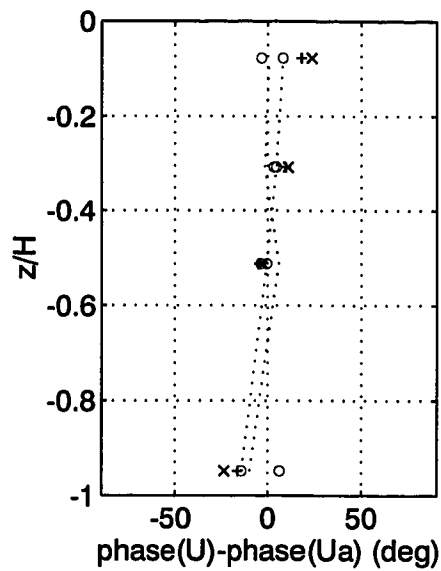
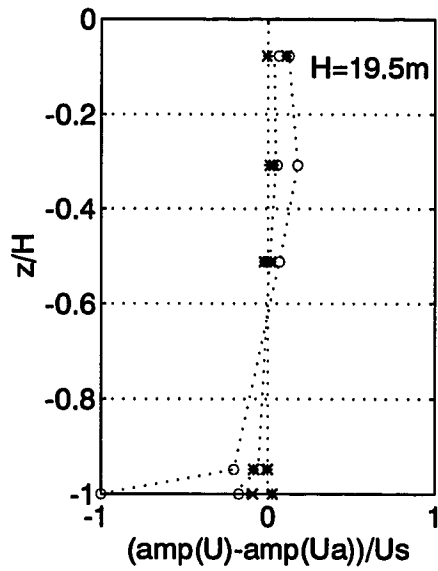
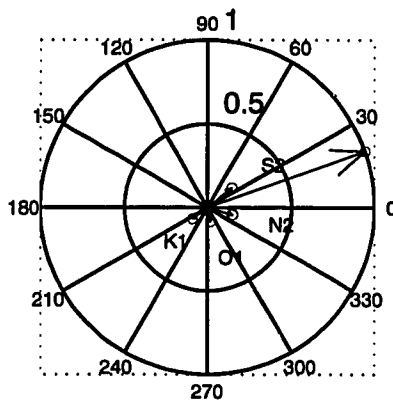


Fig. VI-C-7a. Currents and estimates of PGA_r at the station 'Tu91': segment 'c'.



[bottom stress]/Fs: Fs=1.06

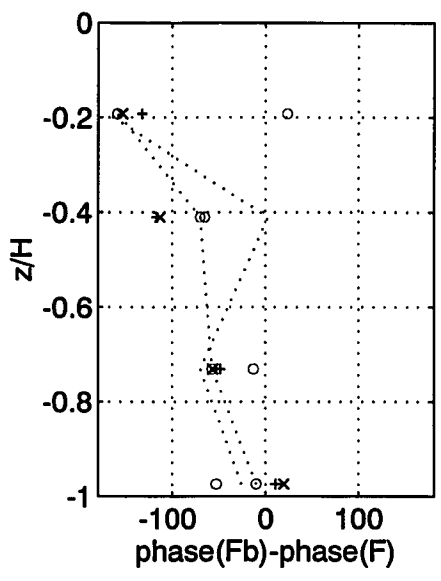
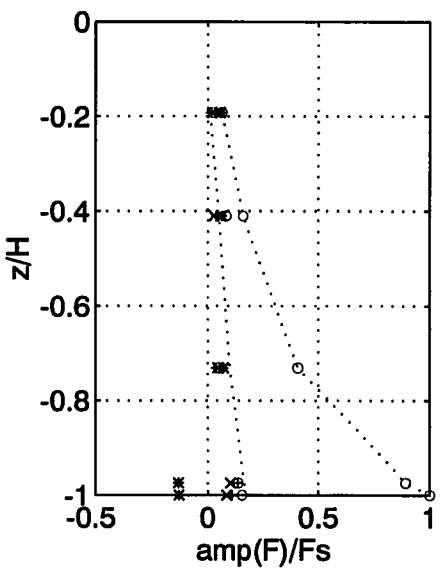
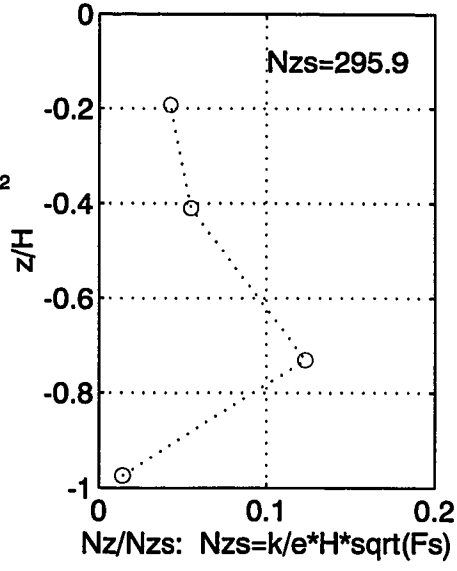


Fig. VI-C-7b. Eddy viscosity and shear stress at the station 'Tu91': segment 'c'.

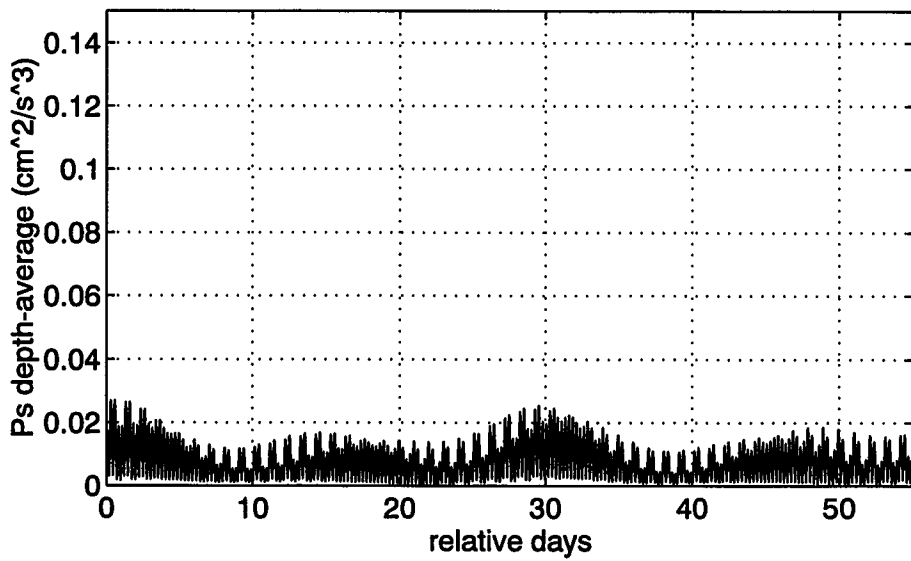
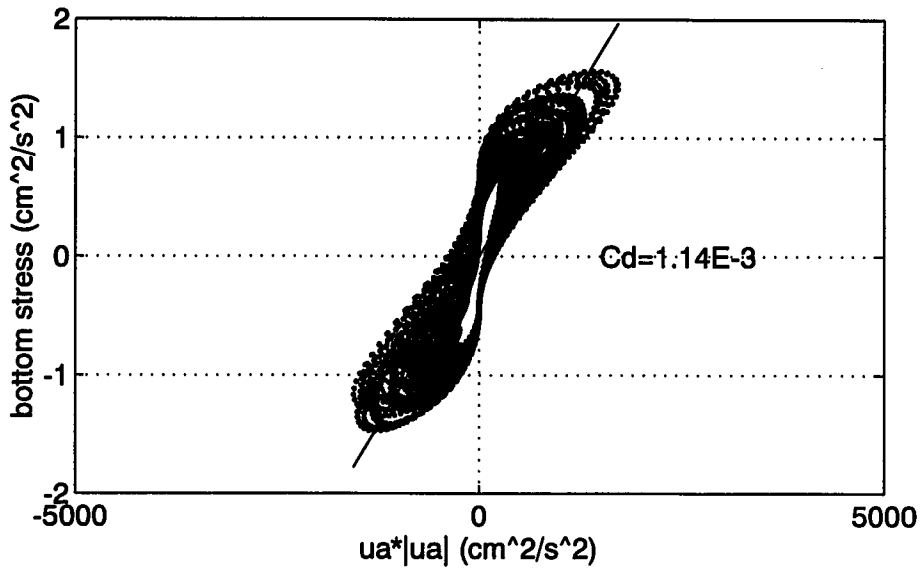


Fig. VI-C-7c. Hysteresis and depth-average *TKE* production at the station 'Tu91': segment 'c'.

3. Results in the bay mainstem

A total of 6 datasets were involved with the analysis-type I10: 'NOS066a', 'NOS066b', 'NOS121a', 'NOS121b', 'NOS121c' and 'NOS121d'. The first 2 sets represent the lower bay, while others represent the upper bay. Results are illustrated in 6 sets of figure plates: [Fig. VI-C-8a,b,c] for 'NOS066a', [Fig. VI-C-9a,b,c] for 'NOS066b', [Fig. VI-C-10a,b,c] for 'NOS121a', [Fig. VI-C-11a,b,c] for 'NOS121b', [Fig. VI-C-12a,b,c] for 'NOS121c' and [Fig. VI-C-13a,b,c] for 'NOS121d'.

Scaling factors (**Us**, **Gs**, **Fs**, **Nzs**) and C_d estimates are summarized in Table VI-22. In general, values at station 'NOS066' are ~2 times higher than at station 'NOS121'. At station 'NOS066', seasonal variation in **Nzs** and C_d estimates (~2% and 12% from the mean of 2 seasons) is relatively higher than in **Us** and **Gs** estimates (< 1%). Mid-summer estimates of **Nzs** and C_d are higher than mid-spring estimates.

At station 'NOS121', seasonal variation becomes more conspicuous. Relative deviations in **Nzs** and C_d are < 34% and < 120%, respectively, relatively higher than in **Us** and **Gs** (< 13%, < 12%) (Table VI-23). **Nzs** and C_d estimates are apparently the highest in mid/late fall (350.0; 1.61) and the lowest in mid/late spring (190.9; 0.22).

In general, the apparent maximum of scaled eddy

viscosity occurs at $0.7H - 0.8H$ below the surface. At station 'NOS066', the scaled maximum is significantly higher in mid-summer (1.91×10^{-1}) than in mid-spring (0.99×10^{-1}).

At station 'NOS121', the scaled maximum appears significantly higher in early winter (0.64×10^{-1}) and in mid/late fall (0.41×10^{-1}) than others (0.18×10^{-1} in mid/late spring, 0.13×10^{-1} in summer) (Table VI-24). At both stations, estimated amplitude profiles of internal-stress show upward-concave structure (Fig. VI-C-8b, 9b, 10b, 11b, 12b, 13b). There seems a conspicuous seasonal change in degree of the concavity at station 'NOS121'; more concave in mid/late-spring and summer than in mid/late fall and early winter (Fig. VI-C-10b, 11b, 12b, 13b).

Maximum values of bottom stress in time appear to be $\sim 3.7 \text{ cm}^2/\text{s}^2$ at station 'NOS066', and to be 1.0, 0.7, 0.8 and $1.9 \text{ cm}^2/\text{s}^2$ at station 'NOS121'. Generated time-series of depth-average *TKE* production show time-modulations (Fig. VI-C-8c, 9c, 10c, 11c, 12c, 13c). Apparently, apogean-perigean modulation is more conspicuous than spring-neap modulation. Perigean-spring-diurnal maxima appear to approach $\sim 0.08 \text{ cm}^2/\text{s}^3$ at station 'NOS066' (Fig. VI-C-8c, 9c), and to ~ 0.01 , ~ 0.004 , ~ 0.01 and $0.02 \text{ cm}^2/\text{s}^3$ at station 'NOS121' (Fig. VI-C-10c, 11c, 12c, 13c). It is noteworthy that the *TKE* shear production (tidal-wave dissipation) appears highest in early winter and lowest in mid/late-spring.

Estimates of 2 PGA_0 -coefficients (a and b) are given in Table VI-25. At station 'NOS066', estimates in mid-spring are ~factor 2 higher than in mid-summer. With mid-spring estimates, effective values of surface slope and λ_0 are deduced as -0.91×10^{-6} and $1.19 \times 10^{-9} \text{ cm}^{-1}$. With mid-summer estimates, effective values of surface slope and λ_0 are derived as -0.44×10^{-6} and $0.72 \times 10^{-9} \text{ cm}^{-1}$.

Meanwhile, at station 'NOS121', the estimates of PGA_0 -coefficients in two seasons, early winter and mid/late fall, are very similar, and 1 - 2 order higher than the other two (Table VI-25). In the former 2 seasons, estimates of surface slope and λ_0 are -0.12×10^{-6} and $0.15 \times 10^{-9} \text{ cm}^{-1}$. The sign reversal in the mid/late spring estimates may not bear any significance because of negligible magnitude.

Overall measures of numerical significance are given in Table VI-26. Compared to the model experiments, a two to three-order of magnitude increase is observed in misfit (γ). Measures of singularity (ν) are ~ 8 ($< \nu_c$), similar to those of the lower York stations.

Table VI-22. Scaling factors and drag coefficients at the bay stations. (G_s : 10^{-3} cm/s²; C_d : 10^{-3})

NOS	066a	066b	121a	121b	121c	121d
Us	41.6	41.1	20.5	21.1	24.2	19.9
Gs	6.47	6.41	3.06	3.08	3.58	3.11
Fs	2.20	2.43	0.55	0.30	0.48	1.00
Nzs	474.0	497.9	263.1	190.9	242.9	350.0
C_d	0.98	1.24	0.68	0.22	0.43	1.61

Table VI-23. Relative deviation ($|\Delta|$ %) in scaling factors and drag coefficients from seasonal means at the upper bay station, 'NOS121'. (unit: %)

NOS	121a	121b	121c	121d
Us	4.3	1.5	13.0	7.1
Gs	4.6	4.0	11.6	3.0
Fs	5.6	48.5	17.6	71.7
Nzs	0.5	27.1	7.2	33.7
C_d	7.5	70.0	41.5	119.0

Table VI-24. Scaled maximum of eddy viscosity and its vertical location at the bay stations. (N_{z0}/Nzs : 10^{-1})

NOS	066a	066b	121a	121b	121c	121d
N_{z0}/Nzs	0.99	1.91	0.64	0.18	0.13	0.41
z/H	-0.74	-0.72	-0.70		-0.69	

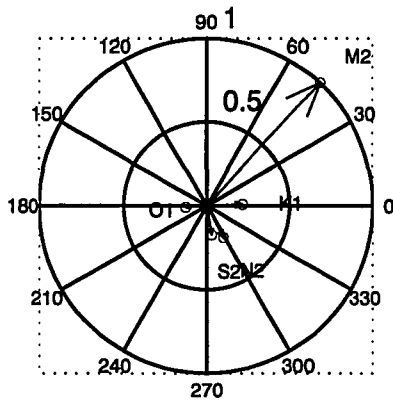
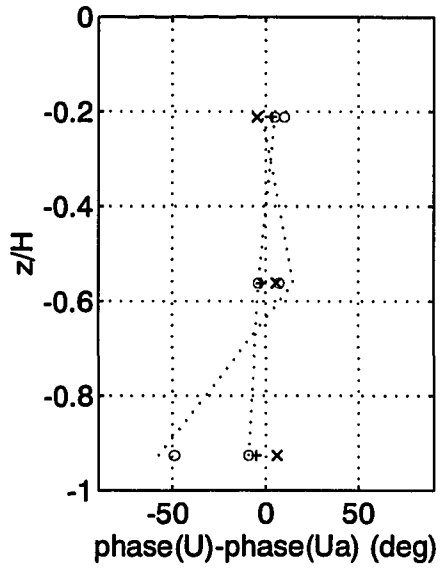
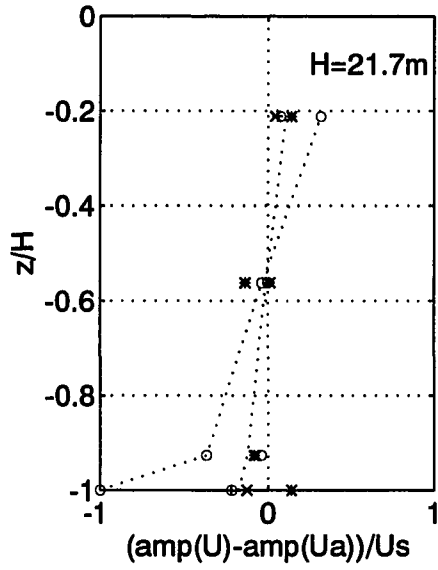
Table VI-25. Estimates of time-residual pressure gradient acceleration, PGA_0 , at the bay stations.
(a: 10^{-3} cm/s², b: 10^{-6} 1/s²)

NOS	066a	066b	121a	121b	121c	121d
a	0.89	0.43	0.13	-0.008	0.04	0.11
b	1.17	0.70	0.15	-0.005	0.05	0.15

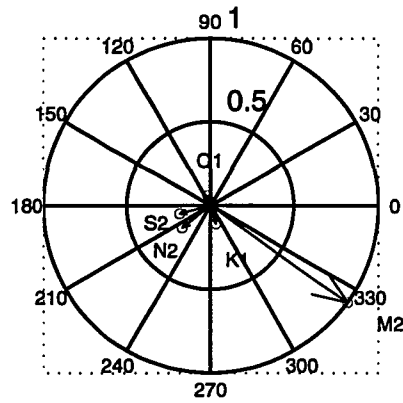
(a > 0: seaward, b > 0: landward)

Table VI-26. General measures of numerical confidence at the bay stations.

NOS	066a	066b	121a	121b	121c	121d
v	8.3	8.5	8.7	8.7	8.5	8.5
γ	4.6e-03	2.9e-03	7.4e-04	6.0e-04	6.3e-04	2.8e-03

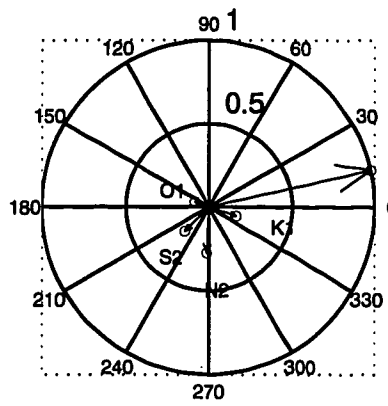


$U_a/U_s: U_s=41.6$



$G/G_s: G_s=6.47E-3$

Fig. VI-C-8a. Currents and estimates of PGA_r at the station 'NOS066': segment 'a'.



[bottom stress]/Fs: Fs=2.20

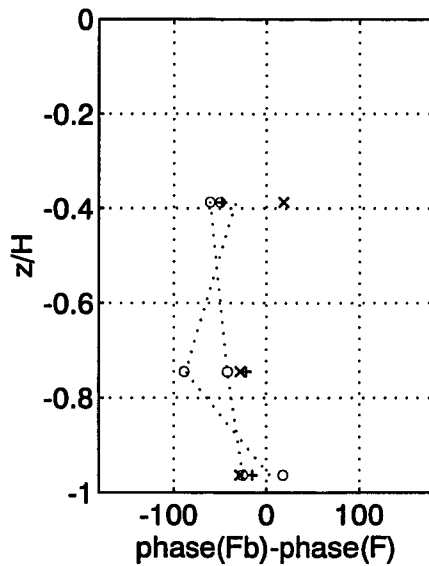
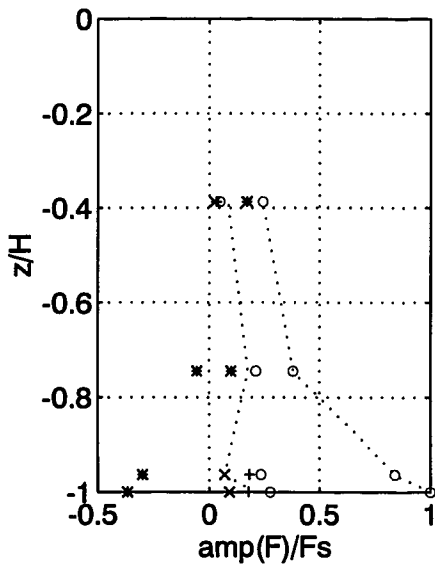
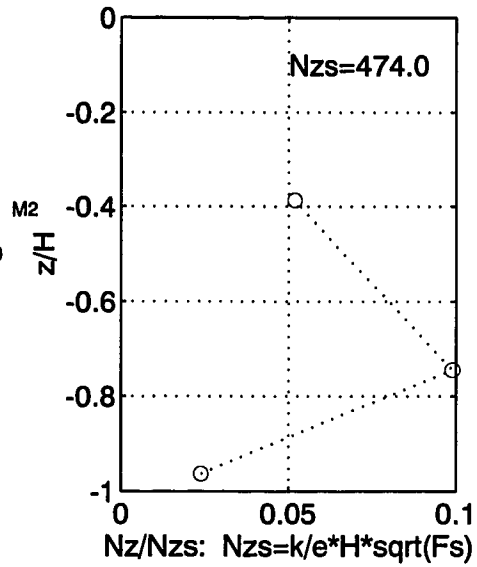


Fig. VI-C-8b. Eddy viscosity and shear stress at the station 'NOS066': segment 'a'.

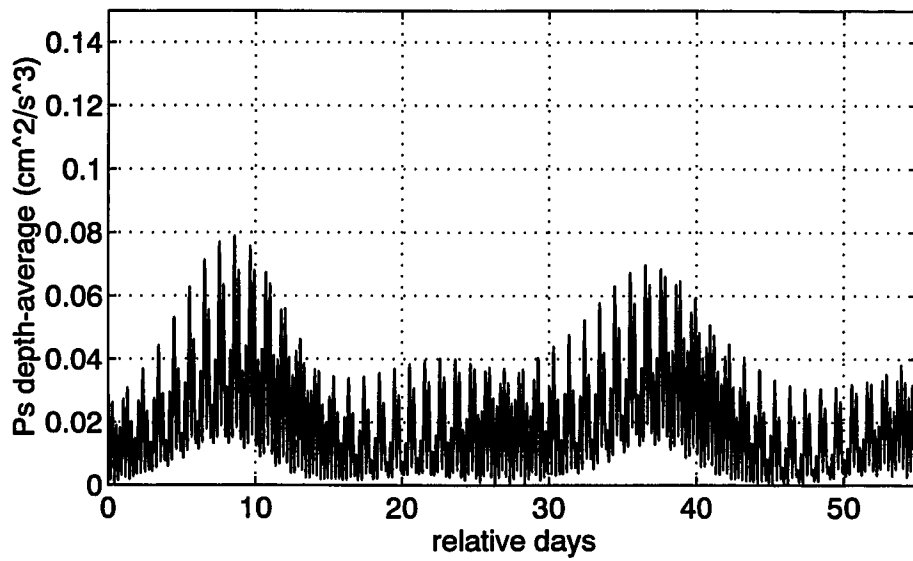
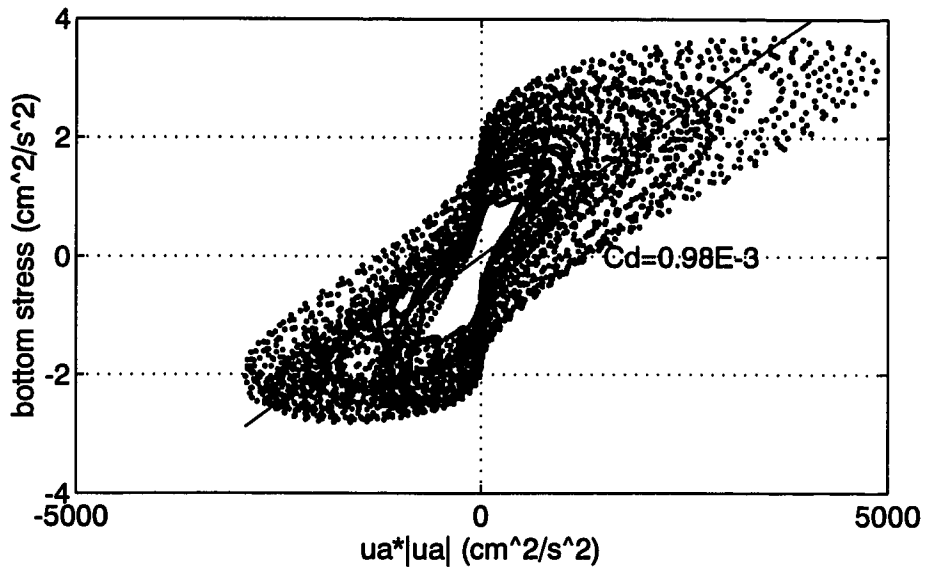
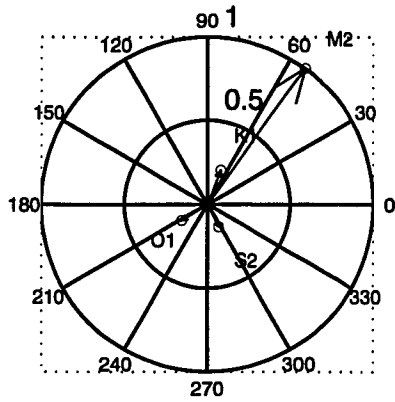
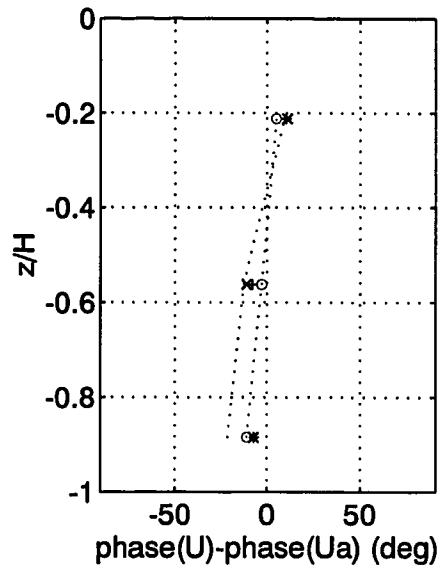
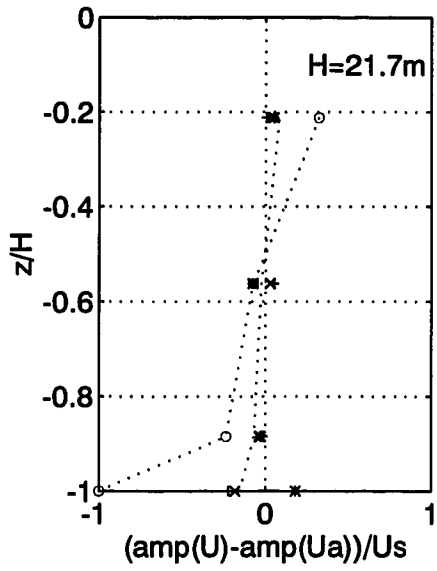
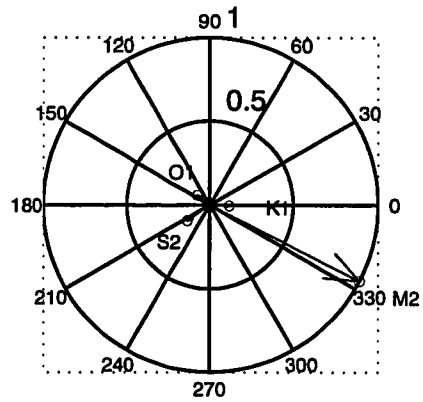


Fig. VI-C-8c. Hysteresis and depth-average *TKE* production at the station 'NOS066': segment 'a'.

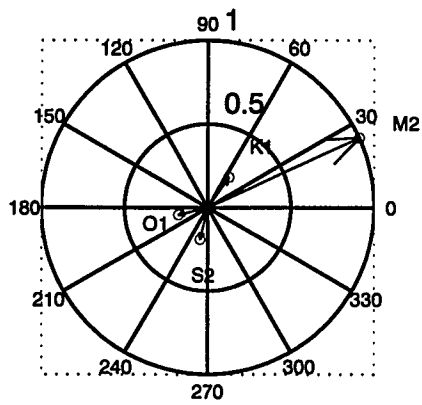


$U_a/U_s: U_s=41.1$



$G/G_s: G_s=6.41E-3$

Fig. VI-C-9a. Currents and estimates of PGA_T at the station 'NOS066': segment 'b'.



[bottom stress]/Fs: Fs=2.43

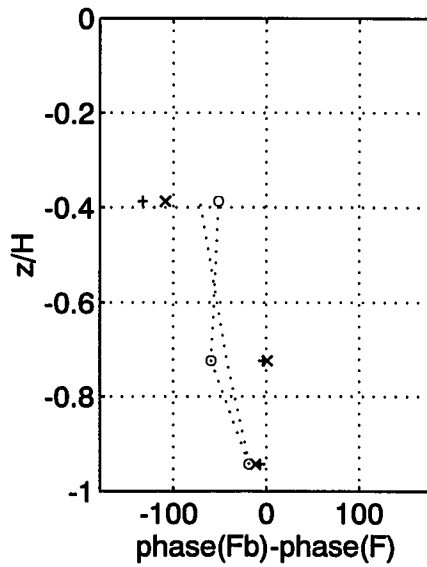
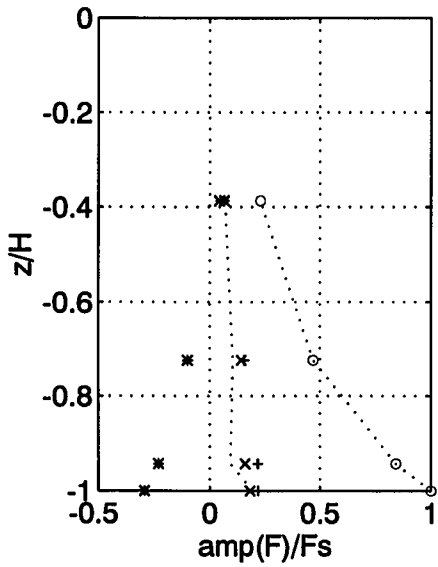
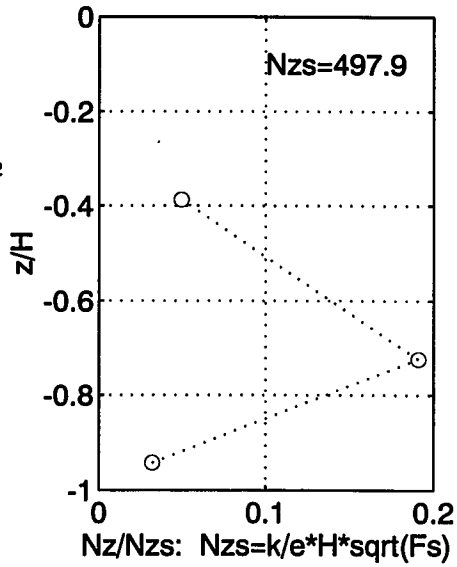


Fig. VI-C-9b. Eddy viscosity and shear stress at the station 'NOS066': segment 'b'.

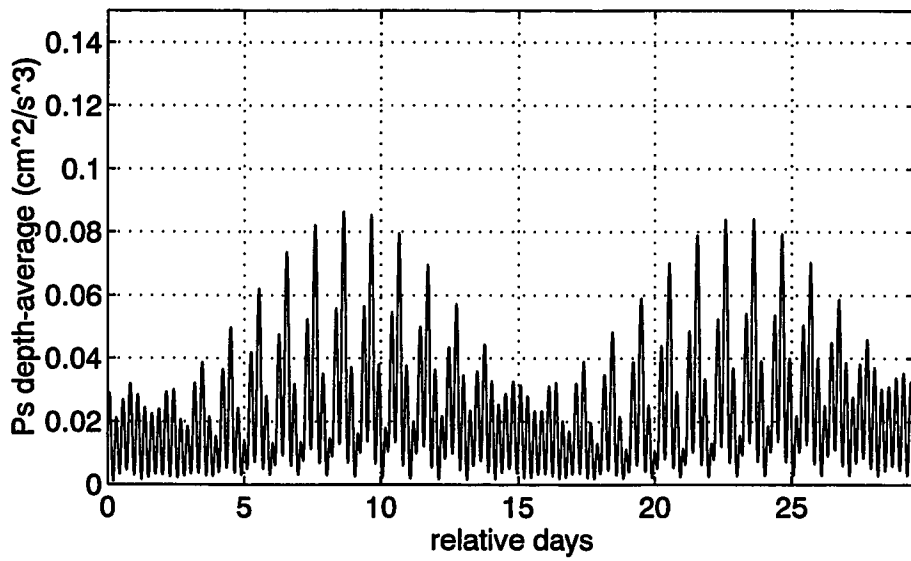
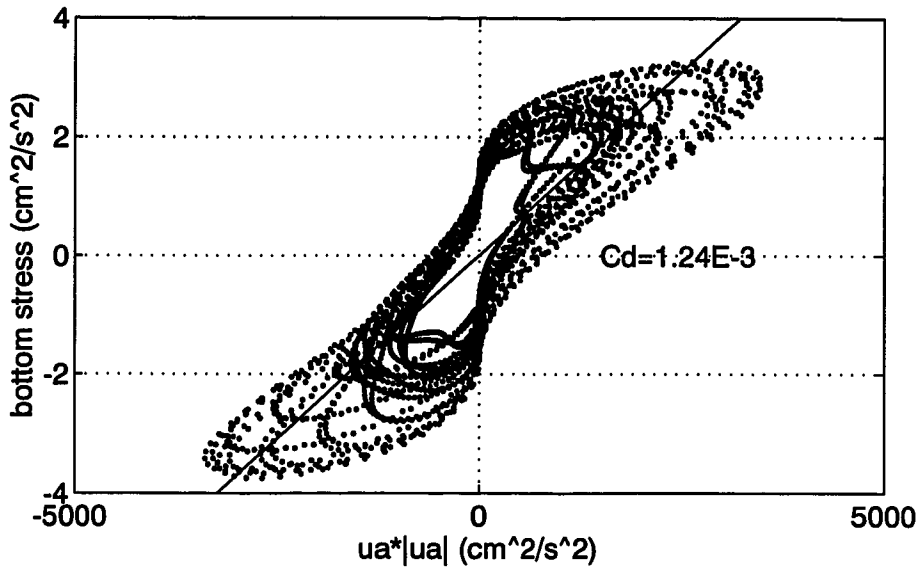


Fig. VI-C-9c. Hysteresis and depth-average *TKE* production at the station 'NOS066': segment 'b'.

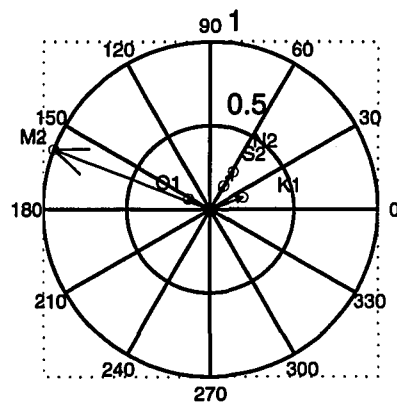
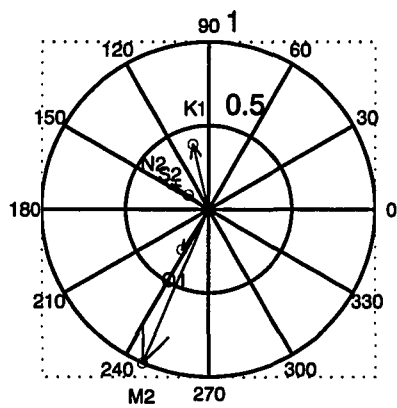
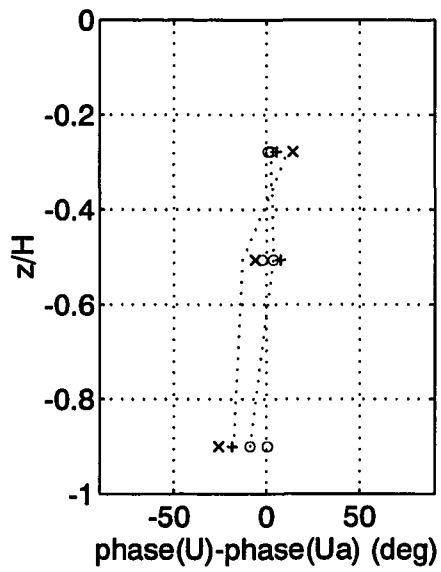
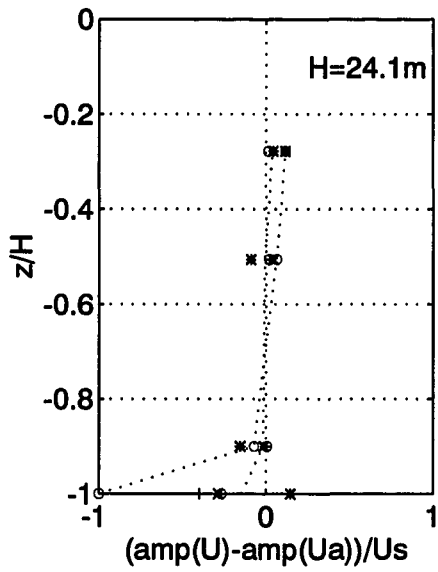
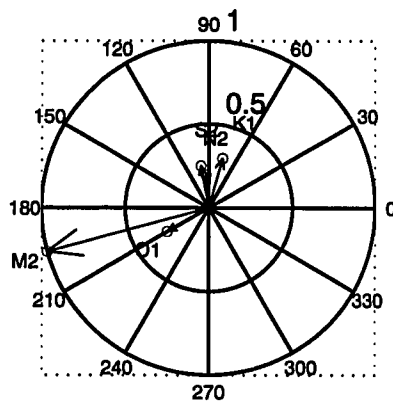


Fig. VI-C-10a. Currents and estimates of PGA_r at the station 'NOS121': segment 'a'.



[bottom stress]/Fs: Fs=0.55

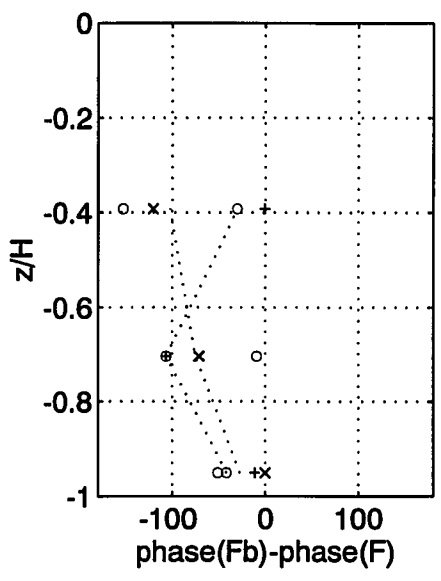
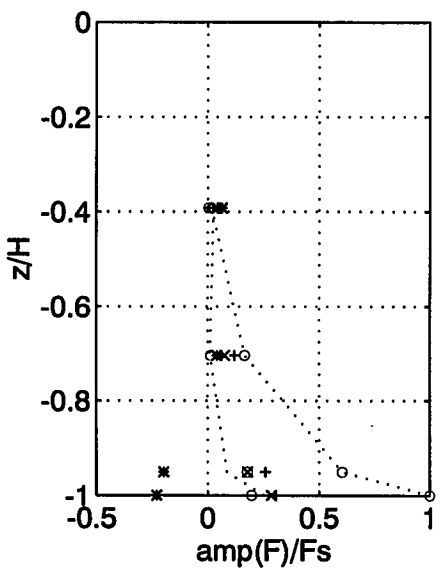
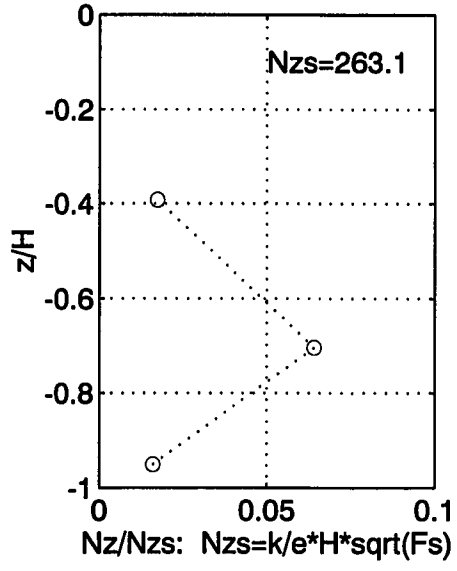


Fig. VI-C-10b. Eddy viscosity and shear stress at the station 'NOS121': segment 'a'.

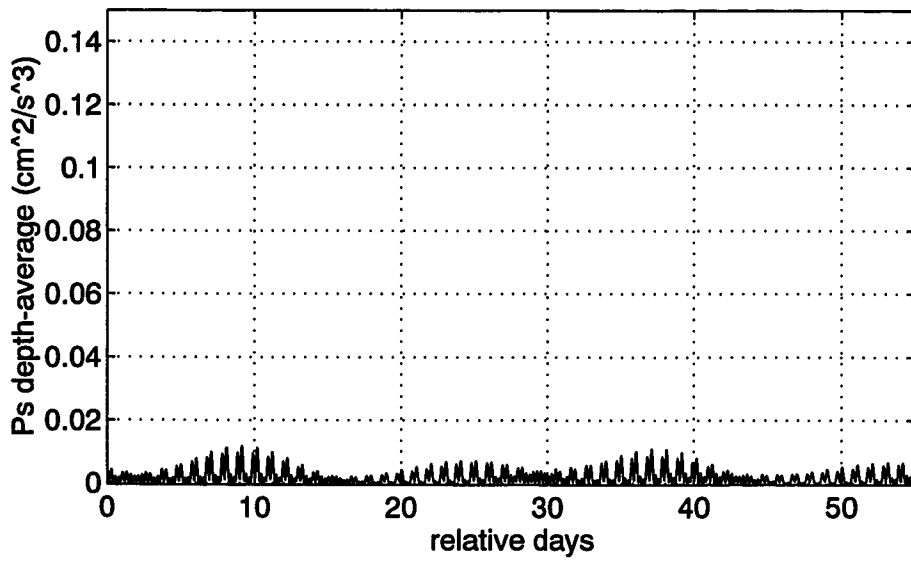
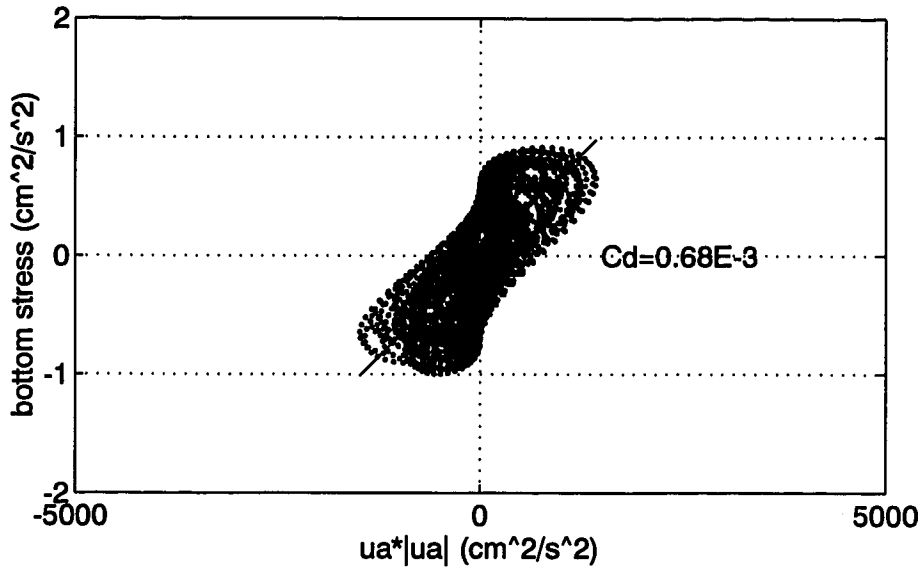


Fig. VI-C-10c. Hysteresis and depth-average *TKE* production at the station 'NOS121': segment 'a'.

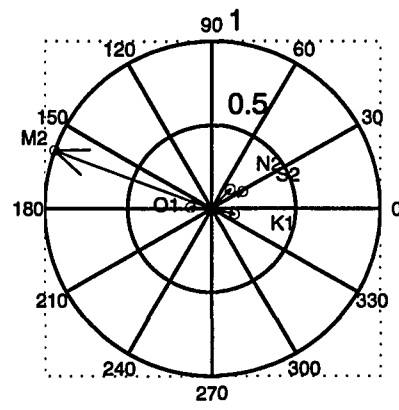
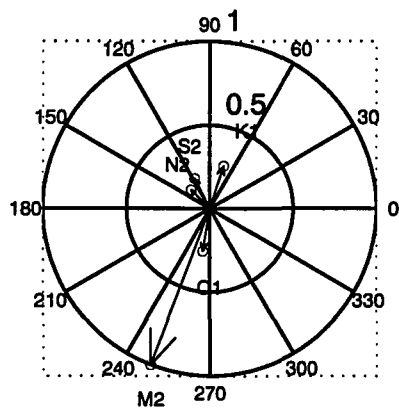
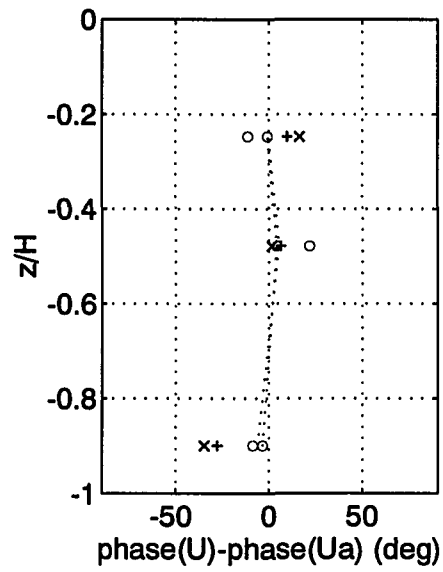
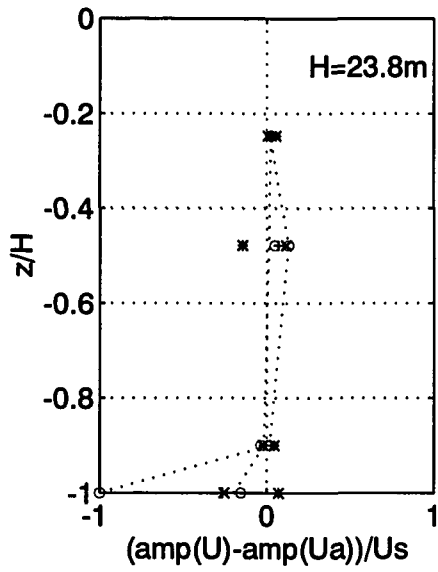
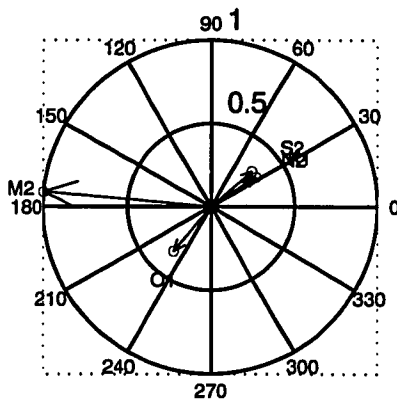


Fig. VI-C-11a. Currents and estimates of PGA_T at the station 'NOS121': segment 'b'.



[bottom stress]/Fs: Fs=0.30

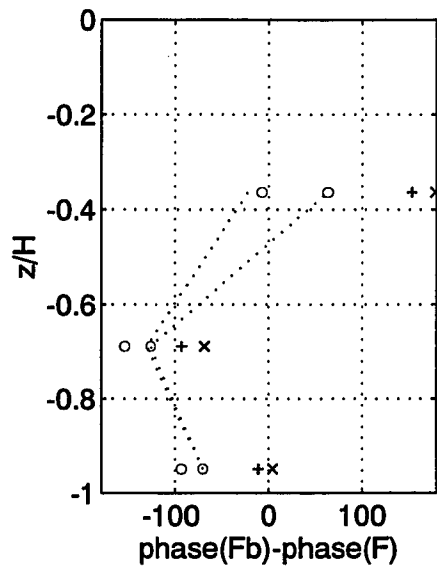
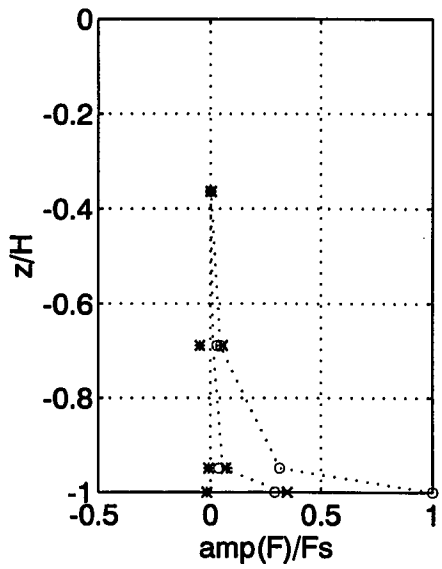
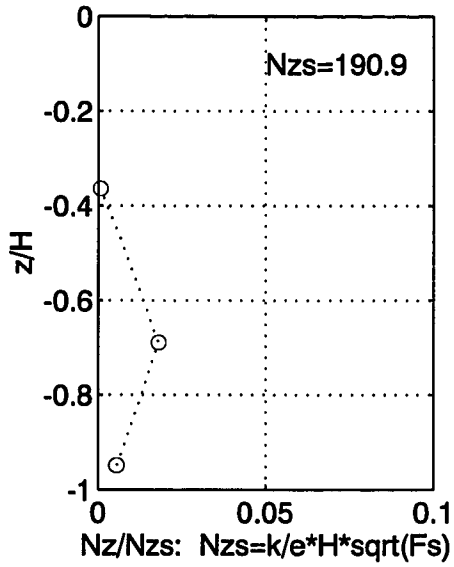


Fig. VI-C-11b. Eddy viscosity and shear stress at the station 'NOS121': segment 'b'.

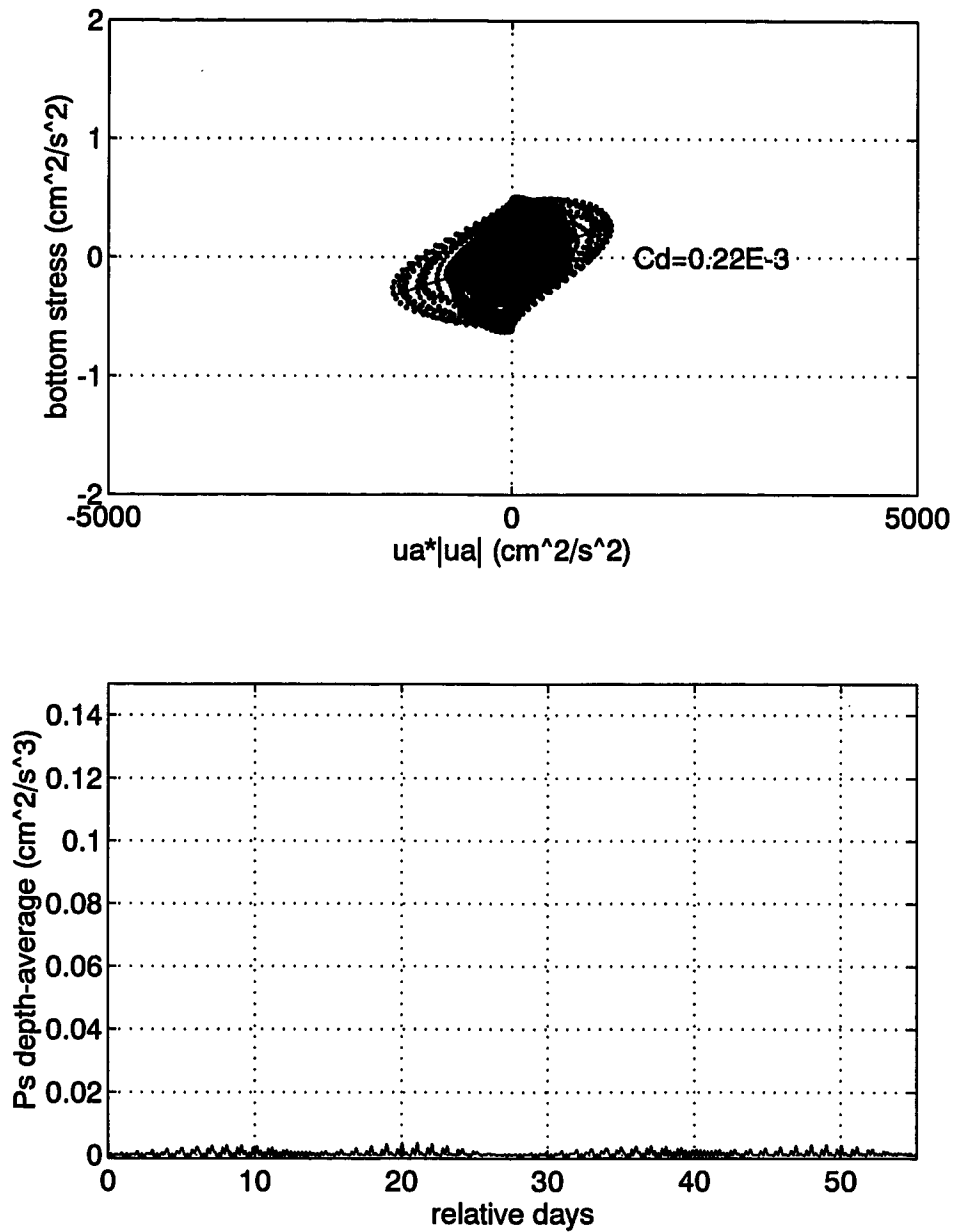


Fig. VI-C-11c. Hysteresis and depth-average *TKE* production at the station 'NOS121': segment 'b'.

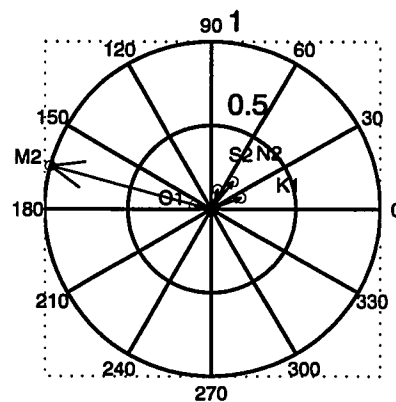
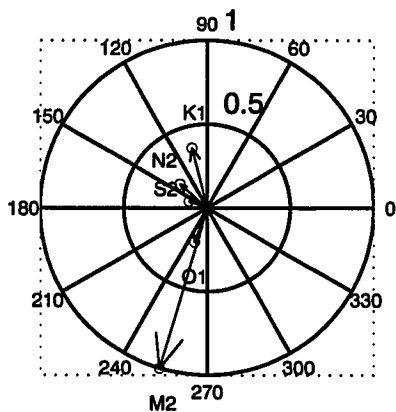
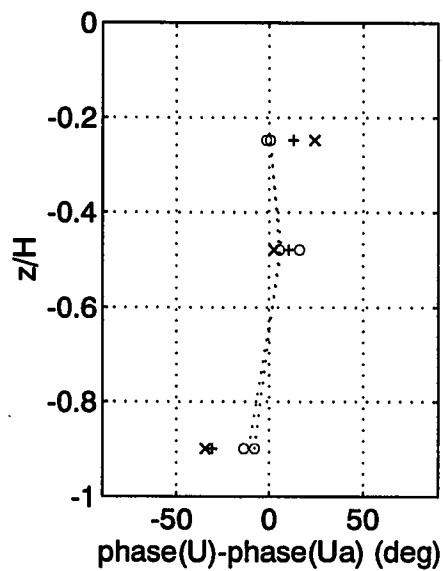
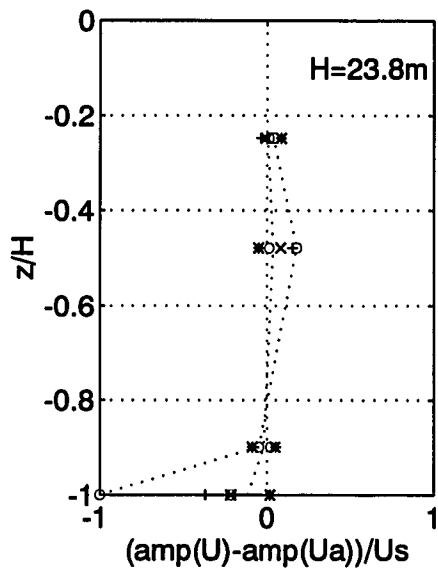
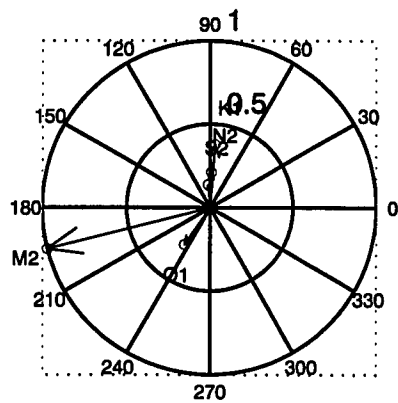


Fig. VI-C-12a. Currents and estimates of PGA_T at the station 'NOS121': segment 'c'.



[bottom stress]/Fs: Fs=0.48

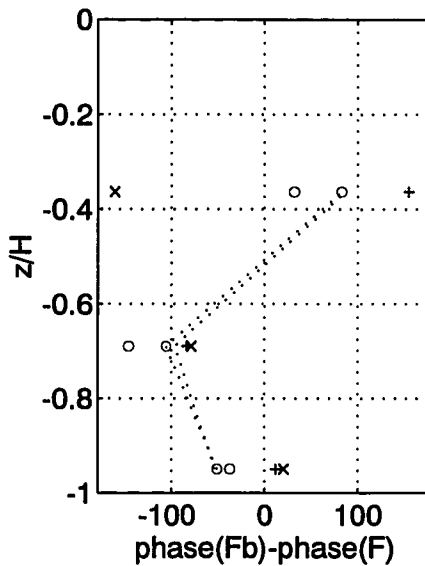
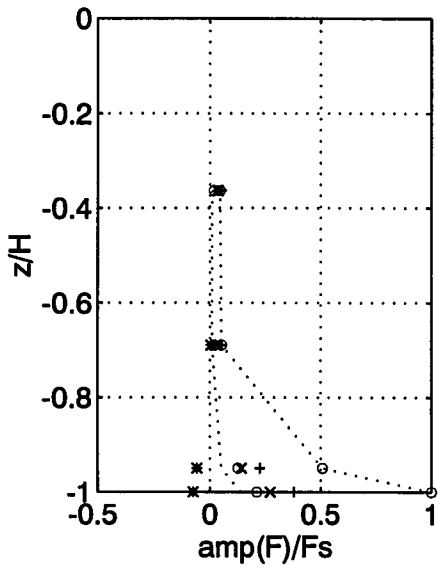
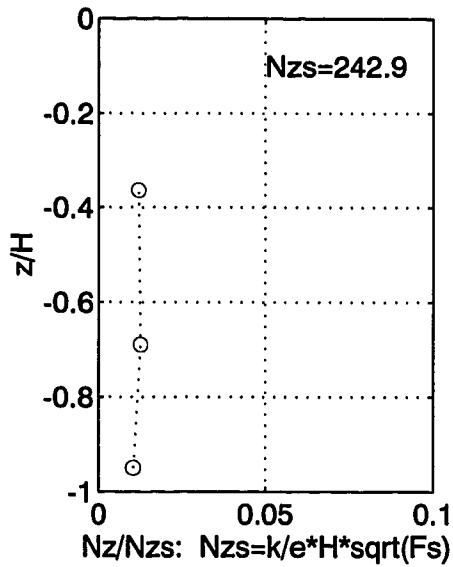


Fig. VI-C-12b. Eddy viscosity and shear stress at the station 'NOS121': segment 'c'.

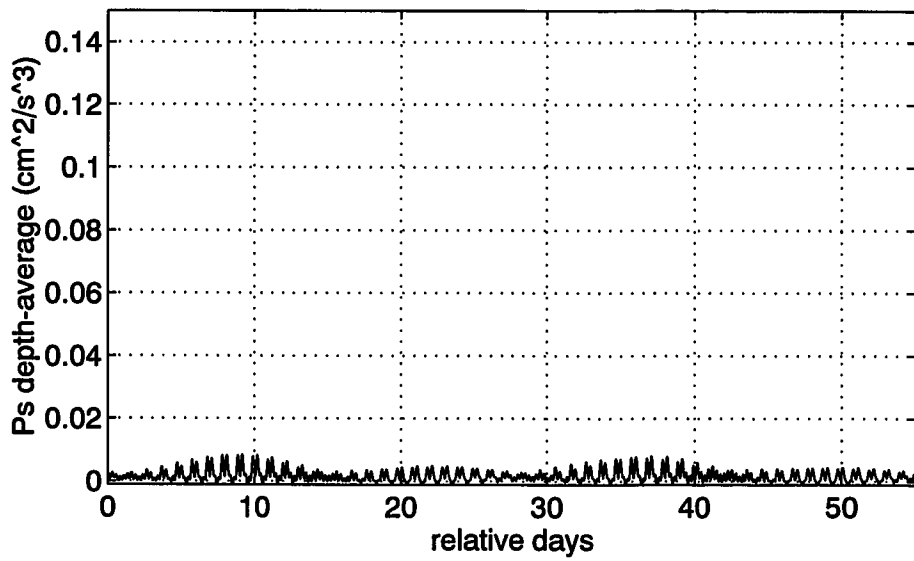
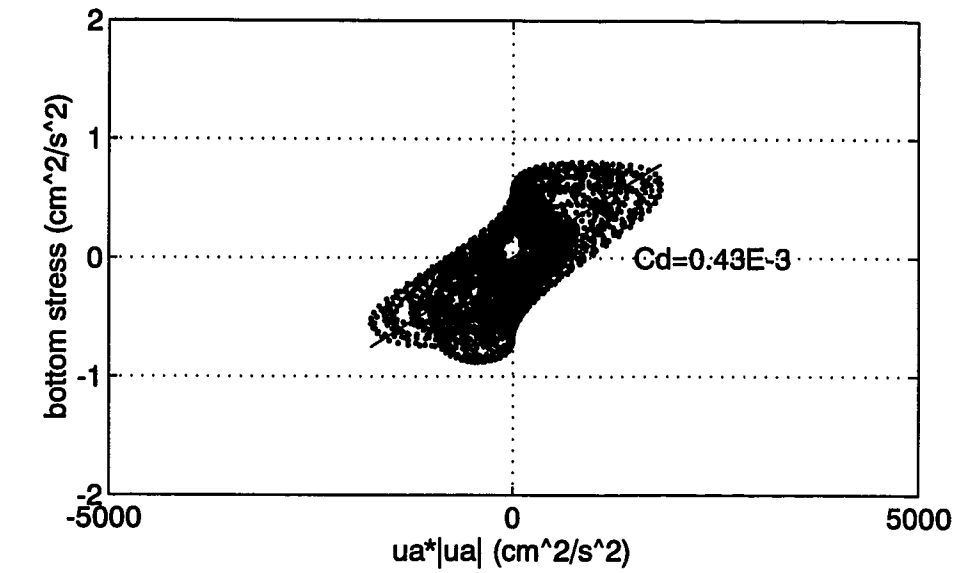
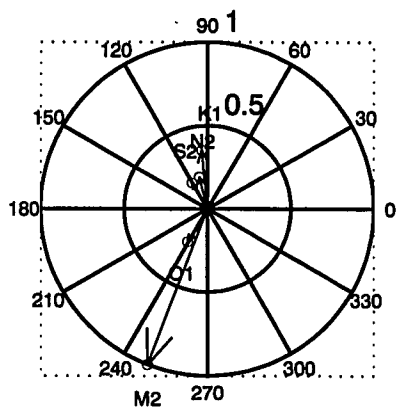
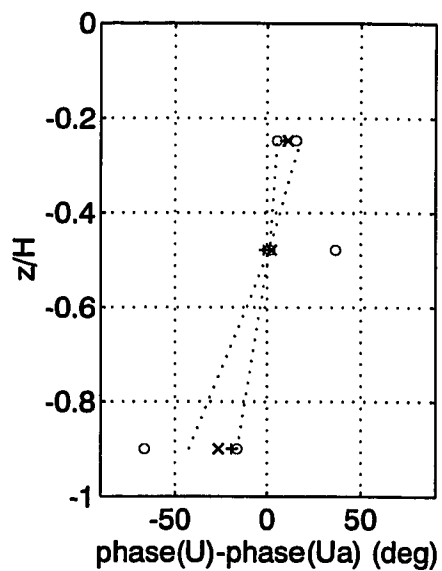
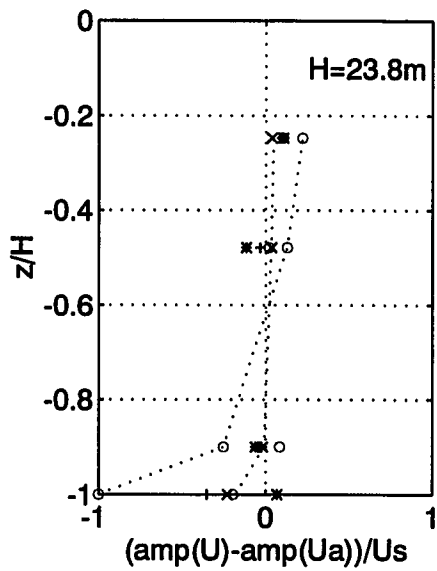
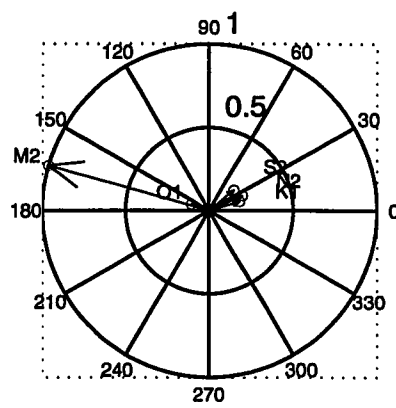


Fig. VI-C-12c. Hysteresis and depth-average *TKE* production at the station 'NOS121': segment 'c'.



$Ua/Us: Us=19.9$



$G/Gs: Gs=3.11E-3$

Fig. VI-C-13a. Currents and estimates of PGA_r at the station 'NOS121': segment 'd'.

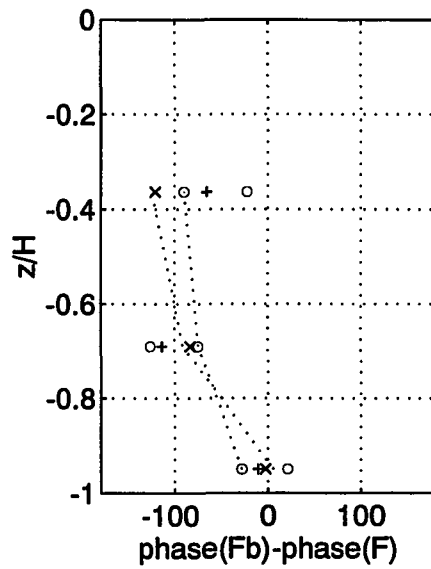
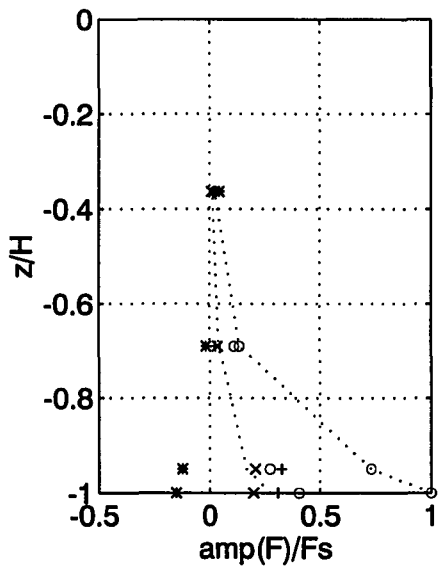
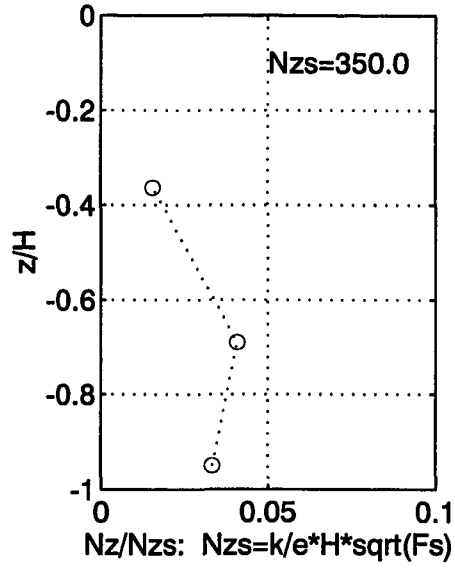
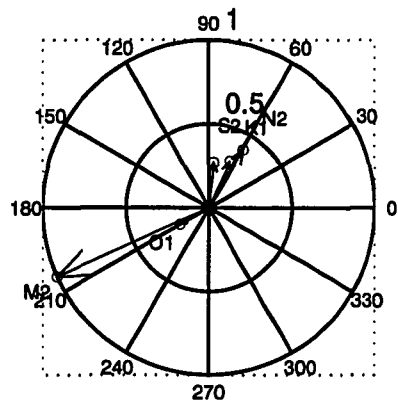


Fig. VI-C-13b. Eddy viscosity and shear stress at the station 'NOS121': segment 'd'.

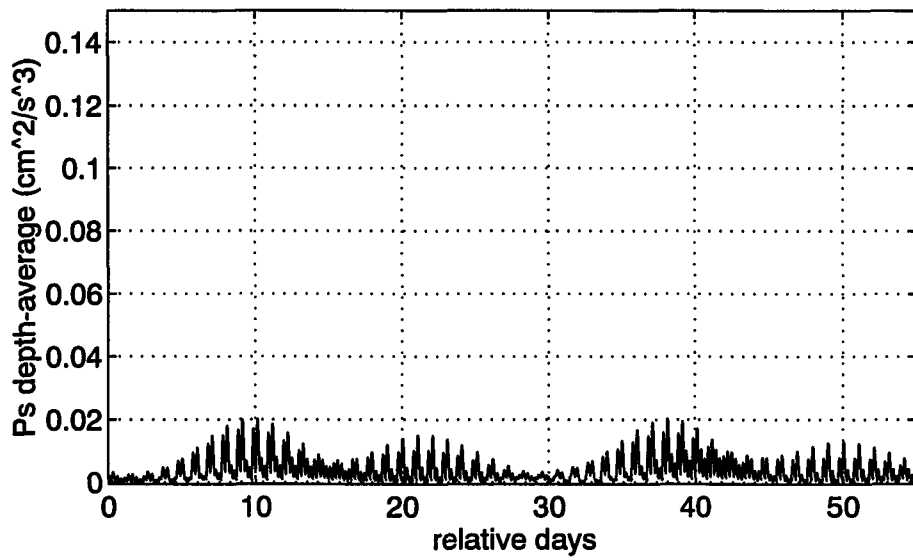
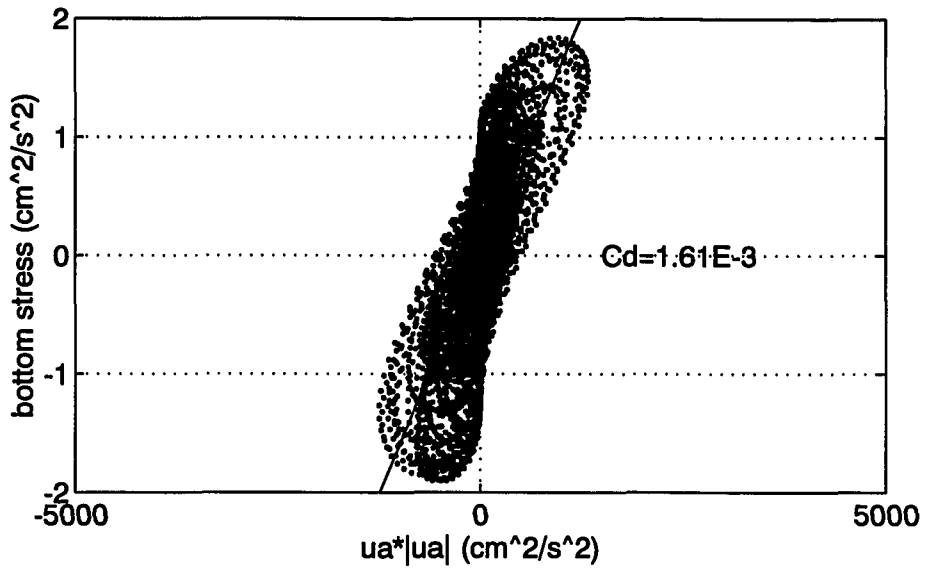


Fig. VI-C-13c. Hysteresis and depth-average *TKE* production at the station 'NOS121': segment 'd'.

D. Results with ADCP Data

1. Current profiles

The time-residual, 5 principal harmonics (M_2 , S_2 , K_1 , N_2 , O_1) and one induced harmonic (M_6) were determined from time series of bins by the method of *LSHA*. It is seen that amplitude and phase profiles have noisy structure in the vertical, with its cause unclear (Fig. VI-D-1a). The structure, however, seems ordered with small vertical waves. Profiles were smoothed to remove those wavelets. Smoothing schemes were 4-, 8-, 12-point moving averages in the vertical. An average of 2 points nearest to the bottom was always kept for near-bottom information. It is conceptually obvious that the averaging schemes are to remove the wavelets with wave numbers larger than $2\pi/4$, $2\pi/8$ and $2\pi/12$ m^{-1} . It is clearly seen that the noisy profiles are gradually smoothed in both amplitude and phase (Fig. VI-D-2a, 3a, 4a). It is noted that vertical macro-structure is still preserved even with the 12-point averaging.

2. Results without N_{2M} resolution

Results with the approach I10 are illustrated in 9 figure plates (Fig. VI-D-1a, 2a, 3a, 4a, 1b, 2b, 3b, 4b, 4c). Estimates of PGA_T vary little with the averaging points increased: $\leq \sim 2\%$ for amplitude, $< \sim 3^\circ$ for phase

(Table VI-27), indicating that PGA_T estimates are little influenced by estimates of frictional term (orthogonality).

As the averaging points increase, N_{z0} structure changes significantly, then becomes stabilized and physically reasonable towards positive viscosity (Fig. VI-D-1b, 2b, 3b, 4b), while PGA_T estimates vary little. Therefore, results due to the 12-point averaging are used in subsequent discussion.

Eddy-viscosity scale Nzs is $318.3 \text{ cm}^2/\text{s}$ and the drag-coefficient C_d is 0.45. Maximum of scaled eddy viscosity is 0.99×10^{-1} , occurring near $0.82H$ below the surface (Fig. VI-D-4b). It is obvious that amplitude profiles of internal stress is upward-concave (Fig. VI-D-4b).

Maximum bottom stress in time appears to be $\sim 1.0 \text{ cm}^2/\text{s}^2$. At this time of year, a time series of depth-average TKE production shows conspicuous apogean-perigean modulation as well as spring-neap modulation. The overall magnitude of the series, however, is comparatively small, with perigean-spring-diurnal maximum being $\sim 0.01 \text{ cm}^2/\text{s}^3$ (Fig. VI-D-4c).

Estimates of 2 PGA_0 -coefficients (a and b) are given as 0.06×10^{-3} and 0.07×10^{-6} . Corresponding values of effective surface slope and λ_0 are -0.06×10^{-6} and $0.07 \times 10^{-9} \text{ cm}^{-1}$.

Measures of singularity (ν) and misfit (γ) are 9.2 and 1.4×10^{-4} , respectively. Regarding values in the upper York,

ν is increased by ~ 2 , and γ is reduced by an order of magnitude. The feature implies that the matrix system is more singular, but more fit to the basis equation.

3. Results with N_{2M4} resolution

PGA_T estimates are not significantly different from those with the I10 approach, with relative deviation being $\leq 1.1\%$ for amplitude and $\leq 0.3^\circ$ for phase (Table VI-28). This feature, again, indicates that PGA_T term tends to be orthogonally estimated.

However, the N_{z0} profile has many negative values. In addition, overall N_{z0} estimates are much smaller than amplitudes of the time-varying component, N_{2M4} (Fig. VI-D-5b; 'o': N_{z0} , '*': N_{2M4}). The outcome is physically unreasonable. In short, the analysis failed to deduce the M_4 component of eddy viscosity. Measures of singularity (ν) and misfit (γ) are 9.8 and 6.3×10^{-4} , respectively, which are increased values compared to the I10 analysis.

Table VI-27. Inversions on ADCP data without N_{2M4} resolution: PGA_T estimates. A: (10^{-3} cm/s²)

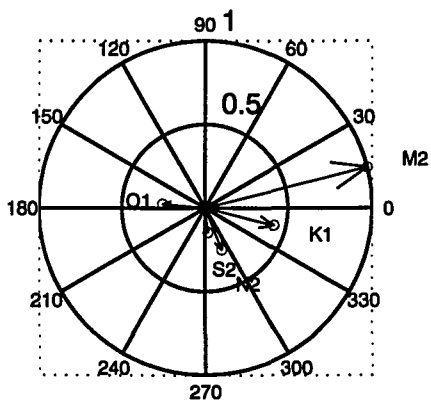
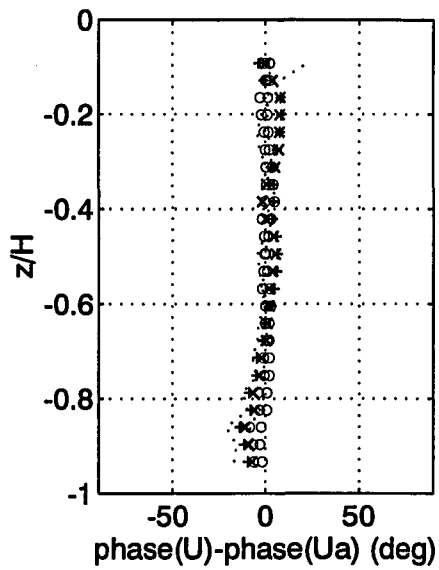
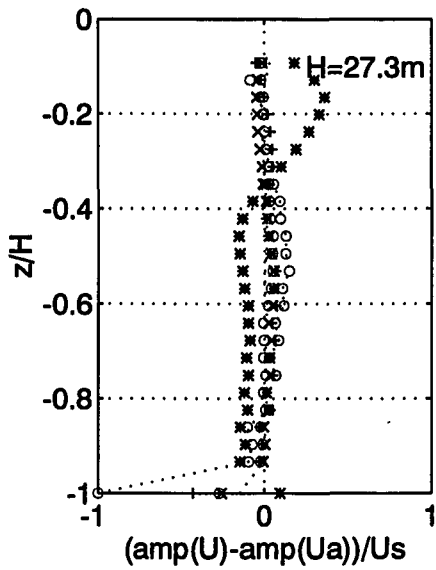
PGA_T	MA0	MA4	Δ	MA8	Δ	MA12	Δ	
A	M_2	4.02	3.98	-1.0%	3.97	-1.2%	3.97	-1.2%
	S_2	0.62	0.61	-1.6%	0.60	-3.2%	0.61	-1.6%
	N_2	1.07	1.06	-0.9%	1.06	-0.9%	1.07	0.0%
	K_1	0.88	0.88	0.0%	0.88	0.0%	0.87	-1.1%
	O_1	0.48	0.47	-2.1%	0.46	-4.2%	0.46	-4.2%
Φ	M_2	285.7	286.0	0.3°	286.1	0.4°	286.5	0.8°
	S_2	191.8	189.8	-2.0°	189.2	-2.6°	189.7	-2.1°
	N_2	202.5	202.4	-0.1°	202.7	0.2°	202.6	0.1°
	K_1	259.3	260.4	1.1°	260.7	1.4°	260.2	0.9°
	O_1	87.6	88.8	1.2°	89.5	1.9°	88.4	0.8°

MA: moving average

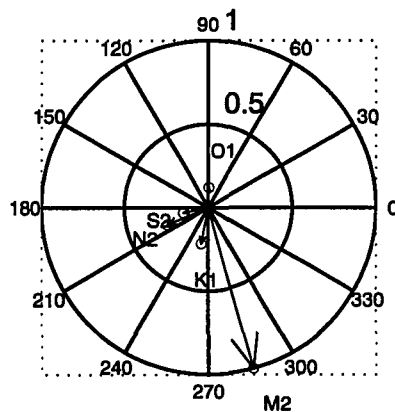
Table VI-28. Comparison of PGA_T estimates from ADCP data without and with N_{2M4} resolution. A: (10^{-3} cm/s²)

PGA_T	I10 (MA12)	I11 (MA12)	$ \Delta $	
A	M_2	3.97	3.93	0.5%
	S_2	0.61	0.61	0.0%
	N_2	1.07	1.07	0.0%
	K_1	0.87	0.88	0.6%
	O_1	0.46	0.47	1.1%
Φ	M_2	286.5	285.9	0.4°
	S_2	189.7	189.7	0.0°
	N_2	202.6	202.4	0.2°
	K_1	260.2	260.0	0.2°
	O_1	88.4	88.2	0.2°

MA: moving average

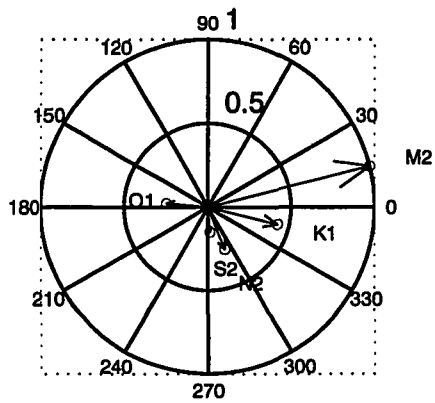
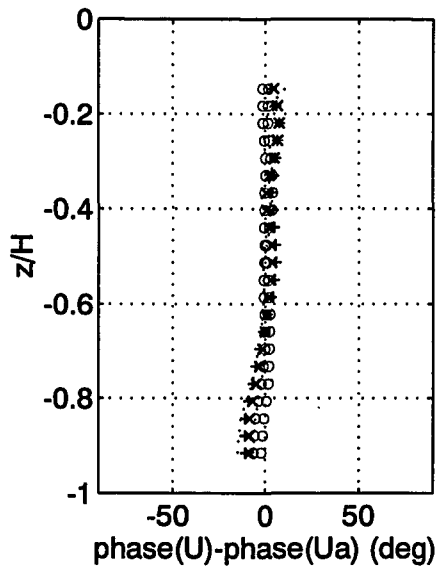
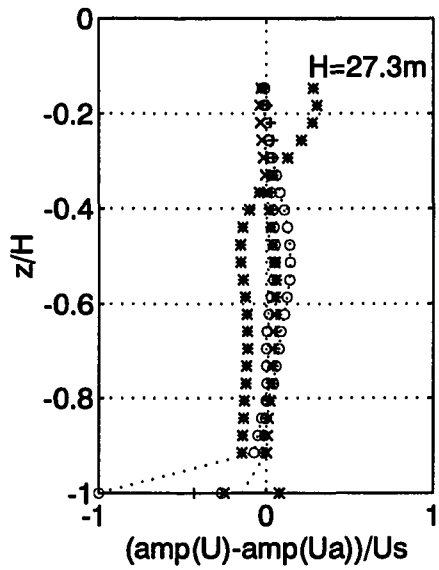


$U_a/U_s: U_s=27.6$

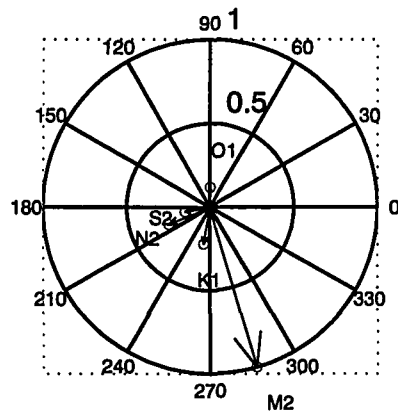


$G/G_s: G_s=4.02E-3$

Fig. VI-D-1a. Currents and estimates of PGA_r at the ADCP station: without smoothing.



$Ua/Us: Us=27.3$



$G/Gs: Gs=3.98E-3$

Fig. VI-D-2a. Currents and estimates of PGA_T at the ADCP station: 4-point moving average.

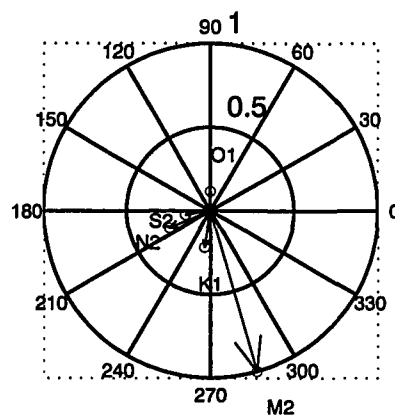
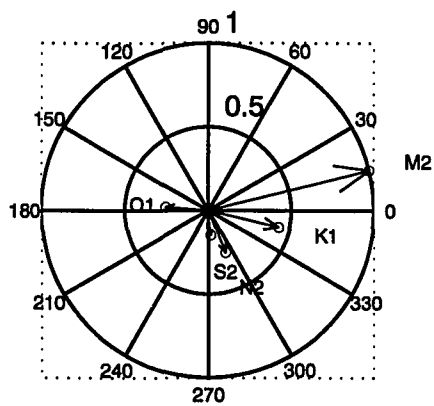
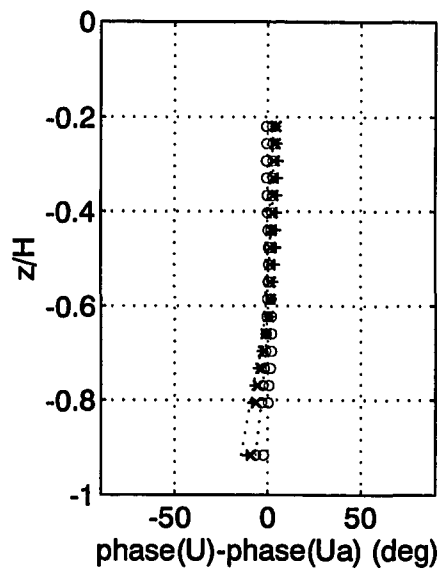
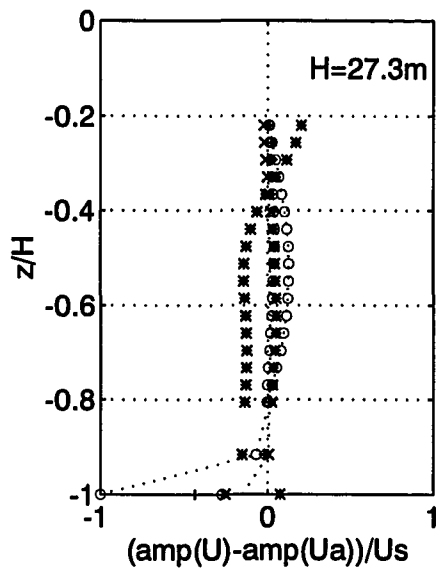


Fig. VI-D-3a. Currents and estimates of PGA_T at the ADCP station: 8-point moving average.

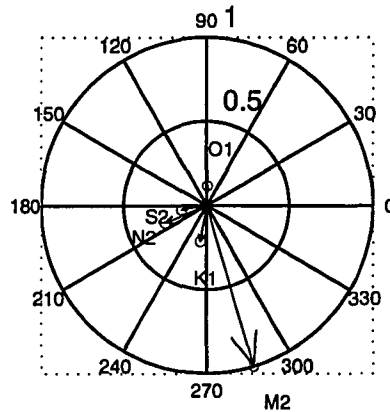
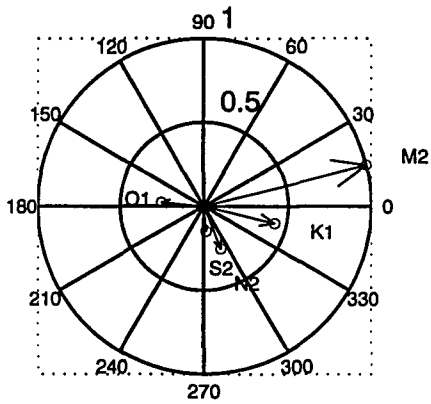
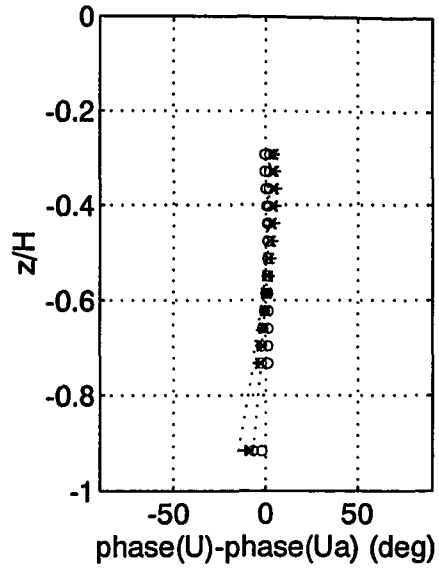
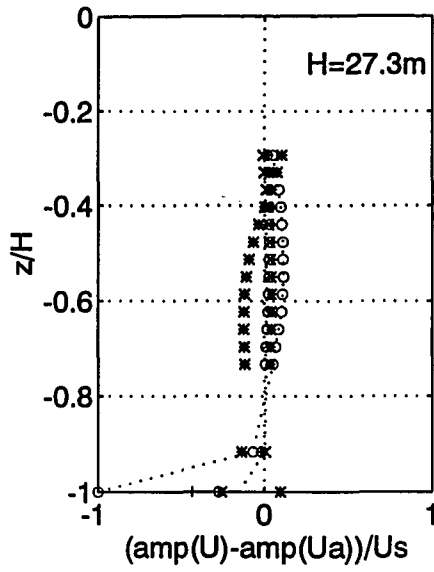
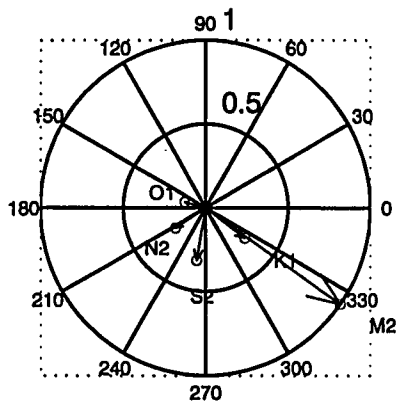


Fig. VI-D-4a. Currents and estimates of PGA_T at the ADCP station: 12-point moving average.



[bottom stress]/Fs: Fs=0.49

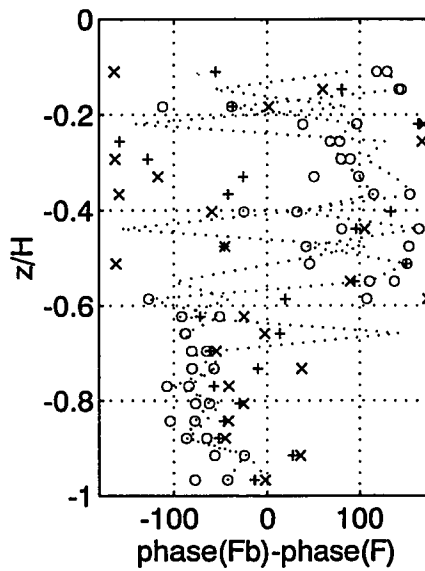
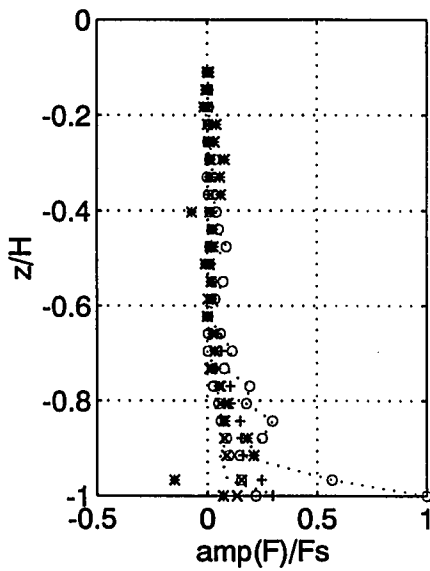
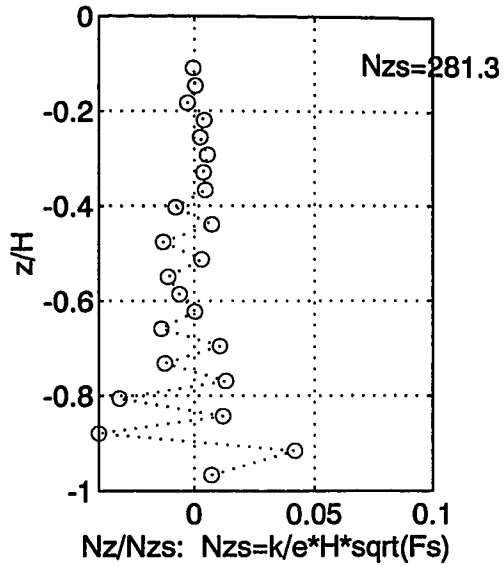
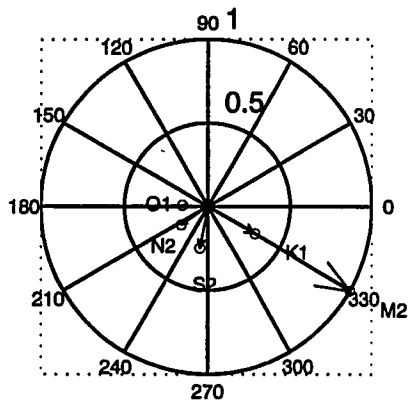
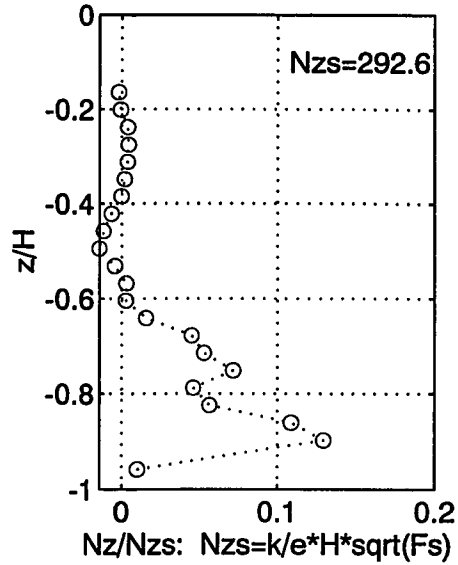


Fig. VI-D-1b. Eddy viscosity and shear stress at the ADCP station: without smoothing.



[bottom stress]/Fs: Fs=0.53



Nz/Nzs: Nzs=k/e*H*sqrt(Fs)

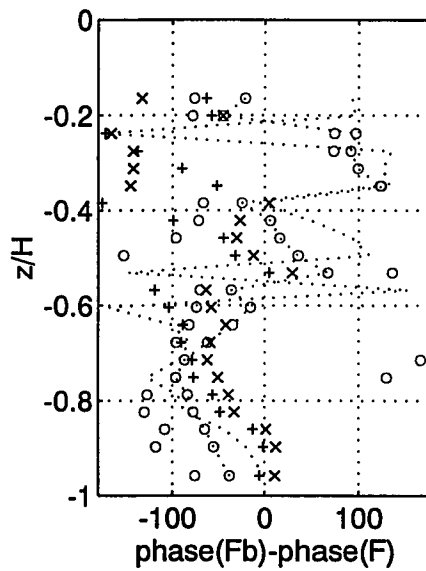
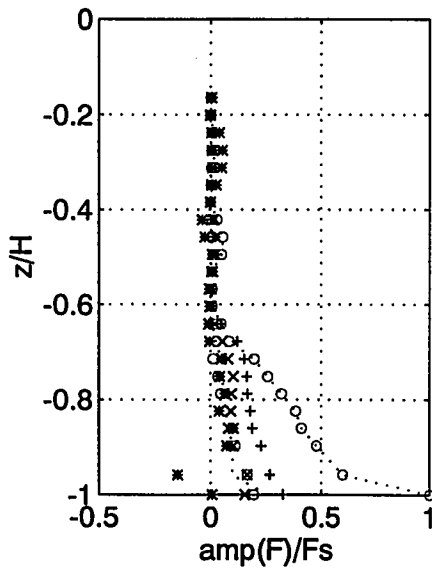
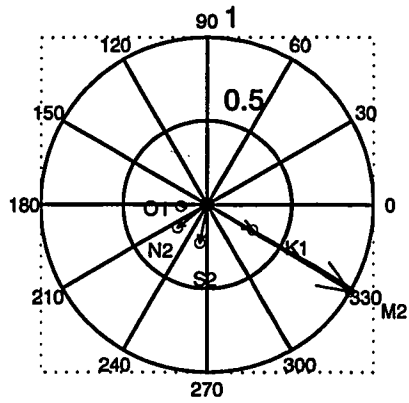


Fig. VI-D-2b. Eddy viscosity and shear stress at the ADCP station: 4-point moving average.



[bottom stress]/Fs: Fs=0.56

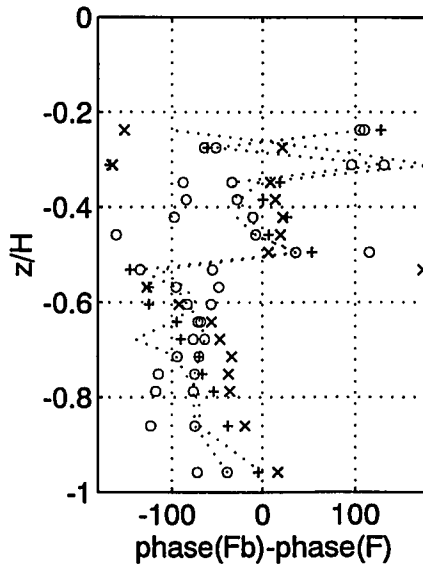
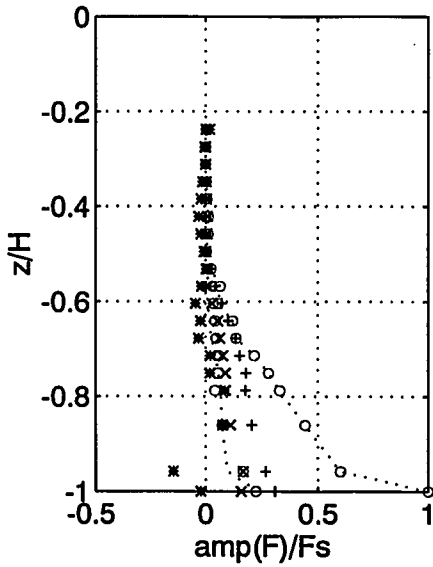
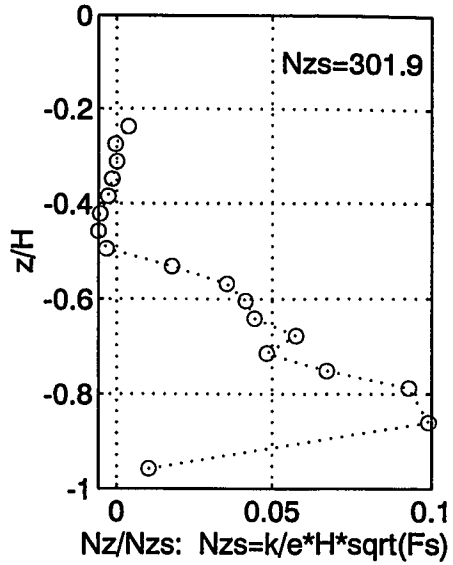


Fig. VI-D-3b. Eddy viscosity and shear stress at the ADCP station: 8-point moving average.

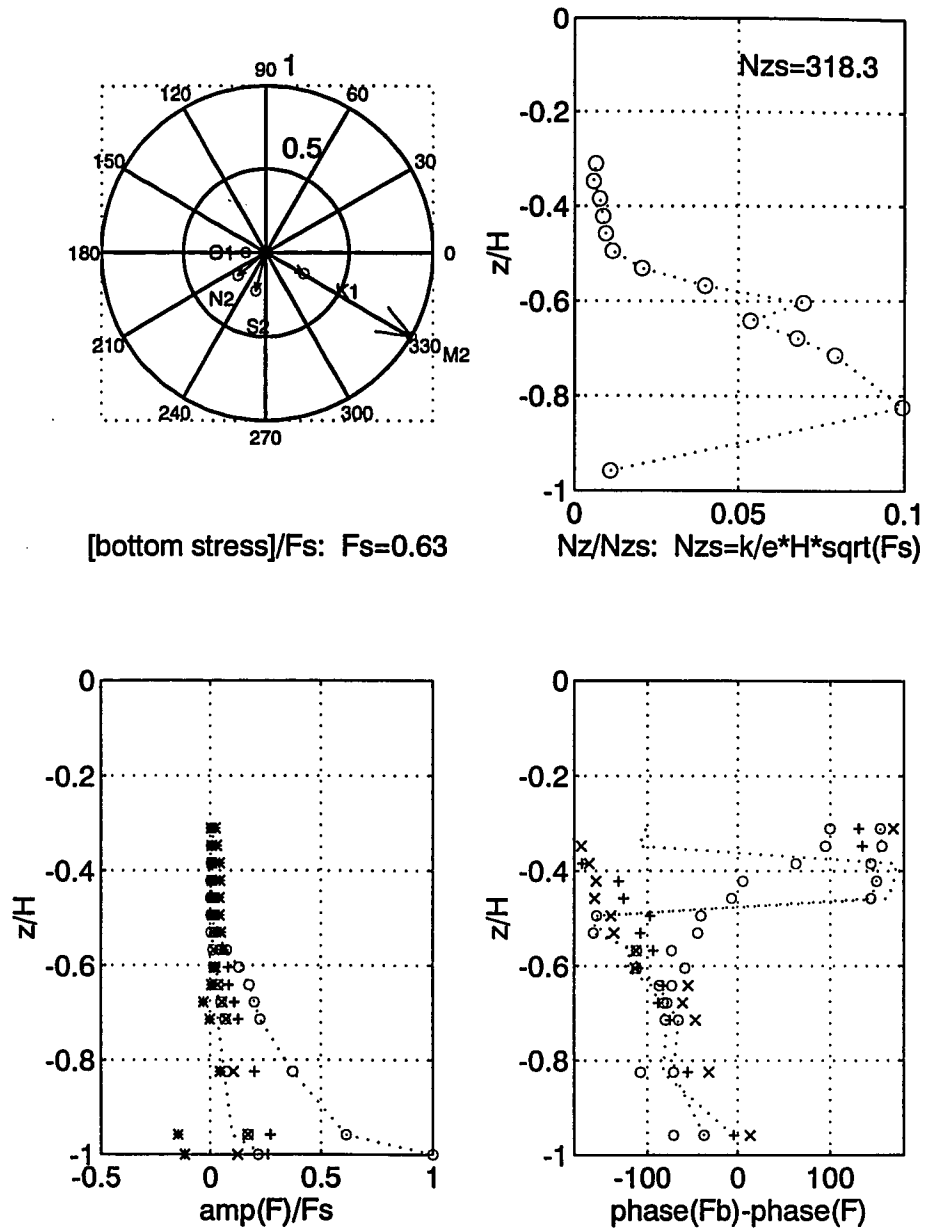


Fig. VI-D-4b. Eddy viscosity and shear stress at the ADCP station: 12-point moving average.

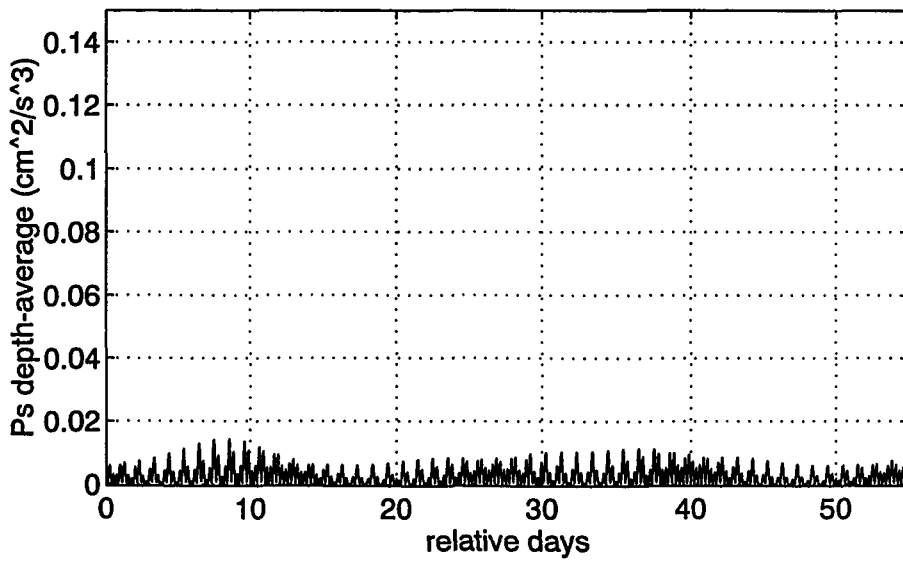
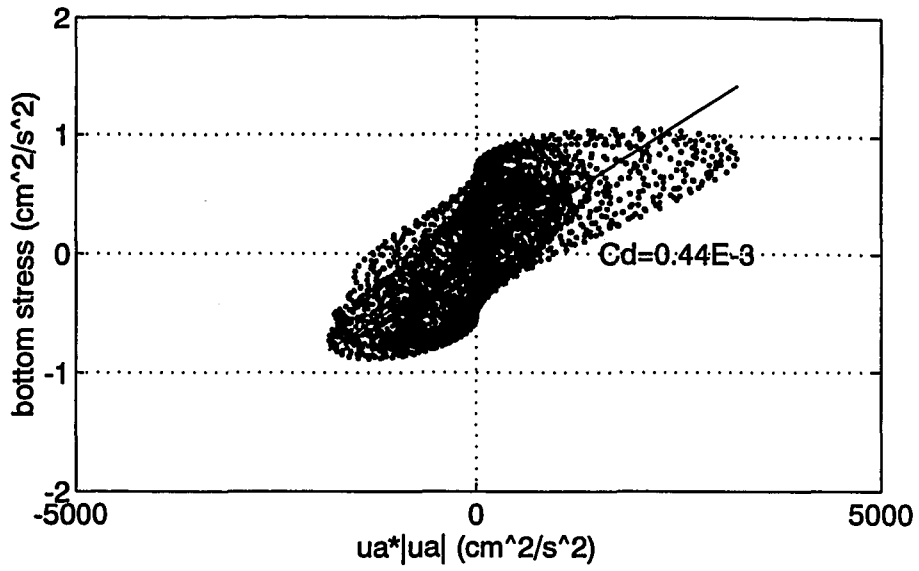


Fig. VI-D-4c. Hysteresis and depth-average TKE production at the ADCP station: 12-point moving average.

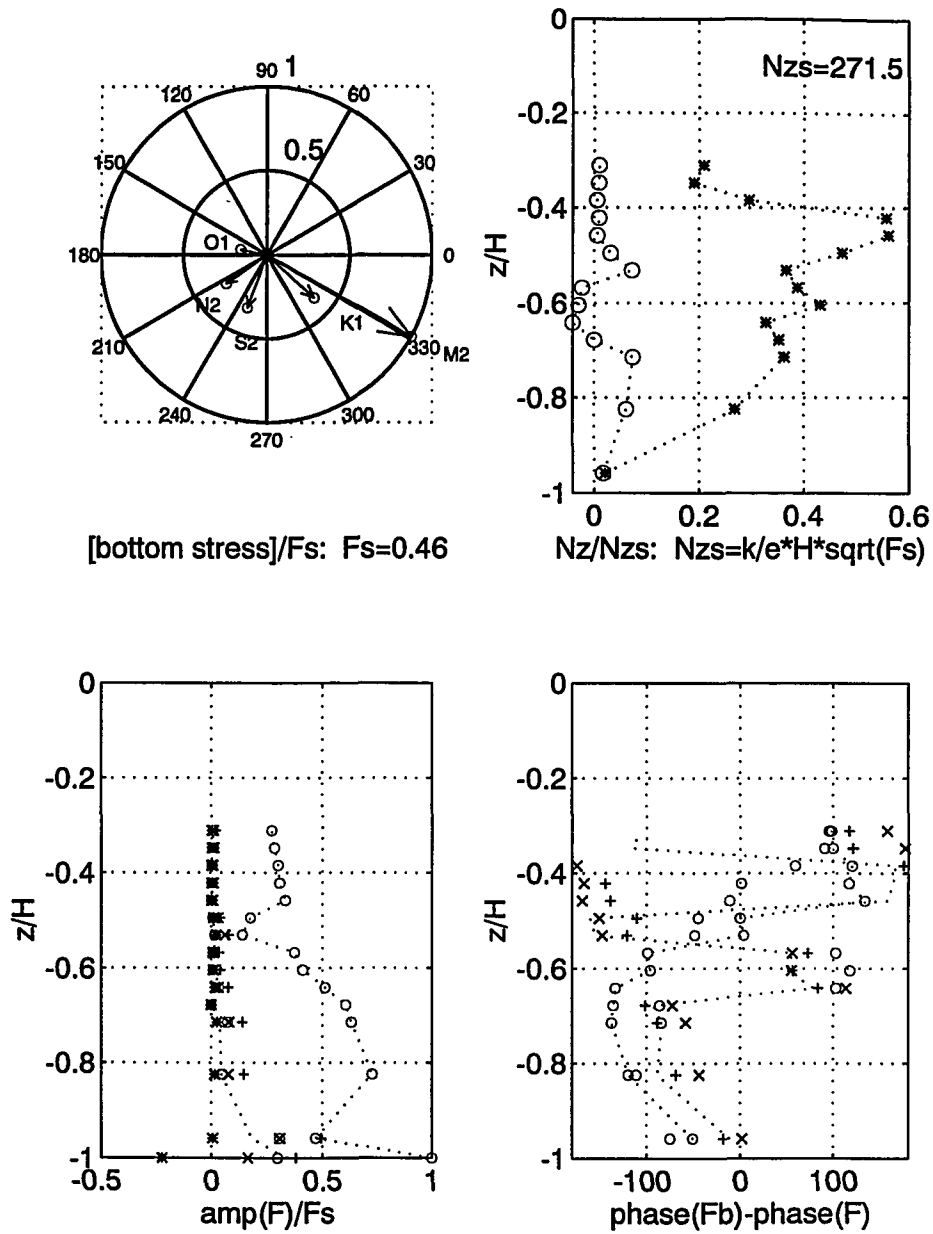


Fig. VI-D-5b. Eddy viscosity and shear stress at the ADCP station: 12-point moving average with N_{zM4} resolution added.

VII. DISCUSSION

A. Pressure Gradient Acceleration

Estimates of PGA_T from the first 2 kinds of data (numerical model, literature) were compared with predetermined reference values.

Model-generated data represented purely rectilinear flow. Inversion experiments reproduced PGA_T in good agreement. Especially, errors associated with the predominant constituent, M_2 , were always $< 1\%$ for amplitude and $< 4^\circ$ for phase.

Literature data represented rather elliptic flow. Moreover, none of datasets was projected on a natural principal flow axis. As a matter of fact, the Coriolis effect should have been considered for u-momentum balance. Nonetheless, these analyses, *per se*, brought in errors $< 12\%$ for amplitude and $< 16^\circ$ for phase with 1-day effective data, and $< 10\%$ for amplitude and $< 8^\circ$ for phase with 1-month effective data.

With harmonic constants of surface elevation reported in N.O.S. (1988), semidiurnal constituents of PGA_T due to surface

slope were determined in the York River. It is found that inverse estimates are closely attached to main trends of the N.O.S. (Fig. VII-1, 2, 3).

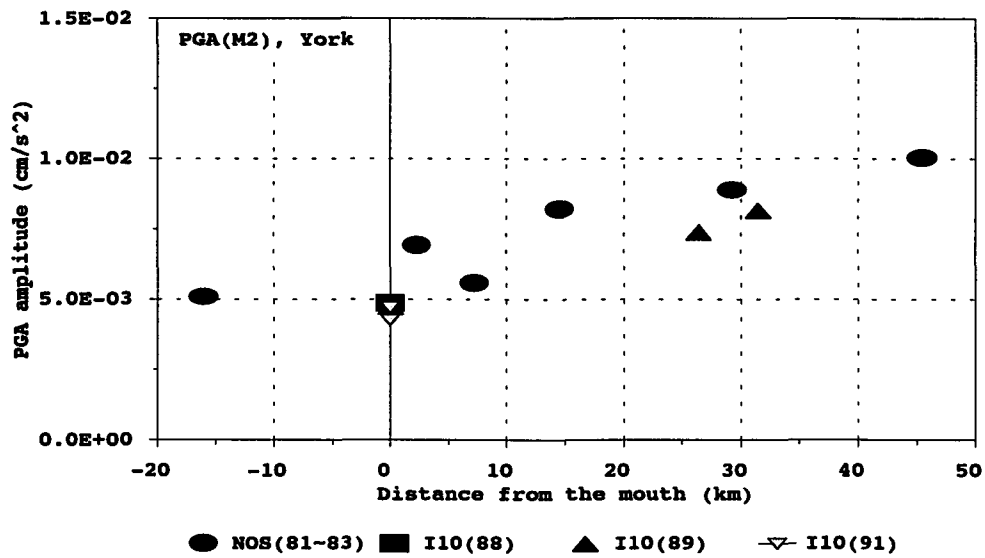


Fig. VII-1. Pressure gradient M_2 in the York River.

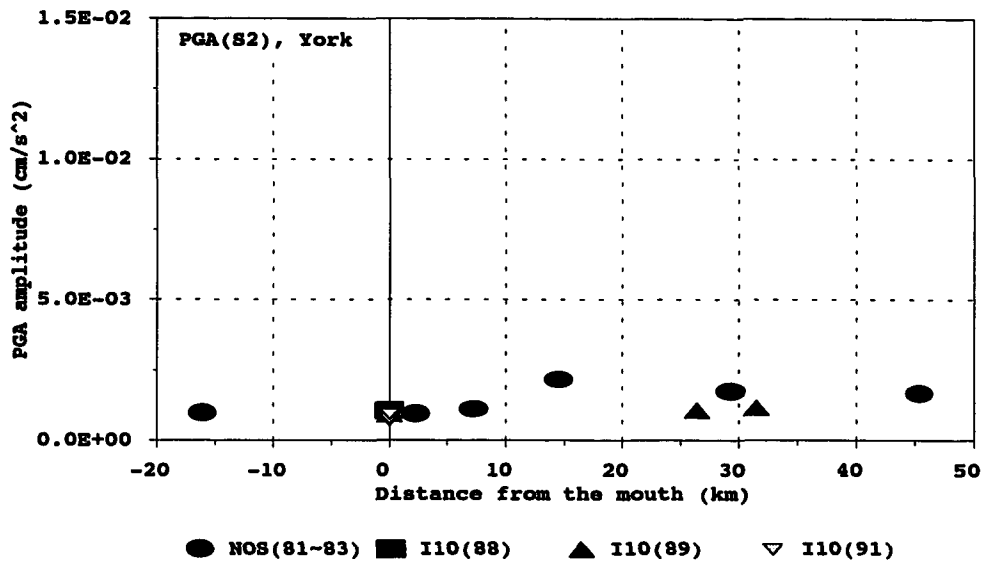


Fig. VII-2. Pressure gradient S_2 in the York River

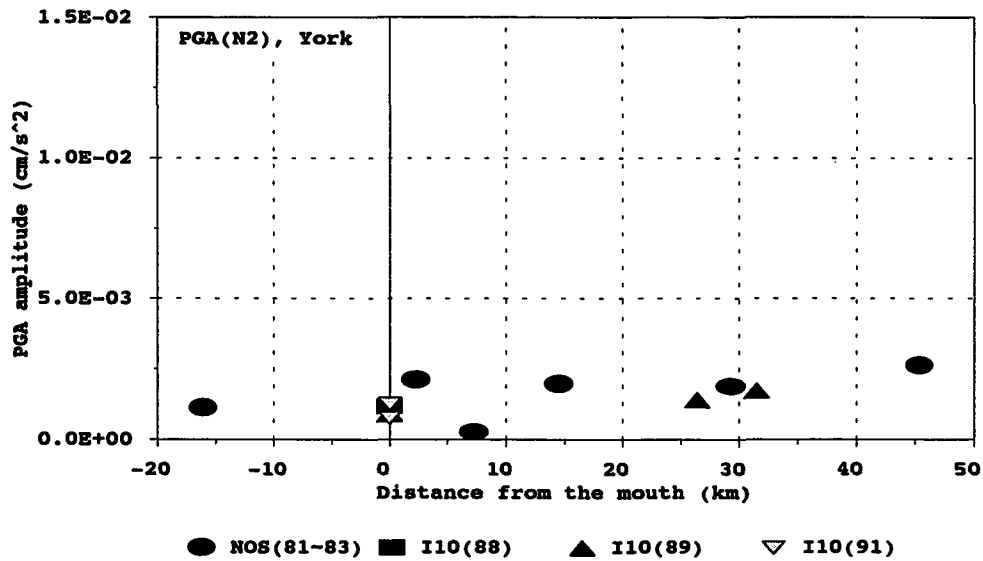


Fig. VII-3. Pressure gradient N_2 in the York River

B. Eddy viscosity

With data generated by a numerical model of purely rectilinear flow, it was shown that errors associated with N_{z0} estimation were $< 13\%$ (8~9% near maximum N_{z0}), except the premeditated one in the bottom layer. When N_{zM4} resolution was added to the inverse system, significant improvement of N_{z0} estimation was mostly observed near the depth of its maximum (error reduction ~8%). Errors associated with N_{zM4} were $< 34\%$ for amplitude and $< 26^\circ$ for phase. Similarity structure was successfully recovered for both N_{z0} and N_{zM4} .

In contrast with the ADCP dataset, the attempt to resolve N_{zM4} was unsuccessful, even with relatively high resolution in the vertical sampling. It is interesting, however, to note that the estimation of PGA_T deteriorated very little. Thus, it is certain that the portion of secondary friction, associated with N_{zM4} , if any, is very insignificant or indistinguishable from other secondary terms. The most probable secondary terms are the nonlinear advection and the Coriolis term.

There may be two causes of the enhancement of the nonlinear advection. The first cause may be a rapid change of channel geometry in the longitudinal direction. The second may be the increase of interaction with time-residual flow due to increase of longitudinal density gradient (e.g. $[u_0 * \partial u_{M2} / \partial x]$,

$[u_{M2} * \partial u_0 / \partial x]$). In order of magnitude, these terms are not comparable to the friction associated with N_{20} (first-order friction). The terms, however, may be greater than or equal to second-order friction associated with N_{2M4} . Also, vertical structure may be inseparable. As a consequence, inverse system becomes more singular.

The second cause may be the Coriolis term. Since currents have been rotated onto a principal axis, this term does not match to the first-order friction either. But it may not be separable from the second-order friction, if the former is significant compared to the latter, but neglected in the inverse model.

Without a doubt, there could have been a combination of two causes. As such is the most probable situation, we have to introduce a linearized (parameterized) version of the nonlinear advective term, or to consider a nonlinear optimization, to resolve N_{2M4} (the simplest model of time-varying eddy viscosity). Even with the suggested 2 approaches, results may not always be successful.

Even with N_{2M4} resolution disregarded, N_{20} estimation was fairly successful in inversions of the model-generated current profiles. This may be due to insensitivity of the tidal current to the nonlinear behavior of the vertical eddy viscosity in time (Tee, 1979). By using time-invariant eddy viscosity profiles, with vertical structure predefined,

Tee (1982) reproduced the observed tidal-current profiles in a well mixed estuary, reasonably well. In a numerical modeling study, Davies (1991) showed that current profiles of both the fundamental and higher harmonics with a fixed viscosity profile (time-invariant viscosity profile effective to a 2½ turbulence energy model) were reproduced to the same level of accuracy as those determined with the turbulence energy model. Therefore, it may be reasonable to regard results of inversion without N_{2M4} valid in the first-order sense.

There was a common pattern in vertical profiles of eddy viscosity. The pattern was such that scaled maximum occurred at $0.7H - 0.8H$ below the surface, and that the scaled viscosity decreased from the maximum toward both the surface and bottom.

From the inversion of the ADCP dataset, it is clearly signaled that the structural form of N_{20} appears to be similar to the linear-exponential form (cf. Fig. VI-D-4b), which is a typical solution of similarity theory in stably stratified planetary boundary layers, found in Businger and Arya (1974):

$$N_{20} = \kappa \cdot u_* \cdot z' \cdot \exp\left(-\frac{z'}{z'_{\max}}\right) \quad \text{VII-(1)}$$

where κ is von Kármán constant, and z' is positive upward. This form is often found as a result of turbulence closure

models (e.g., Mofjeld and Lavelle, 1984; Davies, 1991), or as a solution of similarity theory in vertically well-mixed shallow waters (Smith, 1982).

Further supporting evidence is deduced from Gordon and Dohne (1973). They determined Reynolds stress and turbulence-mean current at 7 depths, from high-frequency current measurements at the time of near-maximum flow in the Choptank River on the eastern shore of Chesapeake Bay. With given profiles of Reynolds stress and turbulence-mean current, it was possible to reconstruct a vertical profile of eddy viscosity (Fig. VII-4). Apparent scaled maximum is $\sim 2.56 \times 10^{-1}$, with $Nzs = 277.0 \text{ cm}^2/\text{s}$, occurring near $\sim 0.8H$ below the surface. The profile also follows the linear-exponential form.

In consequence, a general form of the viscosity may be given as

$$\begin{aligned} N_{z0} &= S_M \cdot \eta_0 \cdot Nzs \cdot \psi(\eta) \\ &= S_M \cdot \eta_0 \cdot \left\{ \frac{\kappa}{e} \cdot H \sqrt{\tau_B} \right\} \cdot \psi(\eta) \end{aligned}$$

or

VII-(2)

$$N_{z0} = S_M \cdot [\eta_0 \cdot \left\{ \frac{\kappa}{e} \cdot \left(\frac{\tau_B}{\bar{u}^2} \right)^{\frac{1}{2}} \right\}] \cdot \bar{u} \cdot H \cdot \psi(\eta)$$

where S_M denotes a stability function, $\eta = (z+H)/H$, and $\psi(\eta)$ is represented by

$$\psi(\eta) = \frac{\epsilon}{\eta_0} \cdot \eta \cdot \exp\left(-\frac{\eta}{\eta_0}\right) \quad \text{VII-(3)}$$

The function $\psi(\eta)$, ranging from 0 to 1, has a maximum at $\eta = \eta_0$. It is worth noting that the second form in VII-(2) is compatible to the one in II-(1). Typical shapes of $\eta_0 * \psi(\eta)$ are illustrated in Fig. VII-5, with $\eta_0 = 0.2$ and 0.3 (or $z_{\max}/H = -0.8$ and -0.7).

At the ADCP station, the scaled viscosity profile appears to be reduced from profiles in Fig. VII-5. The reduction seemed rather more intense in the upper water column than near the depth of maximum (cf. Fig. VI-D-4b). This may indicate the influence of stratification.

Parameters Nzs and η_0 may change in time. Nzs may change in time, primarily due to the variation of bottom-roughness. Meanwhile, η_0 time-variation may be associated with the variation of both bottom roughness and water-column stability. Accordingly, water-column stability may influence the eddy-viscosity profile in 2 ways: through changes in magnitude (S_M) and shape (η_0).

Scaled eddy viscosity can be a measure of water-column stability. At the station 'Tu91', it was shown that the apparent maximum increased by a factor of ~ 2 from the early

summer to the mid-summer, and by a factor of ~2 from the mid-summer to the late summer/early fall (cf. Table VI-19). At the station 'NOS066', the maximum increased by a factor of ~2 from the mid-spring to the mid-summer (cf. Table VI-24). At the station 'NOS121', the maximum varied significantly by a factor of ~3 from the early winter to the mid/late spring (factor ~3 decrease) and from the summer to the mid/late fall (factor ~3 increase) (cf. Table VI-24).

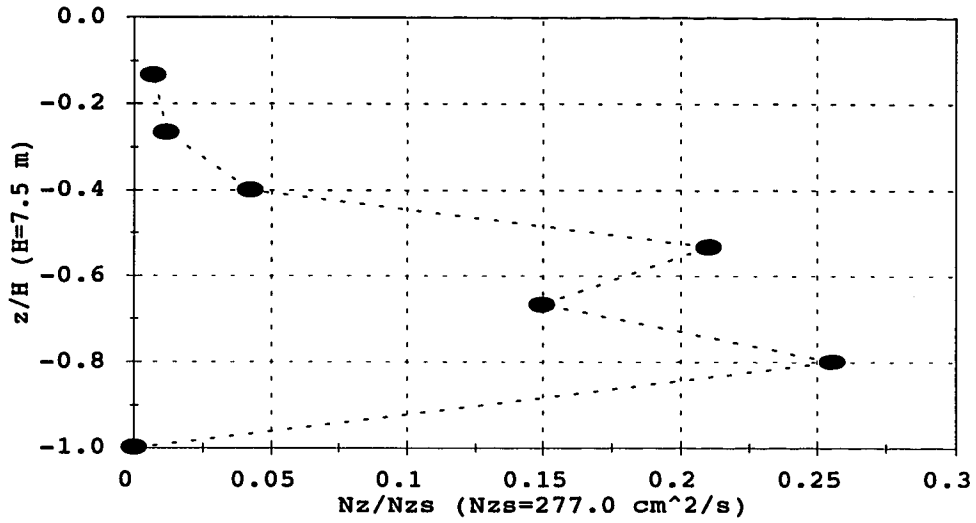


Fig. VII-4. Eddy-viscosity profile reconstructed from Gordon and Dohne(1973).

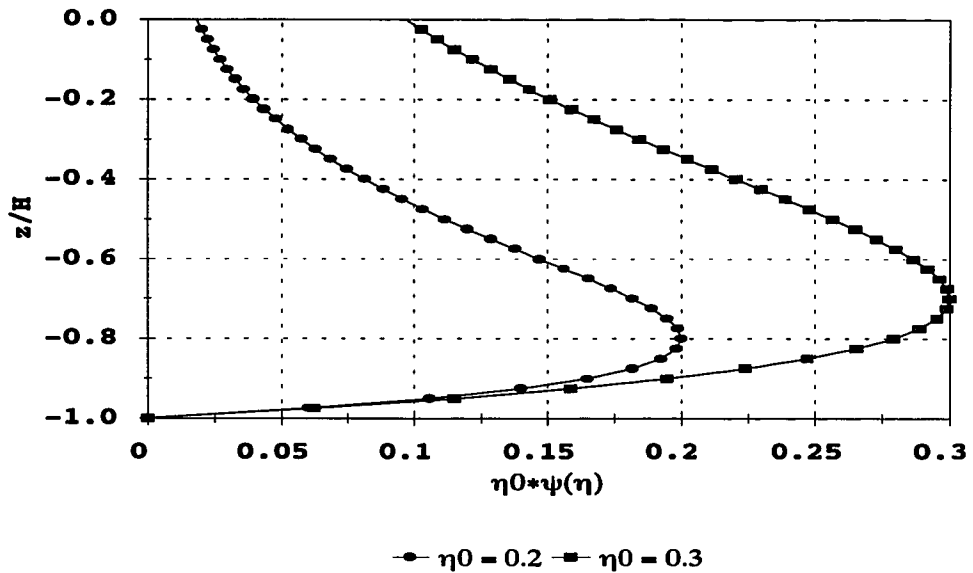


Fig. VII-5. Model eddy-viscosity profile in VII-(3), with η_0 multiplied.

C. Shear stress and Depth-Average *TKE* Production

The maximum bottom stress varied significantly in locality and season. The overall range was $0.7 - 3.7 \text{ cm}^2/\text{s}^2$ ($\approx 0.7 - 3.7 \text{ dynes/cm}^2 = 0.07 - 0.37 \text{ Pa}$): $\sim 1.8 \text{ cm}^2/\text{s}^2$ at the upper-York stations, $1.5 - 2.0 \text{ cm}^2/\text{s}^2$ at the lower-York stations, $3.7 \text{ cm}^2/\text{s}^2$ at the lower-bay station, $\sim 1.0 \text{ cm}^2/\text{s}^2$ at the ADCP station, and $0.7 - 1.9 \text{ cm}^2/\text{s}^2$ at the upper-bay station. Due to the phase difference, an hysteresis effect was always observed between bottom stress and depth-mean current.

The lower-bay station 'NOS066' is located near the study site of bottom-boundary layer ('Wolf Trap' at $37^\circ 16.3'N$, $76^\circ 8.57'W$) by Wright et al.(1992). The site has a different total depth (11 - 12 m), and was occupied in different years (1987, 1989, 1991). Based on their estimates, the maximum bottom-stresses were $0.3 - 0.4 \text{ Pa}$ in June('87) and April('88), and were $0.2 - 0.3 \text{ Pa}$ in February('91). Values, especially in April and June, are comparable to the estimate derived from inverse analysis at the lower-bay station, $\sim 0.37 \text{ Pa}$.

When a current system is strongly dissipative, internal friction tends to be constant through depth. Then internal stress tends to be linear (Tee, 1979). Typical systems can be found in shallow waters, such as in Bowden and Fairbairn(1952) and Tee(1982). In contrast, the present study shows that internal-stress profiles have upward-concave structure.

Apparently, the structure changed seasonally, but never approached the linear trend.

Estimates of water column-effective drag coefficient (C_d) ranged from 0.2×10^{-3} to 1.6×10^{-3} . It is smaller than typical literature values for shallow waters such as $(2 - 4) \times 10^{-3}$ (Bowden, 1983) and 2×10^{-3} (Csanady, 1982). This may be ascribed to bottom roughness element. In the lower bay, it is reported that bottom sediments, for the most part, are blended with sands, silts and clays (Byrne et al., 1982), which implies a smooth bottom.

In the York River, C_d values were higher in summer ($\sim 1.07 \times 10^{-3}$ at the mouth) than in winter ($\sim 0.45 \times 10^{-3}$ in the upper part). It is an interesting fact that the water column with ~ 2 times deeper depth (at the mouth) has ~ 2 times higher C_d , which is contradictory to the general notion that the coefficient depends only on the ratio z_0/H (e.g. Mofjeld, 1988). Thus, it is reasoned that the difference may be due to a seasonal variation of biological roughness.

At the lower bay station, C_d estimates were 0.98×10^{-3} in mid-spring and 1.24×10^{-3} in mid-summer. At the ADCP station (mid-bay), C_d was estimated as 0.45×10^{-3} (early spring). Meanwhile, at the upper bay station, there was a distinctive seasonal change in C_d : 0.68×10^{-3} in early winter, 0.22×10^{-3} in mid/late spring, 0.43×10^{-3} in summer and 1.61×10^{-3} in mid/late fall. The apparent minimum occurred in mid/late spring, while

the maximum did in mid/late fall. Again, the change may be ascribed to the variation of biological roughness. However, the addressed reason can not be emphasized as definite, until seasonal succession of benthic biota is fully investigated in the region.

Depth-average *TKE* production was derived from current profiles and estimates of PGA_T . PGA_T estimates were among primary results of inversions, which were compared in good agreement with other direct references. The estimates of depth-average *TKE* production, accordingly, tend to bear uncertainty no more than PGA_T estimates do.

In the bay mainstem, the depth-average *TKE* production appears to be significantly higher in the lower bay than in the mid-bay or in the upper bay. Maximum (perigean-spring-diurnal maximum) was roughly $\sim 0.08 \text{ cm}^2/\text{s}^3$ (both mid-spring and mid-summer) at the lower-bay station, $\sim 0.01 \text{ cm}^2/\text{s}^3$ (early summer) at the mid-bay station (i.e. *ADCP* station), and $0.004 - 0.02 \text{ cm}^2/\text{s}^3$ (4 seasons) at the upper-bay station.

D. Role of $u_0(z)$ in Inverse Systems

When the $u_0(z)$ -associates (i.e. both equation and unknowns for PGA_0) were excluded from the inverse system, results for both PGA_T and N_{20} were not significantly different from those with the associates (cf. Table VI-11 and VI-12).

The values of v rather decreased without the $u_0(z)$ -associates.

The reason is the dominance of tidal flow over the time-residual $u_0(z)$. From a physical standpoint, the barotropic force is well determined because of the tidal dominance, and tidal currents produce the greater part of turbulent kinetic energy, and hence are mostly responsible for N_{20} .

VIII. CONCLUSIONS

A simple inverse method has been devised to diagnose the linearized momentum balance governing tidal currents in shallow coastal waters, and to determine the vertical structure of vertical shear stress. Assuming a harmonic time dependence, harmonic constants, determined from current measurements at several depths, are utilized as the only inputs. The method employs a least-squares analysis of the resulting overdetermined system of equations to estimate the friction and horizontal pressure gradient terms. Shear stress was parameterized in terms of vertical eddy viscosity, represented as a time-constant term and an oscillatory component. The vertical structure was not predefined.

Barotropic pressure gradients and profiles of vertical eddy viscosity (the M_4 oscillating component as well as the time-constant component) were successfully recovered through experiments with the inverse method on data generated by a numerical model of unstratified flow. A similar experiment on a set of *ADCP* measurements in Chesapeake Bay was not successful in an attempt to resolve the oscillating part of eddy viscosity. However, for the first-order friction, i.e.,

that associated only with time-constant eddy viscosity, reasonable results were obtained. As addressed in the previous chapter, the failure is mainly ascribed to the truncation of advective terms. The three-term dynamic balance (local acceleration, pressure gradient and friction), however, is still strongly effective in the estimation of the time-constant viscosity profile. On this ground, analyses were taken into account only with the time-constant eddy viscosity model.

Strong similarity was found between the eddy-viscosity profile estimated from the *ADCP* measurements and one reconstructed from published values of Reynolds stresses and turbulence-mean currents measured at a location near the *ADCP* deployment site. The structural shape appears to be linear-exponential, as found in asymptotic solutions of similarity theory in a stable boundary layer, and similar to the time-average of profiles from numerical modeling with turbulence closure schemes.

The method proved quite successful in determining barotropic pressure gradients from current data. Utilizing only the harmonic constants (for currents) reported in published studies of tidal flows, the inverse method produced estimates of pressure gradients that agreed well (within ~10% for amplitude and 10 - 20 degrees for phase) with reported values that were based on direct pressure measurement. Also,

pressure gradients determined by inverse analysis of current data at several locations in the York River were highly consistent with the longitudinal distribution of values derived from surface elevations. Bottom stress in the lower bay, determined as a secondary result, appears to have a similar range of time variation to results determined from a tripod study in the bottom boundary layer.

In view of the results from these varied applications and consistency checks, the proposed inverse approach appears to perform satisfactorily enough to resolve barotropic pressure gradients and vertical profiles of time-constant eddy viscosity (i.e., up to the first-order friction). Secondary results involve bottom stress, water-column effective drag coefficient (C_d), depth-average *TKE* production and internal stress. These are deduced from the depth-average balance and current shear, using primary results. It is noted that the secondary estimations are nothing more than recombinations of inputs and primary results, hence with roughly the same degree of uncertainty. If any secondary result does not make physical sense, it could be ascribed to the misfit in one of primary results.

Results of analyses in Chesapeake Bay and the York River yield the following conclusions:

- Eddy viscosity profiles, determined for various locations and times, have similar structure. The structure is very

close to the similarity solution for a stably stratified atmospheric boundary layer (Businger and Arya, 1974), and appears to be similar to the structure found in numerical modeling with turbulence-closure schemes (up to the order $2\frac{1}{2}$) (e.g. Davies, 1991).

- The scaled apparent-maximum of eddy viscosity, which includes water-column stability information, appears to change significantly in season: low in spring and summer, high in fall and winter. Meanwhile, the depth of apparent-maximum appears to be maintained as $0.2H - 0.3H$ from the bottom.
- Internal stress tends to decrease more rapidly from the bottom and becomes more uniform near the surface (concave upward), which is contrasted to the linear profile of strongly dissipated flow system in homogeneous water columns. Degree of concavity tends to be larger, when the scaled maximum of eddy viscosity becomes smaller.
- Overall estimates of C_d , $0.2 \times 10^{-3} - 1.6 \times 10^{-3}$, are obviously lower than typical values in the literature, $2 \times 10^{-3} - 4 \times 10^{-3}$. Also, a tendency towards seasonal change is shown among estimates. At the lower bay and the York stations, C_d tends to be the smallest during winter and the largest during summer. At the upper bay station, C_d tends to be the smallest during spring and the largest

during fall.

- Depth-average *TKE* production in the lower bay appears to be ~8 times higher than in the mid- and upper bay. Also, overall concavity of internal stress seems much lower in the lower bay than in the upper bay. Apparently, flow at the lower bay station is much more turbulent than at the upper bay station.
- Depth-average *TKE* production in the upper York appears to be 3 - 4 times higher than in the lower York. Overall degree of concavity is much lower in the upper York than in the lower York. Thus, flow at the upper York stations appears to be much more turbulent than at the lower York stations.

Some strengths of the proposed inverse approach may be noted. The method requires only current measurements. It is much simpler than an adjoint-variational optimization approach, but is capable of diagnosing the first-order dynamic balance. With respect to first-order friction, the method is able to resolve the vertical structure of time-constant eddy viscosity. Thus, it can be a strong tool to investigate both internal and bottom friction with only current-profile measurements. Due to the simplicity and the time-efficiency for the diagnosis of the first-order dynamic balance, it may be successfully used to study unknown force structure from

ADCP measurements in field.

On the other hand, the application of the method is limited only to (quasi-) deterministic waves, and requires suitable length of time series to resolve dominant frequency band(s). Hence, results are only applicable to flow conditions similar to those during the sampling period. It is not appropriate for strongly advective flows. Even for weakly advective flows, it may not be successful in determining the oscillating part of the viscosity, due to the neglected advective terms.

Future directions include 1) to design a 3-dimensional version with ellipse parameters being used instead of rectilinear harmonics, that is to consider the Coriolis effect, 2) to devise a 'broad-band' version, not limited to pure deterministic waves, and 3) to apply the method to an inertial-flow (or combination of both inertial and tidal flow) environment.

LITERATURE CITED

- Anwar, H. O., 1983. Turbulence measurements in stratified and well-mixed estuarine flows. *Estuar., Coast. Shelf Sci.* 17:243-260.
- Bowden, K. F., 1960. Circulation and mixing in the Mersey estuary. *I.A.S.H. Comm. of Surface Waters Publ.* 51:352:360
- Bowden, K. F., 1983. ***Physical Oceanography of Coastal Waters.*** 302pp., Ellis Horwood Limited, Chicester.
- Bowden, K. F. & L. A. Fairbairn, 1952. A determination of the frictional forces in a tidal current. *Proc. Royal Soc. London A* 214:371-392.
- Bowden, K. F. & L. A. Fairbairn, 1956. Measurements of turbulent fluctuations and Reynolds stresses in a tidal current. *Proc. Royal Soc. London A* 237:422-438.
- Bowden, K. F., L. A. Fairbairn & P. Hughes, 1959. The distribution of shearing stresses in a tidal current. *Geophys. J. of the Royal Astr. Soc.* 2:288-305.
- Businger, J. A. & S. P. S. Arya, 1974. Height of the mixed layer in the stably stratified planetary boundary layer. *Advances in Geophysics* Vol. 18A:73-92, Academic Press.
- Byrne, R. J., C. H. Hobbs, H. H. Seliger & M. A. Tyler, 1982. Baseline sediment studies to determine distribution, physical properties, sedimentation budgets and rates in the Virginia portion of the Chesapeake Bay. *Final Report to U.S. EPA*, 155pp.
- Candela, J., R. C. Beardsley & R. Limeburner, 1992. Separation of tidal and subtidal currents in ship-mounted Acoustic Doppler Current Profiler observations. *J. Geophys. Res.* 97(C1):769-788.
- Csanady, G. T., 1982. ***Circulation in the Coastal Ocean.*** 279pp., R. Reidel, Dordrecht, Holland.
- Davies, A., 1991. On using turbulence energy models to develop spectral viscosity models. *Cont. Shelf Res.*

11(11):1313-1353.

- Dyer, K. R., 1988. Tidally generated estuarine mixing processes. In: *Hydrodynamics of estuaries*, Kjerfve, Björn. (ed.). CRC Press, FL.
- Fang, G. & T. Ichiye, 1983. On the vertical structure of tidal currents in a homogeneous sea. *Geophys. J. of the Royal Astr. Soc.* 2:288-305.
- Fiadeiro, M. E. & G. Veronis, 1984. Obtaining velocities from tracer distributions. *J. Phys. Oceanogr.* 14:1734-1746.
- Fisher, C. W., 1986. *Tidal Circulation in Chesapeake Bay*. Ph. D. dissertation, Old Dominion University. 255pp.
- Francis, J. R. D., H. Stommel, H. G. Farmer & D. Parson, Jr., 1953. Observations of turbulent mixing processes in a tidal estuary. Ref. 53-22. 20pp., Woods Hole Oceanogr. Inst., Woods Hole, Mass.
- Galperin, B., L. H. Kantha, S. Hassid & A. Rosati, 1988. A quasi-equilibrium turbulent energy model for geophysical flows. *J. Atmos. Sci.* 45(1):55-62.
- Gibson, M. M., B. E. Launder, 1978. Ground effects on pressure fluctuations in the atmospheric boundary layer. *J. Fluid Mech.* 86:491-511.
- Godin, G., 1991. Compact approximations to the bottom friction term, for the study of tides propagating in channels. *Cont. Shelf Res.* 11(7):579-589.
- Goodrich, M. D., W. C. Boicourt, P. Hamilton & D. W. Pritchard, 1987. Wind-induced destratification in Chesapeake Bay. *J. Phys. Oceanogr.* 17(12):2232-2240.
- Gordon, C. M. & C. F. Dohne, 1973. Some observations of turbulent flow in a tidal estuary. *J. Geophys. Res.* 78(12):1971-1978.
- Guohong Fang & T. Ichiye, 1983. On the vertical structure of tidal currents in a homogeneous sea. *Geophys. J. R. astr. Soc.* 73:65-82.
- Hogg, N. G., 1987. A least-squares fit of the advective-diffusive equations to Levitus Atlas data. *J. Mar. Res.* 45:347-375.
- Ianiello, J. P., 1977. Tidally induced residual currents in estuaries of constant breadth and depth. *J. Mar. Res.* 35(4):755-786.

- Ianiello, J. P., 1979. Tidally induced residual currents in estuaries of variable breadth and depth. *J. Phys. Oceanogr.* 9:962-974.
- Kuo, A. Y., B. J. Neilson, J. M. Brubaker and Evon P. Ruzecki, 1993. DATA REPORT: HYPOXIA IN THE YORK RIVER, 1991. Data Report #47, VIMS/SMS, College of William and Mary, Gloucester Point, VA 23062.
- Lauder, B. E., G. J. Reece & W. Rodi, 1975. Progress in the development of a Reynolds-stress turbulence closure. *J. Fluid Mech.* 68:537-566.
- Marmorino, G. O. & C. L. Trump, 1992. Acoustic Doppler Current Profiler measurements of possible lee waves south of Key West, Florida. *J. Geophys. Res.*, 97(C5):7271-7275.
- Maas, L. R. M. & J. J. M. van Haren, 1987. Observations on the vertical structure of tidal and inertial currents in the central North Sea. *J. Mar. Res.* 45(2):293-318.
- Mellor, G. L. & T. Yamada, 1982. Development of a turbulence closure model for geophysical fluid problems. *Rev. Geophys. Space Phys.* 20(4):851-875.
- Mofjeld, H. O. & J. W. Lavelle, 1984. Setting the length scale in a second-order closure model of the unstratified bottom boundary layer. *J. Phys. Oceanogr.* 14:833-839.
- Mofjeld, H. O., 1988. Depth dependence of bottom stress and quadratic drag coefficient for barotropic pressure-driven currents. *J. Phys. Oceanogr.* 18:1658-1669.
- Moore, A. M., 1992. Data assimilation in a quasi-geostrophic open ocean model of the Gulf Stream region using the adjoint method. *J. Phys. Oceanogr.* 21:398-427.
- Panchang, V. G. & J. E. Richardson, 1993. Inverse adjoint estimation of eddy viscosity for coastal flow models. *J. Hydr. Eng.* 119(4):506-524.
- Parker, B. B., 1988. Tide and tidal currents in the Chesapeake Bay. U. S. National Ocean Survey. NOAA Technical Report NOS OMA 3, National Ocean Survey, NOAA, Dept. of Commerce, 84 pp.
- Pingree, R. D. & L. Maddock, 1978. The M4 tide in the English Channel derived from a non-linear numerical model of the M2 tide. *Deep Sea Res.* 25:53-63.

- Press, W. H., B. P. Flannery, S. A. Teukolsky & W. T. Vetterling, 1990. *Numerical Recipes in C: The Art of Scientific Computing*, 735 pp., Cambridge Univ. Press, NY.
- Pritchard, D. W., 1989. Estuarine Classification - a Help or a Hindrance. In: *Estuarine Circulation*, B. J. Neilson, A. Y. Kuo and J. Brubaker (eds.). Humana Press, NJ.
- Rodi, W., 1987. Examples of calculation methods for flow and mixing in stratified fluids. *J. Geophys. Res.* 92(C5):5305-5328.
- Rossby, C. G. & R. B. Montgomery, 1935. The layer of frictional influence in wind and ocean currents. *Papers in Physical Oceanography and Meteorology*
- Sasaki, Y., 1970. Some basic formalisms in numerical variational analysis. *Monthly Weather Review* 98(12):875-883.
- Schott, F. & W. Johns, 1987. Half-year-long measurements with a buoy-mounted Acoustic Doppler Current Profiler in the Somali Current. *J. Geophys. Res.* 92(C5):5169-5176.
- Schröder M. & G. Siedler, 1989. Turbulent momentum and salt transport in the mixing zone of the Elbe Estuary. *Estuar., Coast. Shelf Sci.* 28:615-638.
- Seitz, R. C., 1973. Observations of intermediate and small scale turbulent water motion in a stratified estuary (I and II). *Ches. Bay Inst. Tech. Rep.* 79
- Simpson, J. H., E. G. Mitchelson-Jacob & A. E. Hill, 1990. Flow structure in a channel from an acoustic Doppler current profiler. *Cont. Shelf Res.* 10:589-603.
- Sisson, G. M., A. Y. Kuo & J. M. Brubaker, 1991. DATA REPORT: HYPOXIA IN THE YORK RIVER, 1988-1989. Data Report #33, VIMS/SMS, College of William and Mary, Gloucester Point, VA23062.
- Smith, T. J., 1982. On the representation of Reynolds stress in estuaries and shallow coastal seas. *J. Phys. Oceanogr.* 12:914-921.
- Tee, Kim-Tai, 1979. The structure of three-dimensional tide-generating currents. Part I: Oscillating currents. *J. Phys. Oceanogr.* 9:931-944.
- Tee, Kim-Tai, 1982. The structure of three-dimensional

- tide-generating currents: experimental verification of a theoretical model. *Estuar., Coast. Shelf Sci.* 14:27-48.
- Uncles, R. J., 1981. A note on tidal asymmetry in the Severn Estuary. *Estuar., Coast. Shelf Sci.* 13:419-432.
- Uncles, R. J., 1988. Tidal dynamics of Estuaries. In: *Hydrodynamics of Estuaries*, Vol.1, Björn Kjerfve(ed.). Springer-Verlag, NY.
- Wolf, J., 1980. Estimation of shearing stresses in a tidal current with application to the Irish Sea. In: *Marine Turbulence*, J. C. J. Nihoul (ed.). Elsevier Scientific Publishing Company, Amsterdam, pp. 319-344.
- Wright, L. D., J. D. Boon, J. P. Xu & S. C. Kim, 1992. The bottom boundary layer of the bay stem plains environment of lower Chesapeake Bay. *Estuar., Coast. Shelf Sci.* 35:17-36.
- Wunsch, C., 1988. Transient tracers as a problem in control theory. *J. Geophys. Res.* 93(C5):8099-9110.
- Yu, L. & J. J. O'Brien, 1991. Variational estimation of the wind stress drag coefficient and the oceanic eddy viscosity profile. *J. Phys. Oceanogr.* 21:709-719.

Bohyun Bang

Born in Kwangju, Korea, 15 April 1955. Graduated from Kwangju Je-il High School in 1973. Received B. Sc., with a major in oceanography, from Seoul National University, Korea in 1978. Served as ROTC survey officer in the Korean army (1978~1980). Held a permanent position as a research scientist, developing remote-sensing softwares, in Korea Institute of Science and Technology, Seoul, Korea (1981~1985). Received M. Sc. from Seoul National University, Korea in 1985. Thesis topic: *A Reductionist Approach to Ecosystem Modelling in Kwangyang Bay, Korea*. Received the second M. Sc. (non-thesis research) from University of Washington, Seattle, Wa. in 1987. Research topic: *Estimation of apparent growth rate of phytoplankton from CZCS imagery off Washington Coast*. Entered doctoral program at the College of William and Mary, School of Marine Science in 1988.